Development of Dicyanomethylene-4*H*-pyran-Based Activatable Fluorescent Probes and Photosensitizers

by

Eda Kılıç

A Dissertation Submitted to the
Graduate School of Sciences and Engineering
in Partial Fulfillment of the Requirements for
the Degree of
Master of Science

in

Chemistry

March 17 , 2022

Development of Dicyanomethylene-4*H*-pyran-Based Activatable Fluorescent Probes and Photosensitizers

Koç University

Graduate School of Sciences and Engineering

This is to certify that I have examined this copy of a master's thesis by

Eda Kılıç

and have found that it is complete and satisfactory in all respects,

and that any and all revisions required by the final

examining committee have been made.

Committee Members:

_____

Asst. Prof. Dr. Safacan Kölemen (Advisor)

_____

Asst. Prof. Dr. Umut Aydemir (Co-Advisor)

_____

Assoc. Prof. Dr. Uğur Ünal

_____

Assoc. Prof. Dr. Salih Özçubukçu

_____

Asst. Prof. Dr. Sündüs Erbaş Çakmak

Date: 17.03.2022

Dedicated to my lovely family

ABSTRACT

Development of Dicyanomethylene-4*H*-pyran-Based Activatable Fluorescent Probes and Photosensitizers

Eda Kılıç

Master of Science in Chemistry

March 17, 2022

Cancer is used to express the abnormal growth of the cells and World Health Organization (WHO) reported that almost 16% of the worldwide deaths are caused by cancer. Chemotherapy and radiotherapy have surpassed surgery as the most effective cancer treatments. These treatments have proven effective in slowing tumour growth. Early detection of cancer is crucial in the development of new cancer treatments. Molecular biomarkers provide a molecular imaging pathway for early cancer detection. Several imaging agents are developed to image specific locations in living cells. In the first part of this thesis, a dicyanomethylene-4*H*-pyran (DCM) based fluorescent probe for the detection of Cu^{+} in cancer cell lines were developed.

Activity-based theranostic photosensitizers (aPSs) are highly attractive in the scope of photodynamic therapy as they offer enhanced therapeutic outcome on cancer cells with a live cell imaging opportunity at the same time. In the second part of this study, we modified the long known fluorescent DCM core with a heavy iodine atom to get a PS that can be further converted to aPS after simple modifications. DCM_O-I was tested in cell culture studies and proved to be a promising phototheranostic scaffold. Later, a cysteine (Cys) activatable PS based on the DCM core was developed, which exhibited remarkable $^1O_2$ generation capacity and a turn-on fluorescence response after reacting with Cys. In the third part, sulfur was introduced into the DCM scaffold and singlet oxygen generation capacities along with photophysical properties of sulfur-DCM analogues were investigated.

Keywords: DCM, Photodynamic Therapy, Fluorescent Sensors, Cysteine, Copper

ÖZETÇE

Disiyanometilen-4*H*-Piran Temelli Floresan Ajan ve Aktivite Bazlı Teranostik Işığa Duyarlılaştırıcıların Geliştirilmesi

Eda Kılıç

Kimya, Yüksek Lisans

March 17, 2022

Kanser, hücrelerin anormal büyümesini ifade etmek için kullanılır ve Dünya Sağlık Örgütü (WHO) dünya çapındaki ölümlerin yaklaşık %16'sının kanserden kaynaklandığını bildirmiştir. Kemoterapi ve radyoterapi, en etkili kanser tedavileri olarak cerrahiyi geride bırakmıştır ve bu tedavilerin tümör büyümesini yavaşlatmada etkili olduğu kanıtlanmıştır. Kanserin erken teşhisi, yeni kanser tedavilerinin geliştirilmesinde çok önemlidir. Moleküler biyosensörler, erken kanser tespiti için moleküler bir görüntüleme yolu sağlar ve canlı hücrelerde tümör bölgelerini görüntülemek için çeşitli görüntüleme ajanları geliştirilmiştir. Tez kapsamında, kanser hücre dizilerinde Cu^{+} analitinin tespiti için disiyanometilen-4-piran (DCM) tabanlı bir floresan probu geliştirilmiştir. Aktivite bazlı teranostik ışığa duyarlılaştırıcılar (PS), aynı zamanda canlı hücre görüntüleme fırsatı ile kanser hücreleri üzerinde gelişmiş terapötik sonuç sundukları için fotodinamik terapide oldukça çekicidir. Bu çalışmanın ikinci bölümünde, basit modifikasyonlarla aktivitesi arttırılması hedeflenen PS eldesi için DCM floresan boyasının çekirdeğini ağır iyot atomu ile modifiye edilmiştir. DCM_O-I adı verilen PS, HeLa kanser hücre hattında test edilmiş ve umut verici bir fototeranostik yapı iskelesi olduğu kanıtlanmıştı. Daha sonra, aktivite bazlı PS dönüşümü için Cys ile reaksiyona girdikten sonra verimli $^1O_2$ üretme kapasitesi ve floresan tepkisi sergileyen bir sistein (Cys) ile aktive edilebilir PS de geliştirilmiştir. Üçüncü bölümde, kükürt atomu ana DCM iskeletine eklenmiş ve kükürt-DCM türevlerinin singlet oksijen üretme kapasiteleri ile birlikte fotofiziksel özellikleri incelenmiştir.

Anahtar Kelimeler: DCM, Fotodinamik Terapi, Floresan Sensörler, Sistein, Bakır

ACKNOWLEDGEMENTS

I would like to express my deepest and sincerest thanks to my beloved supervisor, Dr. Safacan Kölemen. I would also like to extend my gratitude to him for giving me a chance to be a member of his research group; being his MSc student has been a tremendous privilege. I owe my most deep gratitude to him, not only for his guidance and never-ending moral support but also for his limitless motivation and enthusiasm, particularly in research and all aspects of life, which had motivated me even during difficult times. He is more than a mentor to me, like a family when needed. I have learned to perform independent research and publish results from him, and he has walked me through all of the above phases, never allowing me to struggle alone but stepping in when required.

I owe a special thank to Asst. Prof. Dr. Umut Aydemir for his support and guidance, and I would like to thank to KUBAM for financial support. I sincerely thank my thesis committee members, Assoc. Prof. Dr. Uğur Ünal, Assoc. Prof. Dr. Salih Özçubukçu and Asst. Prof. Dr. Sündüs Erbaş Çakmak for their valuable contributions and time.

I would like to express my sincere appreciation to Assoc. Prof. Görkem Günbas and his research group for their wonderful collaborations, particularly Dilay Kepil and Zübeyir Elmazoğlu for their invaluable contributions to the *in vitro* experiments.

Also special thanks to Antoine Marion and Thibaud Etienne for their invaluable contribution to computational study and helpful discussions on our collaborative study.

I am also very grateful to Dr. Hande Gündüz for her scientific advice, knowledge, and insightful discussions and suggestions. She has been my primary source to answer questions both in the lab and in personal life. I also want to thank her for her time and caring for witnessing my journey to become a chemist. I grew up with her assistance both as an undergraduate and graduate student. I feel so lucky to know such a brilliant colleague, and I will never forget her willingness to help, thank you so much.

I would like to extend my sincere thanks to Dr. Melek Sermin Özer for her scientific advice, knowledge, and insightful discussions. She has been a reason for me to smile uncontrollably whenever I see her, a great pleasure to have such her support in my life.

I want to express my deep blessing for my friends whom I consider as my family; Sultan, Çağrı, and Büşra. To the special ones, that make me believe in myself and love me for simply being me and having the friendship in a lifetime. My journey would have

never been the same without you guys; thank you for your unconditional support, reminding me to take breaks and have fun when I feel not quite myself.

Çağrı, you mean more than a best friend to me; I miss you and your joy around me. We all laughed at the lousy jokes that only one of us could understand; one eye contact is enough for me to break down in most serious situations. Thank you for making me laugh when I did not want to smile, constantly checking on me, and being there for me anyways. You are so important to me, my heart is full of so many ordinary moments, and you make all of extraordinary and incredible.

Sultan, the greatest of all time, thank you for always listening, supporting me, and encouraging me for my dreams. You are a true friend that I have wished for a long-time, and no better friend could I ask. I want you to know how much I love and appreciate you. I just cannot begin to thank you for all your advice and support and for always being on the other end of the phone, regardless of the time. You will always be my go to dance partner :)

Büşra, the best hood partner, our lives had drastically changed after you graduated. I could not go through so many things if not because of your help and tolerance. I can still remember the day we met; I saw the friendliest welcome in those green eyes. Now you have your own family, and it makes me so emotional through the tough times we fought against. I love you deeply, and thank you for making my life easier and funnier than it has ever been.

Also, I would like to express my thanks and best wishes to Eda Erbil, Zeynep Kılcan, Mehmet Akif Aktaş and Sarp Emre Turan for their help, joy and cherish they brought to my life. Thanks to Toghrul Almammadov for being kind and caring in personal life, although we had our conflicts while working together, and I had the great pleasure of working with other members of the Kolemen research group.

I started Koç University at the same time with Ahsen Sare Yalın and Aylin Kınık, who were my friends from the ITU, and we got closer during this journey. I consider them and their support as great treasures because we motivated each other for our dreams and made it through similar problems in our lives. I am hoping that I positively affected them as they affected me.

I would like to thank Assoc. Prof. Önder Metin in particular for his support and assistance. In addition, I would want to express my gratitude to all Metin Lab members for being wonderful and generous friends. Special thanks to Dr. Sibel Eken Korkut, Buse Sündü, Zafer Eroğlu, Temirlan Kubanaliyev that were extremely helpful in my reply.

It is an honor to thank my family for their love and endless support. I am so lucky to have such extraordinary parents, Serpil and Mahmut Kılıç, who are not questioning but doing everything they can in every way to make me follow my dreams. My brother, Sedat, has been my biggest hero all my life and has always had my back. Also, my dear uncle Eyüp, for the impact of the serenity he has given me. Their unconditional love, care, and support have made me the person I am today.

TABLE OF CONTENTS

LIST OF FIGURES

LIST OF TABLES

ABBREVIATIONS

PDT	Photodynamic Therapy
PS	Photosensitizer
aPS	Activatable Photosensitizer
ISC	Intersystem Crossing
PET	Photoinduced Electron Transfer
FRET	Förster-Type Resonance Energy Transfer
ROS	Reactive Oxygen Species
RNS	Reactive Nitrogen Species
NIR	Near Infrared
H_2O_2	Hydrogen Peroxide
D-π-A	Donor- π-Acceptor
DCM	Dicyanomethylene-4H-Chromene
BODIPY	4,4-difluoro-4-bora-3a,4a-diaza-s-indacene
GGT	γ-glutamyl transpeptidase
LAP	Leucine Aminopeptidase
ALP	Alkaline Phosphotase
GSH	Glutathione
TPA	Tri-(2-picolyl)amine
Cys	Cysteine
HCy	Homocysteine
NMR	Nuclear magnetic resonance
TMS	Tetramethylsilane
TLC	Thin Layer Chromatography
UV	Ultraviolet
LED	Light-Emitting Diode
RP-HPLC	Reverse Phase High Performance Liquid Chromatography
HPLC	High Performance Liquid Chromatography
DCM	Dichloromethane
MeOH	Methanol
ACN	Acetonitrile
EtOAc	Ethyl Acetate
DMSO	Dimethyl Sulfoxide
DPBF	1,3-Diphenylisobenzofuran
PBS	Phosphate-Buffered Saline
FBS	Fetal Bovine Serum
NAC	N-Acethyl Cysteine
MTT	3-(4,5-dimethylthiazol-2-yl)-2,5-diphenyl-2H-tetrazolium bromide
DCFH-DA	2',7'-Dichlorofluorescein Diacetate
AO	Acridine Orange
EtBr	Ethidium Bromide
MS	Mass Spectroscopy
PI	Propium Iodide

Chapter 1:
INTRODUCTION

Cancer is a comprehensive series of illness states that advance in a stepwise manner, beginning with molecular abnormalities and culminating in an uncontrolled growth region.[1] Cancerous cells proliferate uncontrollably because they are able to bypass natural cell death mechanisms due to mutations in nucleotide sequences and chromosomes, which eventually result in tumors or neoplasms. Chemotherapy, radiation therapy, and surgical excision of metastatic lesions are all ineffective in most cases since metastasis is generally numerous and drug resistant is common.[2]

There is an obvious need for a better knowledge of tumor microenvironment and metastasis in order to develop more effective cancer medicines, hence there is a lot of interest in cancer research. [3]In the treatment of malignant small tumors, photo-induced treatment, also known as photodynamic therapy (PDT), is a highly promising treatment modality thanks to its superior characteristics compared to state-of-the-art cancer therapy approaches .[4]

1.1 *Photodynamic Therapy*

Photodynamic therapy (PDT) is a new therapeutic approach that uses singlet oxygen as a primary cytotoxic agent to kill cancer cells. It has long been regarded as a promising alternative to traditional therapies as it offers minimally invasive procedures, multiple applications without side effects, and no drug resistance.[5] PDT also stimulates the immune system against cancer cells [6], and because singlet oxygen has a short lifespan (10-320 ns in aqueous medium) and a low diffusion length (10-55 nm), it is considered as a localized therapy. [7,8]

PDT actions requires some critical conditions (1) a photosensitizer (PS) with a cancer cell selectivity, (2) sufficient elapsed time after injection to achieve maximum accumulation of the photosensitizer in the tumor, and (3) irradiation of light with an appropriate wavelength presumably in the red/near-IR region. [5]

1.2 *Mechanism of Competitive Reactions in Photodynamic Therapy*

A photosensitizer (PS), light, and tissue oxygen ($^3O_2$) are the three main components of PDT activity. PS is initially exited to singlet excited states (S_1 or S_2) from its ground state (S_0) by light irradiation in a typical singlet oxygen production mechanism (*F*igure 1.1).[9–11] S2 decays non-radiatively (internal conversion) to S_1 in a short time, and then excited PS either relaxes back to ground state by producing light (fluorescence), or undergoes inter-system crossover (ISC) to generate a long-lived triplet excited state. As a result, fluorescence and ISC are two competing routes, and for effective singlet oxygen production, a suitable PS should have a high triplet quantum yield. Phosphorescence or intermolecular energy transfer to dissolved triplet oxygen (ground state oxygen) in cancer tissues can release triplet excited state energy, resulting in extremely lethal singlet oxygen ($^1O_2$).

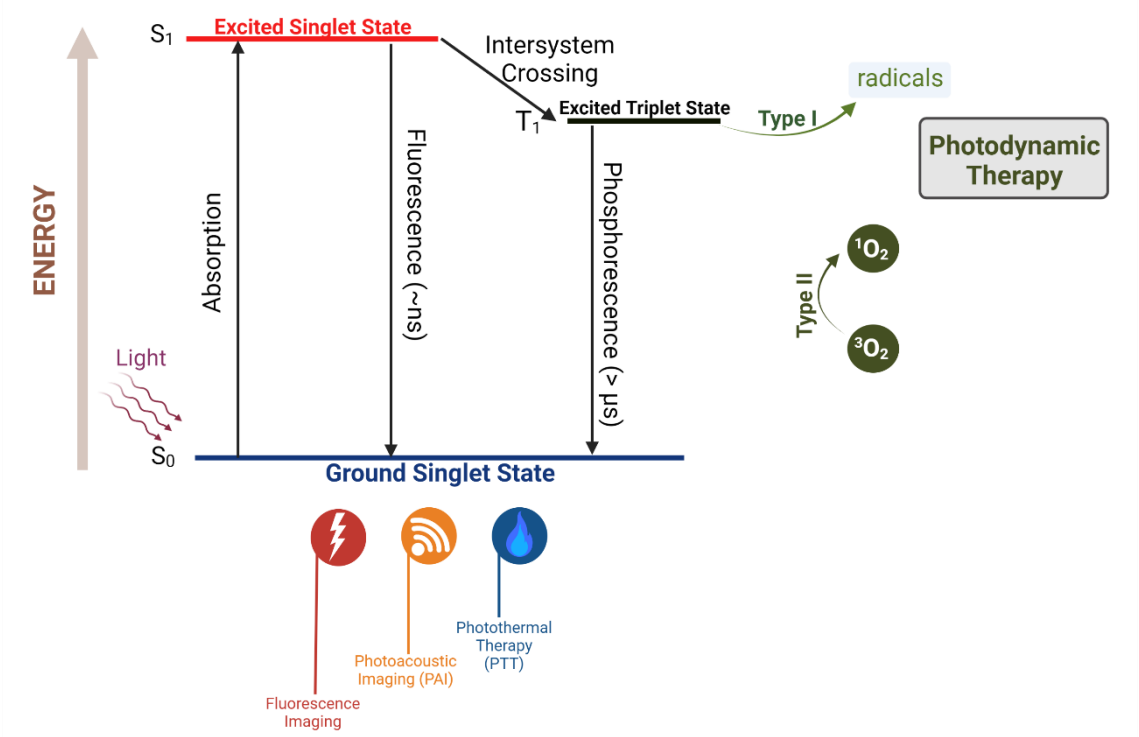

Figure 1.1 Simplified Jablonski energy level diagram.

The transfer of an electron or proton to oxygen and surrounding molecules to produce anionic or cationic radicals is a type I reaction. These radicals have the ability to combine with oxygen molecules to produce reactive oxygen species (ROS). The transfer of one electron to an oxygen molecule in reaction type I frequently results in the creation of superoxide ions.[12] These ions are not active in biological systems, but they can create

hydrogen peroxide (H_2O_2), which is easily absorbed via cell membranes. In high quantities, H_2O_2 may react with super oxide molecules, resulting in the formation of hydroxyl as an active radical capable of ionizing any molecule with a low activation energy.[13] In reaction type II, the photosensitizer molecule transforms to excited singlet oxygen by transitioning from the triplet state to the ground state and transferring energy to the oxygen molecule.[14] As a charge-less molecule, singlet oxygen may spread to the cytoplasm and biological membranes.

1.3 *Activatable Photosensitizers*

To increase the selectivity of photosensitizers, additional control mechanisms on PDT activity are appreciated. Active targeting, in which PSs are selectively linked to endogenous surface receptors that are overexpressed in cancer cells is one prominent strategy in this regard. Designing activatable or activity-based photosensitizers is another interesting option (aPS). Even when exposed to light, these photosensitizers stay in a passive "off" state (no cytotoxicity) in healthy cells, and are specifically triggered by tumour-associated stimuli at the region where treatment is required.[15] The selectivity is primarily satisfied because malignant and normal cells have distinct metabolic activities, which changes the dynamics of the cellular microenvironment.

The photosensitizer core is masked with a protecting group in a typical aPS design, which inhibits $^1O_2$ production and fluorescence, even under light stimulation.[16] Several photophysical properties of the aPSs change when the masking unit is removed in the presence of tumour-associated inputs such as an acidic microenvironment of cancer cells, elevated levels of biothiols and reactive oxygen species, as well as overexpressed enzymes. As a result, both $^1O_2$-induced photocytotoxicity and emission signal are recovered. Modulation of PS's excited states can be accomplished through appropriate molecular engineering techniques such as photoinduced electron transfer (**PeT**), intramolecular charge transfer (**ICT**), and förster-type resonance energy transfer, among others (**FRET**).

PeT is a well-known phenomenon that is often utilized in the development of molecular fluorescent probes.[17–19] It is also capable of modulating the ISC process in aPSs. A spacer connects an electron donating group to a PS core in the construction of PeT-based aPSs. When the PS is stimulated, an electron transfer occurs from the donor unit to the core, and the excited electron relaxes back to ground state following non-

radiative paths rather than the ISC channel.[19] Also it effectively disables ISC since these two routes compete and the PeT process occurs extremely quickly. When PeT is blocked after an electron donating unit is involved in a binding interaction with an analyte of interest, the ISC channel can be reopened for an excited electron.

The FRET mechanism is fascinating since it allows for the generation of extremely potent and selective aPSs. In this pattern, PS core serves as a donor and is linked to an acceptor/quencher fluorophore through a cleavable linker. When the PS is excited, energy is transferred from the PS to the acceptor unit, and the ISC route is deactivated. FRET is disrupted after breakage of the linker that joins PS and the acceptor molecule in tumor cells, and excitation of the PS results in effective ISC and subsequent $^1O_2$ production.[20,21]

Another well-established mechanism in the designing of aPSs is intramolecular charge transfer (ICT). A donor-acceptor (D-π-A) structure is used in an ICT-based aPS.[22] Charge transfer happens during excitation from the donor unit, which is usually phenolic or amine groups, to the acceptor side, causing charge redistribution throughout the molecule. Because of blocked ICT and charge delocalization, a strong blue shift in the absorption signal of PS is noticed when the electron donating unit is blocked with a cleavable cage unit.[23–26] When the cage group is selectively eliminated by a corresponding analyte, ICT activates and the red-shifted absorption peak is restored. When the PS is excited by a freshly arrived red-shifted absorption signal, $^1O_2$ creation begins.[27] On the other hand, no evidence of $^1O_2$ generation can be detected in the caged form since the external light irradiation, which is regulated according to the red-shifted signal, is unable to activate the PS.

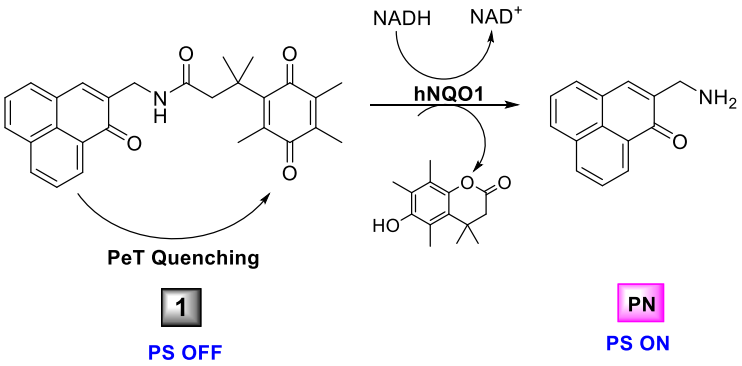

Figure 1.2 In presence of NQO1, reduction of the quinone to quinol results in releasing dihydroxylcoumarin and PS on active product.

Beharry group has revealed a PeT-mediated NQO1-responsive activatable PS.[28] As a theranostic scaffold, they used a highly effective phenalenone (PN) core (Figure 1.2). Because of active PeT from the PS core to the quinone cage, PN's cytotoxicity and fluorescence are muted by a quinone derivative. The $^1O_2$ and fluorescence quantum yields of the PS in caged form are determined to be 0.28 and 0.0036, respectively. When the PS is treated with HQO1 enzyme, the quinone group is reduced and followed by intramolecular cyclization, releasing the cage and restoring the PN core's fluorescence and $^1O_2$ capacity.

Hua and colleagues recently presented a diketopyrrolopyrrole (DPP)-based PS (DPP-GGT) with a 4-bromomethylphenyl glutamic acid as a GGT responsive cage unit.[29] DPP-GGT displays a blue shift from 532 nm to 490 nm as a result of GGT-induced cage breakage through the ICT mechanism. After GGT activation, the emission signal shifts to lower wavelengths, and active PS emits at 548 nm (Figure 1.3). DPP-GGT has a strong ratiometric response in fluorescence and substantial photocytotoxicity in HepG2 cells, where GGT is known to be overexpressed. In low GGT expressing MCF-7 (breast cancer) and normal LO2 cells, however, only red shifted emission signals are seen, with no apparent cell death.

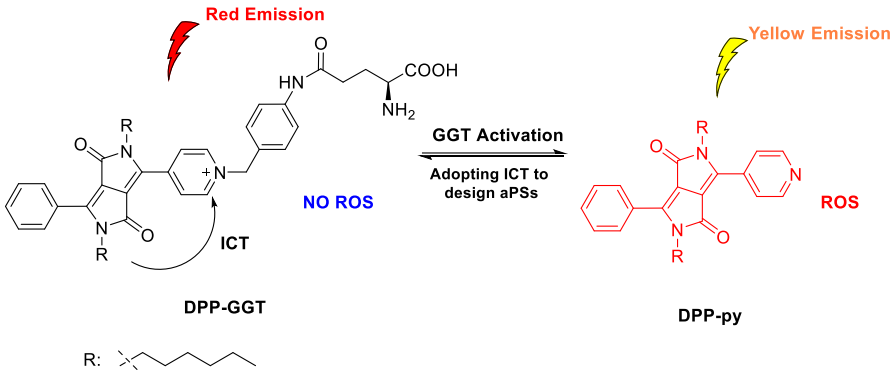

Figure 1.3 Activation mechanism of γ–GT activatable DPP-GGT photosensitizer.

Activatable photosensitizers that are responding to more than one analyte have received a lot of interest in the recent decade since they can enhance PS selectivity over single input activatable PDT drugs.[30–32] In the construction of such aPSs, two biological activators (enzymes, pH, thiols, and ROS) are coupled, and extra selectivity is achieved by the PS turning on its photocytotoxicity only when two inputs are present, simulating the AND logic gate action.

As a highly selective PDT agent, Wang and colleagues developed a GSH and H_2O_2 dual activatable benzothiadiazole derivative (HO-NB-Bpin).[33] A H_2O_2-responsive boronate ester cage unit protects the thiol group on the PS (Figure 1.4). This change not only adds an activation side, but it also prevents the interaction of O-NB-Bpin with GSH. As the cage group is removed after the addition of H_2O_2 and 1,6-elimination, HO-NB-SH is generated, which is subsequently transformed to the cytotoxic and emissive HO-NH_2ArSO_3H through H_2O_2 and GSH. Chemical trap tests have shown that HO-NH_2ArSO_3H can cause both Type I and II PDT action. In the same work, mito aPS, a mitochondria-targeted analogue of HO-NB-Bpin, is produced and tested in HeLa cells. Light irradiation causes dose-dependent cell death in hypoxic situations. The effectiveness of the PS in hypoxia is mostly due to its ability to initiate oxygen independent Type 1 PDT activity. MitoaPS may also be employed in the context of two-photon PDT, which is extremely useful for future biological research.

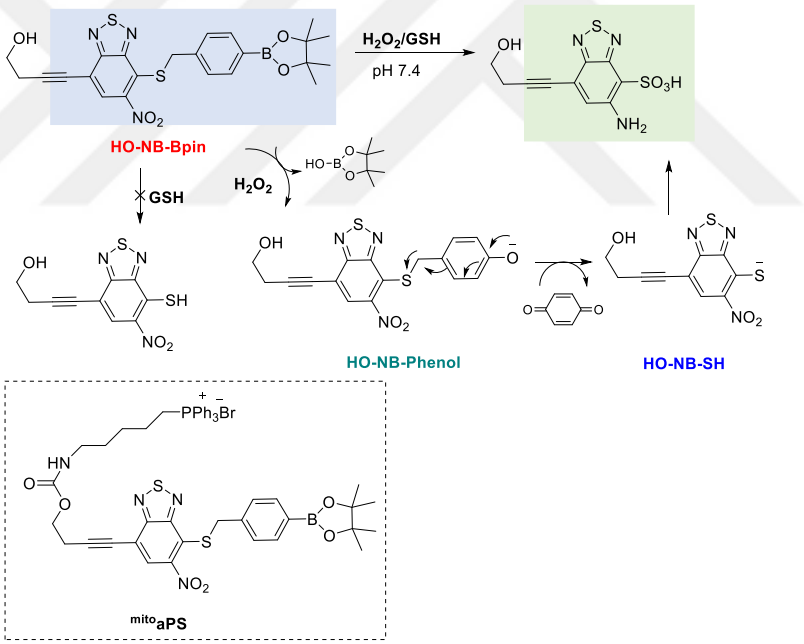

Figure 1.4 Schematic illustration of H_2O_2/GSH activatable HO-NB-Bpin targeting both hydrogen peroxide and GSH.

1.4 *Fluorescence Imaging*

Fluorescence can be simply described as a molecule's capacity to emit light that is absorbed at a specific wavelength. First, the molecule is excited with light of a certain wavelength, which causes it to enter the singlet excited state. At that point, alternative relaxation mechanisms exist including light emission, inter-system crossover (ISC), and

nonradiative relaxations.[34] ISC and fluorescence are competing routes as previously mentioned; a molecule with a high triplet quantum yield will lose its fluorescence. Fluorescence is the relaxation to the ground state caused by the release of luminescence. Because of its outstanding features, fluorescence is widely considered as the best signaling method for optical molecular sensors. The most essential property of fluorescent probes (fluorophores) is their great sensitivity, which is attributable to Stokes' shift, which gives distinct wavelengths for excitation and emission.[35] Fluorescence imaging has been intended to help with early cancer diagnosis and also accurate real-time tumor localization during surgery.[36] It is sensitive, safe, and simple to use; it also enables for quantitative information on an enzyme to be retrieved through real-time imaging. Among prospective optical imaging technologies, near-infrared fluorescence imaging, with its high sensitivity and multi-detection capabilities, is an appealing modality for early cancer diagnosis.[37] This method is based on a fluorescence probe that emits in the near-infrared range (650-900 nm).[38]

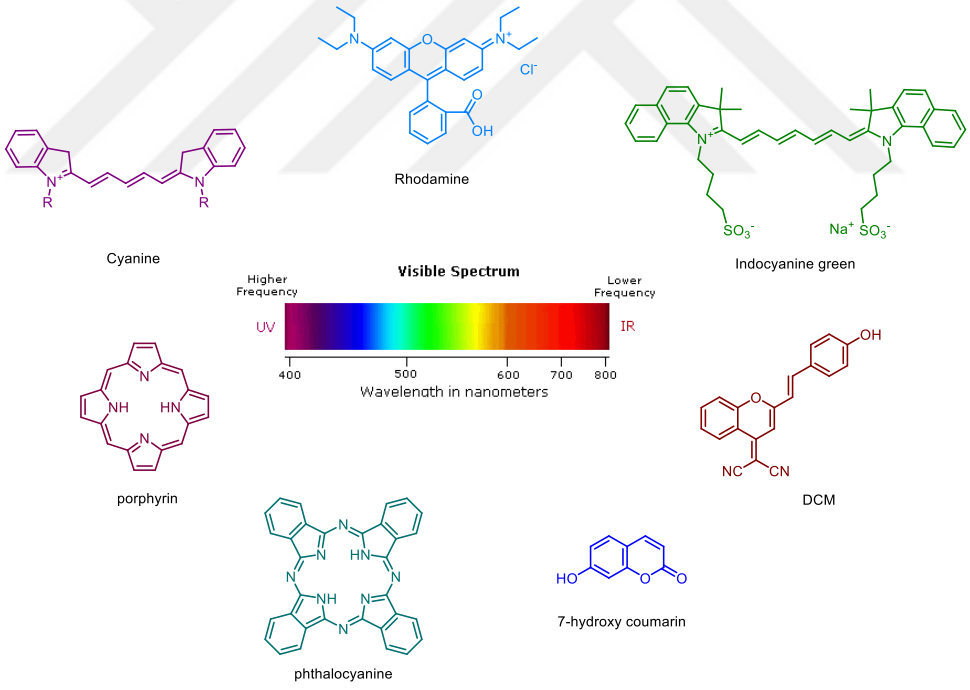

Figure 1.5 Molecular structures of several NIR fluorescent probes.

In the last two decades, several NIR fluorescent probes have generated a lot of interest in bioimaging and therapies. There have been several NIR fluorescent probes created with excellent photophysical characteristics and these dyes can be categorized into many groups, including cyanines, rhodamine analogs, 4,4-difluoro-4-bora-3a,4a-diaza-s-indacene (BODIPYs), DCM (dicyanomethylene-4*H*-pyran), squaraines,

phthalocyanines, and porphyrin derivatives, as well as other related dyes. Figure 1.5 shows the fundamental chemical structures of these dyes.[39]

1.5 *Theranostics: Combination of Diagnosis and Therapy*

Combining therapeutic activity and fluorescence imaging is another attractive approach in the development of new generation PDT drugs. The theranostic agents have sparked a lot of attention in recent years since they can track the location of tumors and medications in addition to treatment opportunities.

In 2021, our group had reported the first resorufin-based photosensitizer (RR-1) that can be selectively triggered in cancer cells by hydrogen peroxide (H_2O_2) as well as the first resorufin-based phototheranostic agent.[40] RR-1 is composed mainly of an iodinated resorufin core and a phenylboronic acid pinacol ester cage group that can be cleaved by H_2O_2 (Figure 1.6). Prior to H_2O_2 treatment, RR-1 shows a maximal absorption at 488 nm due to a suppressed ICT process. With the addition of H_2O_2, the ICT mechanism was engaged, resulting in a significant red shift in the absorption signal, as well as a turn-on response in the fluorescence peak at 597 nm. The parent iodo-resorufin (Res-I) is released by H_2O_2-induced oxidative boronate cleavage in cancer cells, which restores both PDT activity and fluorescence at the same time, yielding a theranostic agent.

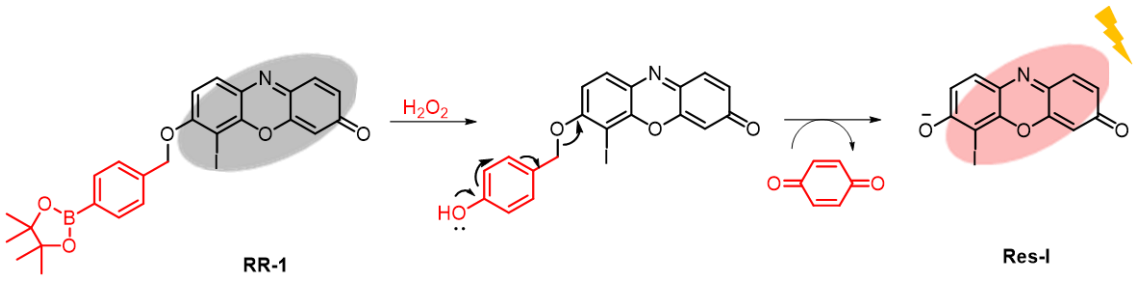

Figure 1.6 Activation mechanism of RR1 with H_2O_2.

In addition to RR-1; our group developed leucine aminopeptidase (LAP) activatable PDT agent (HCL), which is based on a red-shifted, water soluble, and photostable brominated hemicyanine derivative.[41] HCL is made up of a leucyl cage unit, a self-immolative linker, and a PS core based on brominated hemicyanine (Figure 1.7). Endogenous LAP enzyme preferentially activated HCL in A549 (lung) and HCT116 (colon) cancer cells with high LAP levels, resulting in efficient photocytotoxicity and low dark toxicity. In addition, when the PS was activated with LAP, the fluorescence of the

parent bromo-hemicyanine core was restored. Healthy L929 cells, on the other hand, showed no signs of phototoxicity or fluorescence turn-on. As a result, HCL is a useful and LAP-sensitive phototheranostic agent. Different cancer-associated analytes, in conjunction with near-IR absorption scaffolds, might be used in the context of activatable PDT designs to enrich the tumour-selective PS arsenal, according to our findings.

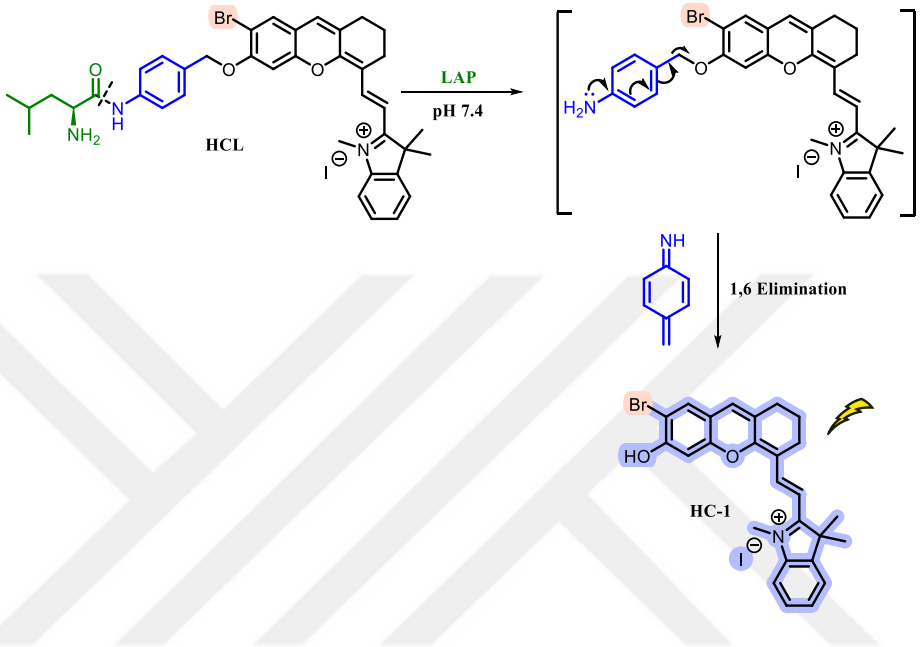

Figure 1.7 The cleavage mechanism of HCL in the presence of LAP.

Also, another novel theranostic core by our group was introduced as an iodinated silicon-fluorescein (SF-I), an effective red-shifted theranostic agent at physiological conditions.[42] Under both 595 and 630 nm irradiations, SF-I showed high $^1O_2$ quantum yields, and its cytotoxicity was tested in negative breast (MDA MB-231) and colon (HCT-116) cancer cell lines. *In vitro* cell culture studies clearly revealed that SF-I may trigger cell death as a result of effective PDT action and at the same time can still operate as a fluorophore. SF-I presents a new family of readily available photosensitizers that have the potential to enable image-guided PDT applications. Furthermore, the SF-I core can be customized with different cage groups, targeting moieties, and organelle directing units to create highly effective cancer cell selective agents.

1.6 *DCM (Dicyanomethylene-4H-pyran) Chromophores*

Dicyanomethylene-4*H*-pyran (DCM) chromophores are traditional donor-π-acceptor (D-π-A) chromophores with a wide absorption band due to an ultra-fast internal charge–

transfer (ICT) mechanism (Figure 1.8).[43] Tang et al. presented a DCM derivative as a highly luminous dopant in organic electroluminescent diodes for the first time in 1989.[44] Due to their superior optical-electronic characteristics and extensive structural modification, several DCM-type derivatives have been investigated in recent years. The structural alteration of DCM chromophores can be used for OLED emitters, logic gates, and optical chemosensors.[43]

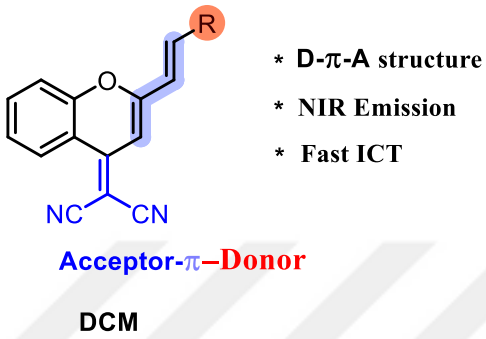

Figure 1.8 Schematic diagram of D-π-A structure in DCM chromophore.

D-π-A structures are mainly composed of three parts: an electron-donor group (D), a π-conjugated linker and an electron-acceptor group (A). The donor group can significantly affect fluorescence spectra while also acting as a reactive site for analytes. They possess excellent optical properties such as a long emission wavelength, a large Stokes shift, and excellent photostability.[26] Significantly, DCM derivatives can be utilized as an activity-based molecular sensor. To this end, DCM core has previously been employed for the detection of a wide range of analytes, including various anions, biothiols, ROS, RNS and enzymes.[45–51]

Using DCM as the fluorophore and 2,4-dinitrobenzensulfonyl group as the fluorescence quencher and recognition moiety, James *et al*. created a colorimetric and NIR fluorescence turn-on thiol-responsive probe.[52] Also following these promising findings, additional DCM derivatives (X-DPCO) were created by inserting an electron-withdrawing group (F or Cl) into the phenol ring, lowering the phenolic hydroxyl group's pKa. The F and Cl derivatives, without a doubt, function better in weakly acidic circumstances and can be used in *in vivo* applications.[53] (Figure 1.9)

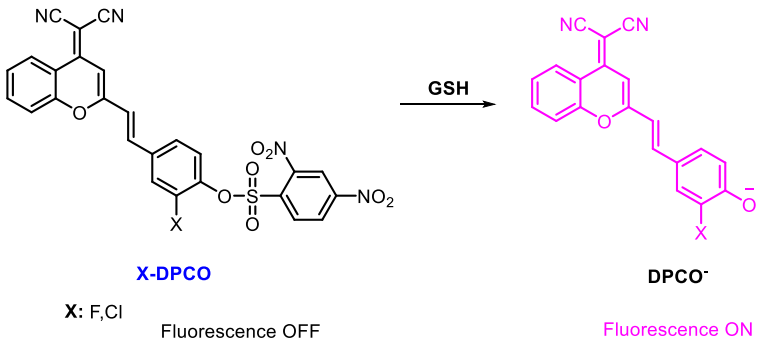

Figure 1.9 GSH promoted release of $DCPO^-$.

β-galactosidase (β -gal) has been shown to be a significant biomarker for primary ovarian malignancies as a typical enzyme. Zhu and colleagues described an enzyme-activatable ratiometric near-infrared (NIR) probe (DCM-βgal) for *in vivo* and *in situ* real-time measurement and trapping of β-gal activity.[26] For the first time, this system used the lacZ gene transfection method to track endogenously overexpressed β-gal distribution in living HEK293T cells and OVCAR-3 cells, as well as real-time *in vivo* bioimaging of β-gal activity in colorectal tumor-bearing nude mice, providing an accessible tool for the unprecedented quantification and trapping of β-gal activity for *in vivo* human colorectal cancer diagnosis. (Figure 1.10)

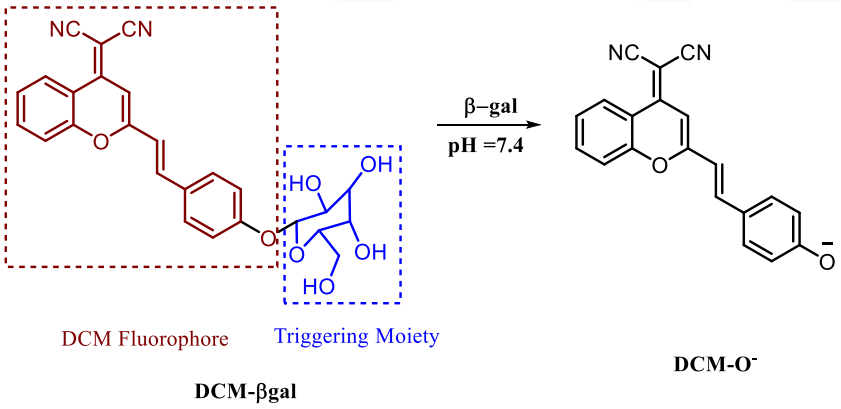

Figure 1.10 Sensing mechanism for β-Gal enzymatic reaction of DCM- βGal.

Tracking the overexpression of the specific enzymes in the tumor area makes diagnostic and therapy more convenient. Figure 1.11 summarizes key examples of the current enzyme[54–56], ROS[55–59] and RNS[60,61] activated DCM derivatives. Wei and colleagues used a new NIR fluorescent probe, Cl_2 -BDCM-ALP, to build a smart nanocontainer to address the time-resolved monitoring of alkaline phosphatase (ALP) activity *in vivo*.[62] The phenolic hydroxyl of chlorine-substituted BDCM had its pKa value decreased to 6.97, indicating that it may be used in a variety of pH environments. Long-term time-resolved

monitoring of endogenous ALP activity *in vitro* and *in vivo* has been accomplished using the photoresponsive nanocontainer. Guo et al. recently described DCM-TYR, an activatable NIR ratiometric fluorescent probe for detecting tyrosinase activity.[63]

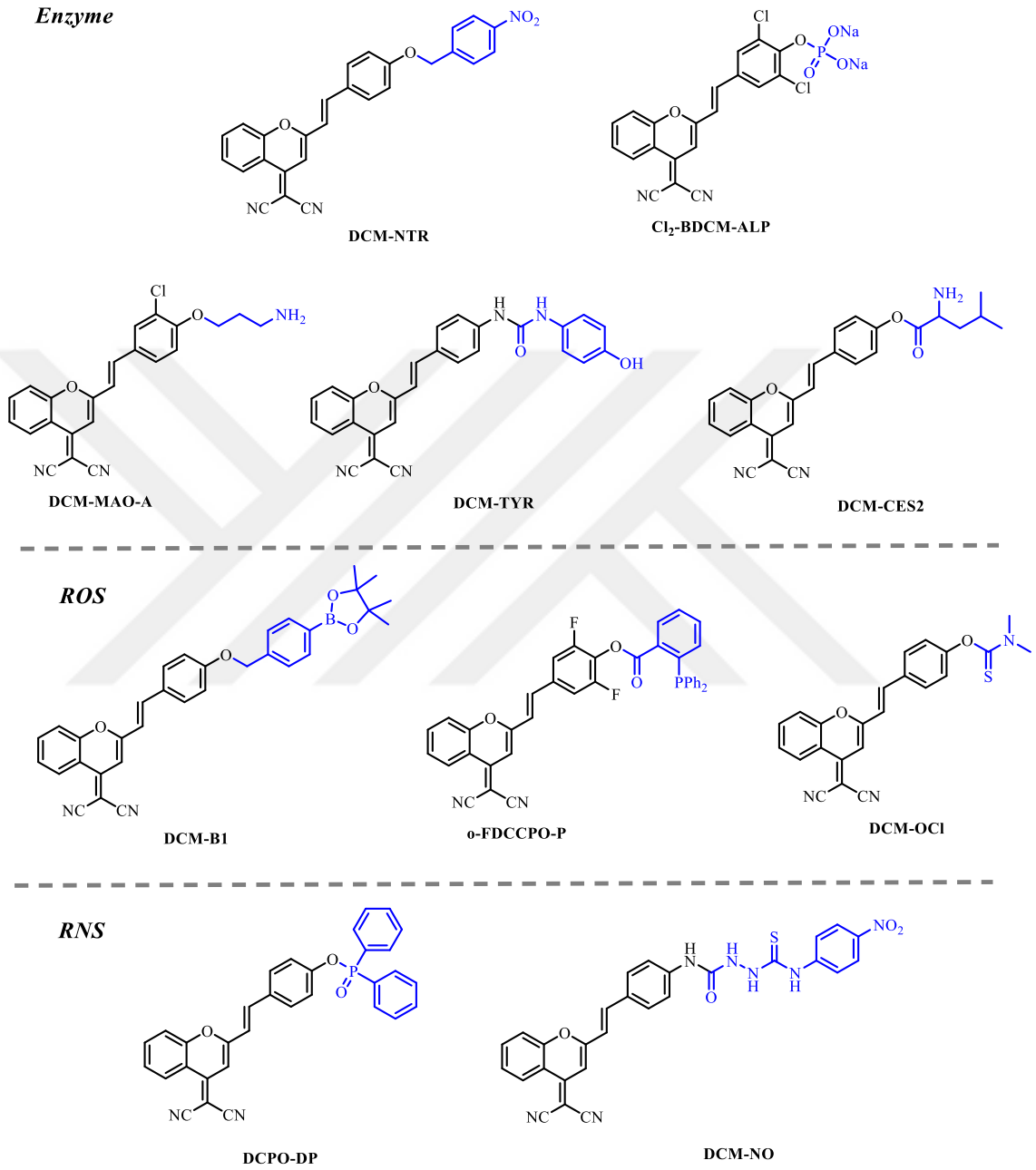

Figure 1.11 Structure of DCM fluorescent probes for sensing various analytes.

Among all the examples given before, Li et al. recently presented a series of modified DCM derivatives by substituting ordinary oxygen with selenium, which are further modified with either two iodine or bromine at the *ortho* position of the phenolate unit as activatable PSs.[25] It was demonstrated that the presence of heavy atom, selenium, in combination with iodine/bromine atoms significantly boosted the $^1O_2$ quantum yield owing to enhanced spin-orbit coupling via ISC (Figure 1.12).

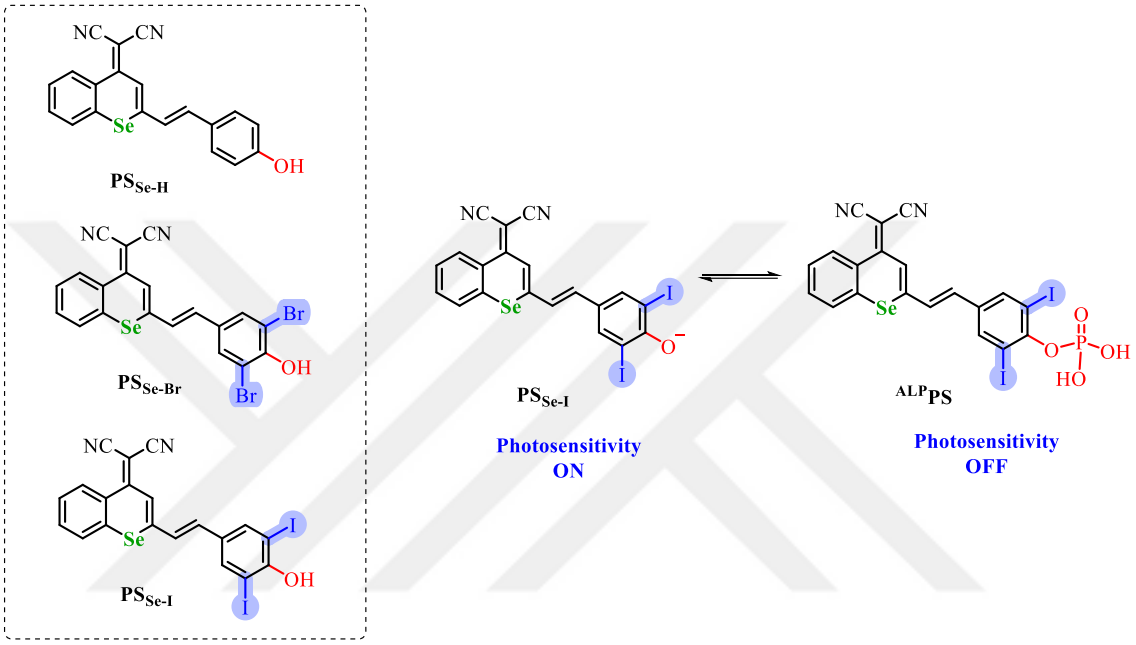

Figure 1.12 Different types of D-π-A photosensitizer including various electron withdrawing groups that decreases pKa value of the phenolic group and activation strategy of PS_{Se-I} with alkaline phosphotase enzyme.

They also created alkaline phosphatase (ALP) and peroxynitrite ($^-$ONOO) sensitive PSs from their most promising di-iodinated Se-substituted DCM core and successfully assessed their photocytotoxicity in malignant cell types. A cationic triphenylphosphinium unit is also added to the core structure to target mitochondria. As with their ALP responsive agent, removing the cage unit restores ICT and triggers photocytotoxicity, as indicated by a loss in cell viability in activated RAW 264.7 cells (Figure 1.12).

1.7 *Copper(I) Responsive Fluorescent Probes*

Copper is a crucial cofactor in the mitochondrial matrix of the enzymes cytochrome c oxidase (CcO) and superoxide dismutase (SOD1), both of which are involved in the creation of cellular energy and the execution of apoptotic processes.[64]

Cu^{2+} and Cu^{+}, the two physiologically relevant oxidation states of copper, are thought to be the most prevalent in the reducing environment of the cell cytoplasm.[65,66] In a cytosolic reducing environment, the soft transition metal copper prefers to be in the Cu^{+} oxidation state rather than Cu^{2+}. Copper has a high chemical redox potential and the capacity to form hydroxyl radicals via the Fenton reaction, making it potentially hazardous.[67] When *in vivo* copper concentrations surpass the usual range, the redox active metal creates a health danger by producing reactive oxygen species (ROS) that can trigger cellular metabolic disturbances.[68]

Fluorescent probes that can visualize copper distribution inside distinct subcellular organelles are useful tools for studying copper homeostasis at the cellular level.[64,69,70] Despite the increasing popularity in the production of specialized fluorescent probes for other cations, copper-selective probes are relatively rare, and research into copper-selective probes is particularly difficult for the biological system dominating oxidation state (1+).[66] Cu^{+} is a powerful free radical quencher in all coordination settings due to its paramagnetic nature. Glutathione (GSH,γ-glutamine-cystein-glycine) is a tripeptide that converts Cu(II) to Cu(I) and binds strongly to soft metals like copper(I), producing extremely stable complexes even when oxygen is present. Glutathione is the most prevalent intracellular nonprotein thiol, with concentrations ranging from 1 to 6 mM in all live cells.

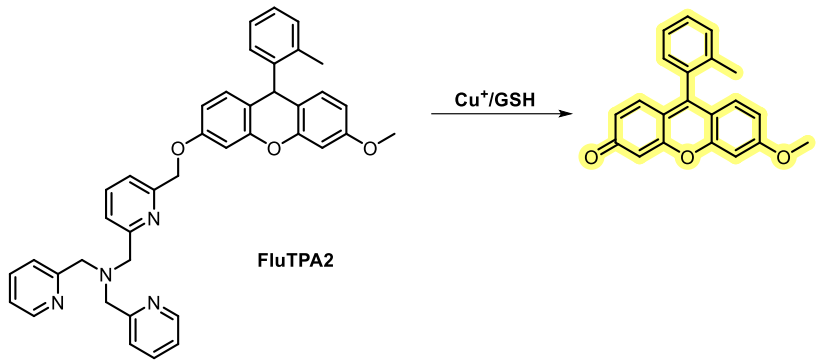

Figure 1.13 Proposed reaction of TPA unit cleavage in the presence of Cu+/GSH.

Taki and colleagues reported the first reaction-based Cu-responsive probe. They used tripicolylamine (TPA unit) as a selective copper receptor. Cu^{+} assisted removal of the cage group from the chromophore's backbone phenolic moiety functions as an off–on switch for signaling Cu^{+} NIR fluorescence.[71] (Figure 1.13)

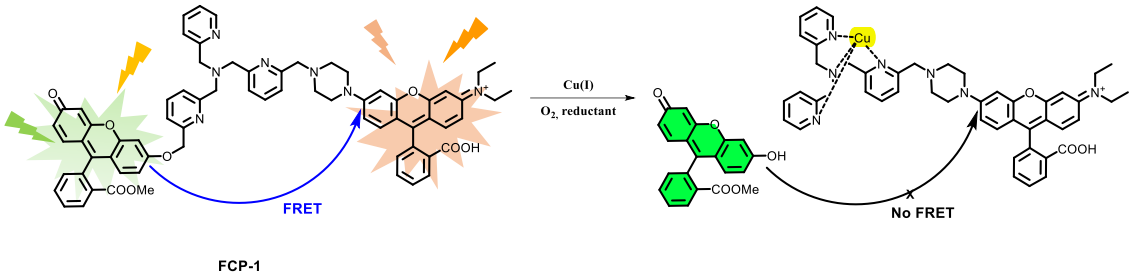

Figure 1.14 Cleavage of Fluorescein and Rhodamine Dyes with Cu+ analyte.

Chang and coworkers proposed a probe, FCP-1, a ratiometric fluorescence resonance energy transfer (FRET) copper probe for activity-based detection of labile Cu(I) pools in living cells. The TPA bridge connects fluorescein and rhodamine dyes in FCP-1(Figure 1.14). FRET between fluorescein donor and rhodamine acceptor is reduced by bioinspired Cu(I)-induced oxidative cleavage. FCP-1 can be used to monitor dynamic changes in labile Cu(I) pools in living cells because of its strong metal and oxidation state specificity, as well as its 2-color ratiometric FRET response. FCP-1 was able to accurately detect declines in endogenous levels of labile Cu(I) in mouse embryonic fibroblasts due to the self-calibration provided by its ratiometric response (MEFs).[72]

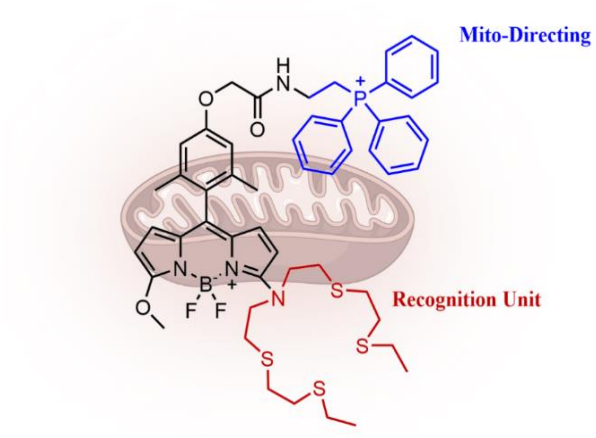

Mito-CS1

Figure 1.15 BODIPY based mitochondria targeted and, a thioether-rich receptor for selective recognition and binding of Cu^{+} fluorophore Mito-CS1.

Chang et al. also reported a photo-induced electron transfer mechanism-based mitochondria-targeted fluorescent probe, Mito-CS1, for Cu^{+} detection.[73] This probe had a cationic triphenylphosphonium group that accumulated exclusively in mitochondria, allowing for the monitoring of changes in mitochondrial Cu^{+} contents in live samples (Figure 1.15). The use of this probe was restricted, however, due to the small fluorescence

on/off ratio (ca. 10-fold) that originated in significant background fluorescence of the metal-unbound form, which can frequently conceal the detection of the required signals. Mito-CS1 was found in the mitochondria of live HEK293T cells and fibroblasts, and it was sensitive to copper supplementation and chelation.[73]

Herein, in the first part of the thesis, we offer a reaction-based ratiometric **DCM-Cu** for Cu^{+} in a physiological reducing environment (Figure 1.16). First, DCM_O was synthesized through given synthesis route in Figure 3.1. To specifically target the +1 oxidation state of Cu, we installed a Cu^{+} responsive tris[(2-pyridyl)methyl] amine (TPA) unit to DCM fluorophore to generate DCM-Cu. Results indicated that the reaction of Cu^{+} and DCM-Cu uncaged the probe resulted in a red shifted absorption signal along with a turn-on response in NIR fluorescence. The probe was tested in a HeLa cell line and successfully monitored changing copper concentrations.

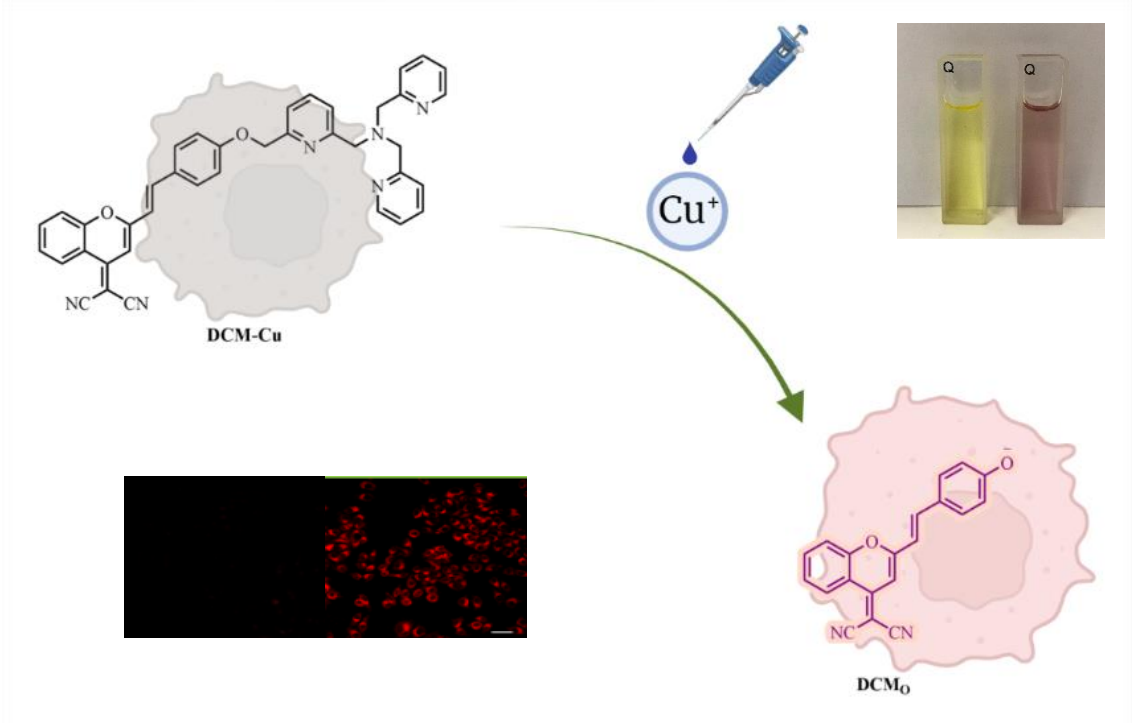

Figure 1.16 The schematic representation of the activation process of **DCM-Cu.**

1.8 *Cysteine (Cys) Sensing and Signaling*

Cys is an essential thiol-containing amino acid that involves in many physiological processes including protein synthesis, detoxification, metabolism and post-translational modification.[74] Abnormal levels, on the other hand, are strongly linked to a variety of illnesses. The concentration of intracellular Cys is changed between 30 and 200 μM.[75] Cys-specific molecular probes may be constructed based on two distinct features of Cys that distinguish it from Hcy and GSH. The first is that Cys has a lower pKa (8.53) than GSH (9.20) and Hcy (10.86), making it more nucleophilic than other biothiols under physiological conditions.[76] Also, Cys has a smaller size compared to Hcy and GSH, resulting in a less steric shielding effect than other biothiols. Cys-responsive molecular probes have been created by combining fluorescein, naphthalimide, coumarin, boron dipyrromethene (BODIPY), and cyanine derivatives along with different luminophores (Table 1).[77–85] Practically all optical sensors for biothiol detection use a chemodosimeter technique, which is based on molecular sensors reacting with thiols. Michael addition, cyclization with aldehydes, cleavage of sulfonamide/sulfonate esters, thiol-halogen substitution, and metal complex coordination are the mechanisms for these particular reactions.

Cys-triggered addition-cyclization-cleavage reaction with acrylate moiety is the most widely used mechanism for developing Cys-responsive probes among numerous response mechanisms. The addition reaction of Cys with the C=C bond of the acrylate can be achieved by shielding the hydroxyl groups of fluorophores with acrylates. The cyclization-cleavage processes that follow this addition reaction lead to the deprotection of the fluorophore's hydroxyl and the generation of 7-membered ring compound. In contrast, while the nucleophilic addition reaction of Hcy or GSH with acrylate can occur, the cleavage reaction is exceedingly slow or impossible due to the formation of high membered rings. As a result, the most successful strategy for constructing Cys-responsive probes is to use Cys-triggered addition-cyclization-cleavage reactions with an acrylate unit.[76]

Table 1 Overview of Cys targeting fluorescent probes and their photophysical properties.

Cys Targeting Probe	λ_{ex} / λ_{em}	Stokes Shift	Linear Dynamic Range	LOD	Ref
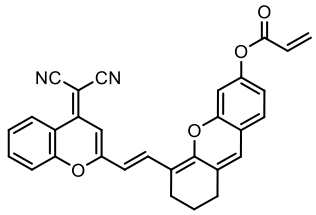	600/760	160	0-10 μM	48	[86]
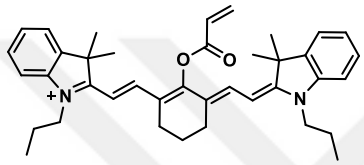	520/560 720/780	-	0－25 μM	-	[87]
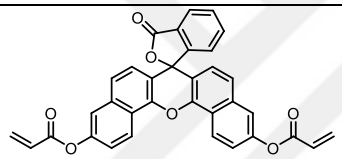	620/690	70	0－25 μM	180 nM	[88]
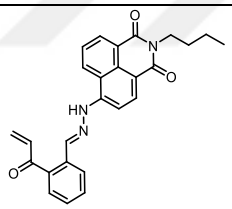	456/536	80	0-80 nM	25 nM	[89]
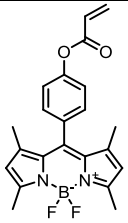	480 /517	37	0.2- 30 mM	50 nM	[90]
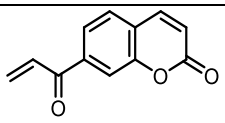	332/455	123	0–16 μM	65 nM	[91]

In this thesis, we introduced a cysteine selective iodinated DCM as a cysteine (Cys) activatable PS (DCM_O-I-Cys) to get a cancer cell selective theranostic PS. The activity of DCM_O-I-Cys was tested in human cervical cancer cells (HeLa) and mouse fibroblast cell (L929) lines.

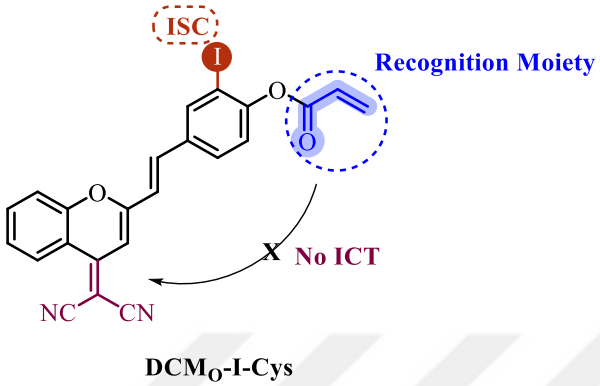

Figure 1.17 Design Principle of DCM_O-I-Cys

DCM_O-I-Cys has an acrylate unit, a well-known Cys cleavable masking group, as recognition moiety that blocks the parent DCM_O core's photosensitivity and fluorescence effect (Figure 1.17). Iodine was added to the core structure to lower the phenol's pKa and raise the phenolate concentration at pH 7.4, which is necessary for obtaining a red-shifted absorption signal and a strong fluorescence signal after activation. Additionally, adding a heavy element (iodine) to the structure results in a high triplet quantum yield as well as the capacity to make singlet oxygen via photodynamic action. The cage unit is selectively cleaved by Michael addition of Cys to the acrylate group, followed by intramolecular cyclization, restoring PDT activities and the DCM_O core's distinctive high emission signal (Figure 1.18). As a result, even if healthy cell lines take up the PS, it will be inert and so non-toxic.

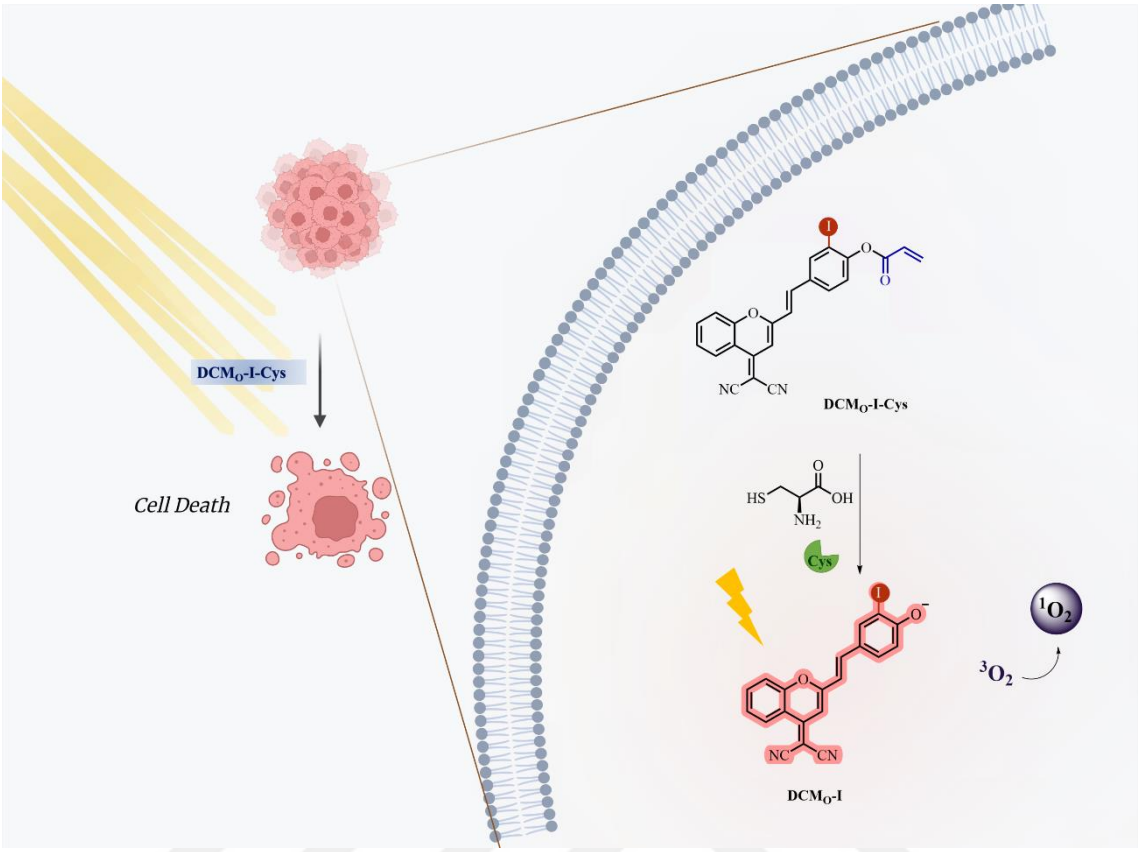

Figure 1.18 The schematic representation of the PDT effect of DCM$_O$-I-Cys.

Chapter 2:
Materials and Methods

2.1 *Chemicals and Instruments*

All reagents were commercially available and used without further purification unless otherwise noted. All dry solvents used in reactions were dried over 4A˚ sieve and, dry THF was directly obtained from the Mbraun MBSPS5 solvent drying system. The inert atmosphere was obtained by Argon. The ^{1}H and ^{13}C-NMR spectra were recorded on a Bruker (500 MHz) spectrometer using $CDCl_3$ or d_6-DMSO as the solvents. The chemical shifts are reported in parts per million (ppm) downfield from an internal TMS (trimethylsilane) reference. Coupling constants (J) are reported in hertz (Hz), and the spin multiplicities were specified by the following symbols: s (singlet), d (doublet), t (triplet), and m (multiplet). NMR spectra were processed with MestReNova program. Column chromatography was performed by using thick walled glass columns and silica Gel 60 (Merck 230-400 mesh). Thin layer chromatography (TLC Merck Silica Gel 60 F254) was performed by using commercially prepared 0.25 mm silica gel plates and visualization was provided by UV lamp. The relative proportions of solvents in chromatography solvent mixtures refer to the volume: volume ratio. Electronic absorption and fluorescence spectra in solution were acquired using a Shimadzu UV-3600 UV-Vis-NIR and Agilent Cary-100 spectrophotometers. Mass spectra were recorded on Waters Synapt G1 High Definition mass spectrometer.

2.2 *Synthesis*

2.2.1 *Synthesis of DCM Core*

*Synthesis of **1***

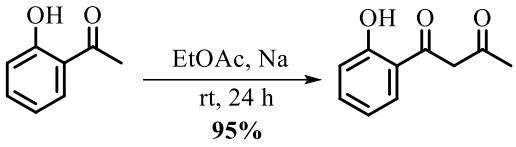

1

2-hydroxyacetophenone (5 g, 36.72 mmol) was dissolved in 50 mL dry ethyl acetate and the reaction mixture was stirred in an ice bath. Sodium was cut into pieces and added to the reaction mixture gradually. After being stirred for 24 h, the mixture was filtered and washed with cold ethyl acetate. After drying overnight compound **1** (6.25 g, 95% yield) was used without further purification.

*Synthesis of **2***

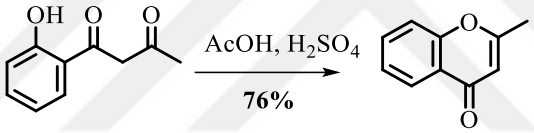

1 **2**

Compound **1** (6.95 g, 38.91 mmol) and 30 mL acetic acid were stirred for 15 min, and then 4.6 mL of sulfuric acid (4.6 mL) was slowly added to the solution. The mixture was refluxed for about 45 min and then mixture was poured into ice water. pH of the solution was adjusted to 7.0 with Na_2CO_3 addition. The aqueous solution was washed with dichloromethane and the organic phase was dried over Na_2SO_4, filtered, and concentrated under reduced pressure to brown solid (4.78 g, 76% yield). The crude product was directly used in the next reaction without further purification.

*Synthesis of **3***

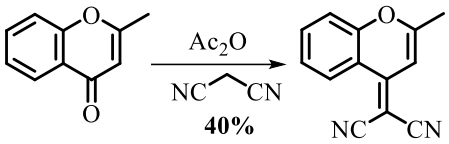

2 **3**

Compound **2** (4.78, 30 mmol) and malononitrile (7.8 g, 120 mmol) were dissolved in 15 mL of acetic anhydride. The mixture was refluxed for overnight and then the solvent was evaporated under reduced pressure. 20 mL of deionized water was added to the residue and refluxed for an additional hour. After cooling the reaction mixture to room temperature, the mixture was washed in an extraction funnel using dichloromethane. The organic phase was dried over Na_2SO_4, filtered, and concentrated. The crude product was purified by silica column chromatography using Hex:EtOAc (85:15, v/v) to yield compound **3** as a bright orange solid. (2.5 g, 40% yield)

^{1}H NMR (500 MHz, $CDCl_3$): δ 8.90 (d, *J* = 8.3 Hz, 1H), 7.72 (t, *J* = 8.5 Hz, 1H), 7.48 – 7.42 (m, 2H), 6.71 (s, 1H), 2.44 (d, 3H). ^{13}C NMR (126 MHz, $CDCl_3$): δ 161.8, 153.2, 152.9, 134.6, 126.0, 125.8, 118.7, 117.5, 116.6, 115.5, 105.5, 62.3, 20.8, 20.5.

*Synthesis of **DCM$_O$***

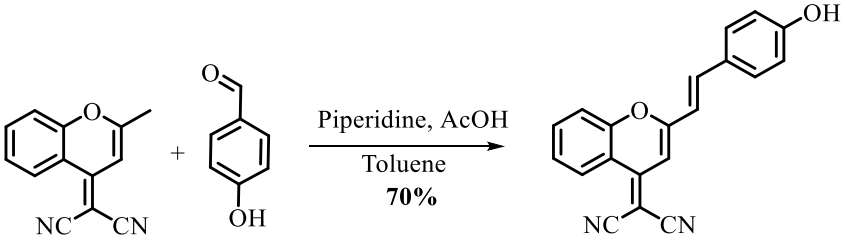

3 **DCM$_O$**

Compound **3** (150 mg, 0.72 mmol) and 4-hydroxy benzaldehyde (97.5 mg, 0.81 mmol) were dissolved in 20 mL of toluene. Piperidine (0.5 mL) and acetic acid (0.5 mL) were added to solution under inert atmosphere. The solution was heated under reflux for 16 hours. After the completion of the reaction, toluene was evaporated under reduced pressure. The residue was purified by silica gel chromatography with DCM to get **DCM$_O$** as red solid (180 mg, 70% yield).

^{1}H NMR (500 MHz, d_6-DMSO): δ 10.22 (s, 1H), 8.79 (dd, *J* = 8.3, 1.0 Hz, 1H), 8.00 (t, 1H), 7.85 (d, *J* = 8.4 Hz, 1H), 7.76 (d, *J* = 16.0 Hz, 1H), 7.73 – 7.63 (m, 3H), 7.33 (d, 1H), 7.02 (s, 1H), 6.92 (d, *J* = 8.6 Hz, 2H). ^{13}C NMR (126 MHz, d_6-DMSO): δ 163.0,

159.8, 158.5, 152.5, 151.7, 138.9, 134.9, 131.8, 130.0, 128.1, 125.8, 125.7, 124.3, 118.8, 117.1, 116.8, 115.8, 115.6, 105.4, 58.9.

*Synthesis of **4***

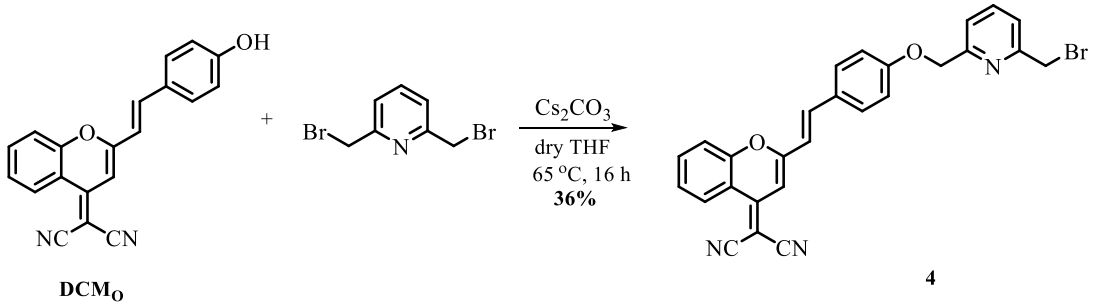

DCM_O **4**

DCM_O (140 mg, 0.45 mmol) and Cs_2CO_3 (220 mg, 0.67 mmol) were dissolved in 15 mL of dry THF. Then 2,6-bis(bromomethyl)pyridine (178 mg, 0.67 mmol) was added into the solution, the resulting mixture was refluxed for 16 hours under argon atmosphere. After the reaction was over, THF was evaporated and the residue was dissolved in ethyl acetate and washed with brine (50 mLx2). The organic layer was dried over Na_2SO_4, filtered and concentrated under reduced pressure. The crude product was purified by silica gel chromatography using DCM: MeOH (50:1, v/v) to get deep red solid (80 mg, 36% yield).

^{1}H NMR (500 MHz, d_6-DMSO): δ 8.73 (dd, *J* = 8.4, 1.4 Hz, 1H), 7.92 (t, *J* = 8.5 Hz, 1H), 7.89 (t, *J* = 7.8 Hz, 1H), 7.79 (d, *J* = 9.9 Hz, 1H), 7.75 (d, *J* = 6.6 Hz, 2H), 7.73 (d, *J* = 16.0 Hz, 1H), 7.61 (ddd, *J* = 8.4, 7.1, 1.3 Hz, 1H), 7.53 (d, *J* = 7.8 Hz, 1H), 7.48 (d, *J* = 7.8 Hz, 1H), 7.38 (d, *J* = 16.0 Hz, 1H), 7.15 (d, *J* = 9.0 Hz, 2 H), 6.99 (s, 1H), 5.25 (s, 2H), 4.72 (s, 2H). ^{13}C NMR (126 MHz, d_6-DMSO): δ 156.9, 156.8, 153.4, 143.3, 139.4, 139.0, 138.8, 138.4, 135.9, 135.4, 130.6, 130.6, 128.6, 128.1, 124.5, 123.5, 121.8, 121.7, 117.9, 117.8, 117.8, 117.7, 115.9, 115.9, 106.0, 64.5, 35.1. Mass spectrometry (ESI negative ion mode for $[M - H]^-$): Calcd. For $C_{27}H_{18}BrN_3O_2$: 495.0582, found: 496.0665.

*Synthesis of **DCM-Cu***

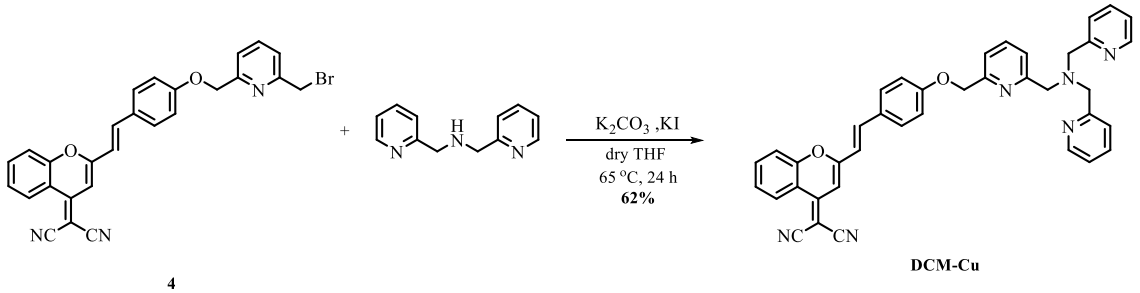

To a solution of compound **4** (50 mg, 0.1 mmol) in 8 mL of dry THF, K_2CO_3 (107 mg, 0.77 mmol), KI (4 mg, 0.028 mmol) and di(2-picolyl) amine (23 mg, 0.11 mmol) were added at room temperature. The reaction was refluxed overnight. After completion of the reaction, the mixture was condensed under reduced pressure. The crude product was purified by silica gel column chromatography using DCM:MeOH (50 : 1 to 50 : 2, v/v) to obtain **DCM-Cu** as brown solid. (38.5 mg, 62% yield)

^{1}H NMR (500 MHz, $CDCl_3$): δ 8.91 (dd, *J* = 8.3, 1.5 Hz, 1H), 8.54 (d, *J* = 4.8 Hz, 2H), 7.77 – 7.63 (m, 4H), 7.61 – 7.49 (m, 7H), 7.48 – 7.41 (m, 1H), 7.37 (d, *J* = 7.7 Hz, 1H), 7.16 (dd, *J* = 7.4, 5.0 Hz, 2H), 7.04 (d, *J* = 8.4 Hz, 2H), 6.83 (s, 1H), 6.67 (d, *J* = 15.9 Hz, 1H), 5.23 (s, 2H), 3.91 (d, *J* = 6.8 Hz, 6H).^{13}C NMR (126 MHz, $CDCl_3$): δ 160.5, 159.3, 159.2, 157.9, 155.8, 152.9, 152.3, 149.2, 138.6, 137.4, 136.5, 134.6, 129.7, 129.5, 127.8, 125.9, 125.8, 122.9, 122.1, 122.0, 119.6, 118.6, 117.8, 116.9, 116.5, 115.9, 115.5, 106.3, 70.8, 62.1, 60.1, 60.0, 31.9, 31.5, 30.2, 29.7, 29.7, 29.4, 22.7, 14.2 Mass spectrometry (ESI negative ion mode for $[M - H]^-$): Calcd. For $C_{39}H_{30}N_6O_2$: 614.2430, found: 615.1420.

*Synthesis of **5***

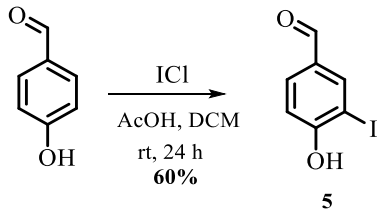

To a solution of ICl (1.26 g, 7.78 mmol) in DCM (5 mL) 4-hydroxy benzaldehyde (500 mg, 4.09 mmol) in 15 mL DCM was added dropwisw following by addition of acetic acid (1 mL). The reaction was stirred at room temperature for 24 hours. Upon completion, the mixture was quenched with saturated $Na_2S_2O_3$ solution. Organic phase was dried over

Na_2SO_4 and concentrated under reduced pressure. The compound **5** was obtained as white crystals through purification with column chromatography using DCM as eluent (610 mg, 60% yield).

^{1}H NMR (500 MHz, $CDCl_3$): δ 9.81 (s, 1H), 8.22 (d, *J* = 2.0 Hz, 1H), 7.79 (dd, *J* = 8.4, 1.9 Hz, 1H), 7.11 (d, *J* = 8.3 Hz, 1H). ^{13}C NMR (126 MHz, $CDCl_3$): δ 189.3, 159.9, 140.6, 132.3, 131.6, 115.4, 86.3, 77.3, 77.3, 77.0, 76.8. Mass spectrometry (ESI negative ion mode for $[M-H]^-$): calcd for $C_7H_5IO_2$ 247.9334, found: 246.9268

*Synthesis of **6***

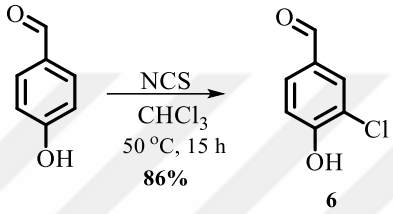

6

N-chlorosuccinimide (550 mg, 4.09 mmol) was added in portions to a solution of 4-hydroxy benzaldehyde (500 mg, 4.09 mmol) in 15 mL acetonitrile and the mixture was heated at 50 °C for 15 hours. Upon completion, the reaction was washed with brine and dried over Na_2SO_4. The compound **6** was obtained as off white solid through purification with column chromatography using DCM as eluent (555 mg, 86% yield).

^{1}H NMR (500 MHz, $CDCl_3$): δ 9.85 (s, 1H), 7.90 (d, *J* = 2.0 Hz, 1H), 7.75 (dd, *J* = 8.4, 1.9 Hz, 1H), 7.16 (d, *J* = 8.4 Hz, 1H), 6.29 (s, 1H). ^{13}C NMR (126 MHz, $CDCl_3$): δ 188.4, 152.8, 130.2, 129.8, 122.2. Mass spectrometry (ESI negative ion mode for $[M-H]^-$): calcd for $C_7H_5ClO_2$ 155.9978, found: 154.9911

2.2.2 *Synthesis of DCM_O Derivative Activatable Photosensitizers*

*Synthesis of **7***

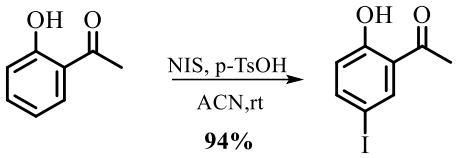

7

2-hydroxyacetophenone (2.2 g, 16.6 mmol) and *p*-toluenesulfonic acid (2.8 g, 16.6 mmol) were dissolved 10 mL ACN. After 5 minutes of stirring, *N*-Iodosuccinimide (3.7 g, 16.6 mmol) was added portion wise at room temperature. The solution was allowed to stir overnight at 40 °C. Reaction was cooled down to room temperature and ACN was removed under reduced pressure. The crude was diluted with 150 mL EtOAc and the mixture was washed with saturated sodium thiosulfate solution. Organic layer was separated, dried over Na_2SO_4 and the solvent was evaporated under reduced pressure. The crude product was purified by column chromatography on silica gel Hex:EtOAc (85:15, v/v) to give compound **7** as a yellowish solid. (4.1 g, 94% yield).

^{1}H NMR (500 MHz, $CDCl_3$): δ 12.11 (s, 1H), 7.93 (s, 1H), 7.62 (d, *J* = 8.9 Hz, 1H), 6.69 (s, 1H), 2.56 (s, 3H). ^{13}C NMR (126 MHz, $CDCl_3$): δ 202.4, 160.9, 143.7, 138.2, 120.7, 119.9, 78.8, 25.5.

*Synthesis of **8***

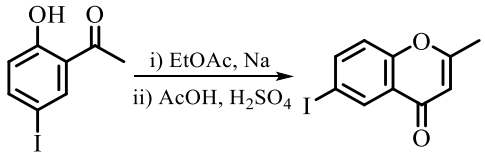

7 **8**

To a solution of Compound **7** (4.1 g, 15.6 mmol) in dry ethyl acetate (80 mL) sodium (5 g) was added as small pieces. The suspension was stirred overnight at room temperature. The solution was filtered and the brown solid was dissolved in 100 mL distilled water. Acidification of the solution with 1 N HCl was done to adjust pH to 7.0. Solution was washed with 250 mL of EtOAc, the organic layers were dried over Na_2SO_4, filtered, and concentrated to give crude product as a brown solid, which was directly used in the next reaction without further purification. To a solution of the crude product in acetic acid (30 mL) was slowly added sulfuric acid (2.5 mL). The mixture was heated to

120 °C for about 0.5 h. After cooling to room temperature, the solution was poured into an ice bath; pH was adjusted to 7.0 with slow Na_2CO_3 and dilute NaOH. The solution was washed with DCM (250 mL) in an extraction funnel, the organic layers were dried over Na_2SO_4, filtered, and evaporated to dryness. The residue was purified on silica gel with Hex:EtOAc (90:10, v/v) as an eluent to get compound **8** as a brown solid. (1.6 g, 57% yield)

^{1}H NMR (500 MHz, $CDCl_3$): δ 8.49 (d, *J* = 2.2 Hz, 1H), 7.89 (dd, *J* = 8.8, 2.2 Hz, 1H), 7.18 (d, *J* = 8.8 Hz, 1H), 6.18 (s, 1H), 2.38 (s, 3H). ^{13}C NMR (126 MHz, $CDCl_3$): 176.6, 166.5, 155.9, 141.9, 134.5, 125.2, 119.9, 110.7, 88.7, 20.5.

*Synthesis of **9***

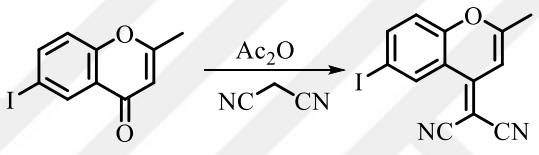

8 **9**

Compound **8** (50 mg, 0.001 mmol) and malononitrile (57 mg, 12.87 mmol) were dissolved in 2.5 mL acetic anhydride, the solution was refluxed overnight. After completion, 10 mL methanol was added to solution and refluxed for another 3 hours. The solvent was evaporated under vacuum and the residue was purified on silica gel with Hex:EtOAc (80:20, v/v) as an eluent to get compound **9** as a dark-reddish solid. (30 mg, 51% yield)

^{1}H NMR (500 MHz, $CDCl_3$): δ 9.14 (d, *J* = 2.0 Hz, 1H), 7.90 (dd, *J* = 8.8, 2.0 Hz, 1H), 7.13 (d, *J* = 8.8 Hz, 1H), 6.64 (d, *J* = 0.9 Hz, 1H), 2.35 (s, 4H).^{13}C NMR (126 MHz, $CDCl_3$): δ 160.5, 151.4, 150.1, 142.2, 133.3, 119.3, 118.4, 114.9, 113.9, 104.6, 88.4, 62.4, 19.4. Mass spectrometry (ESI negative ion mode for $[M-H]^-$): calcd for $C_{13}H_7IN_2O$ 333.9603, found: 333.9600

Synthesis of ***I-DCM$_O$-Cl***

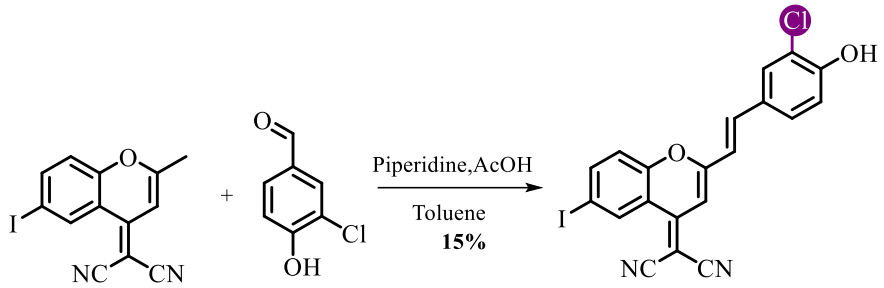

9 **6** **I-DCM$_O$-Cl**

Compound **9** (41.5 mg, 125 mmol) and compound **6** (20 mg, 125 mmol) were dissolved in 8 mL toluene and then piperidine (12 µL) and acetic acid (12 µL) were added to the solution under argon atmosphere at room temperature. The solution was refluxed overnight. The solvent was evaporated in *vacuo*. The obtained crude product was purified by silica column chromatography to get DCM **I-DCM$_O$-Cl** as orange solid (9 mg, 15% yield).

^{1}H NMR (500 MHz, d_6-DMSO): δ 9.10 (d, *J* = 2.0 Hz, 1H), 8.27 (dd, *J* = 8.9 Hz, 1H), 7.91 (d, 1H), 7.73 (d, *J* = 15.9 Hz, 1H), 7.64 (d, 1H), 7.59 (dd, 1H), 7.44 (d, *J* = 15.9 Hz, 1H), 7.09 (d, *J* = 8.5 Hz, 1H), 7.03 (s, 1H).^{13}C NMR (126 MHz, d_6-DMSO): δ 158.9, 152.2, 151.7, 143.8, 138.5, 133.4, 130.0, 129.5, 127.7, 121.5, 121.2, 119.7, 117.5, 116.1, 106.8, 90.8. Mass spectrometry (ESI negative ion mode for $[M-H]^-$): calcd for $C_{20}H_{10}IN_2O_2Cl$ 471.9475, found: 470.9417

Synthesis of ***DCM$_O$-I***

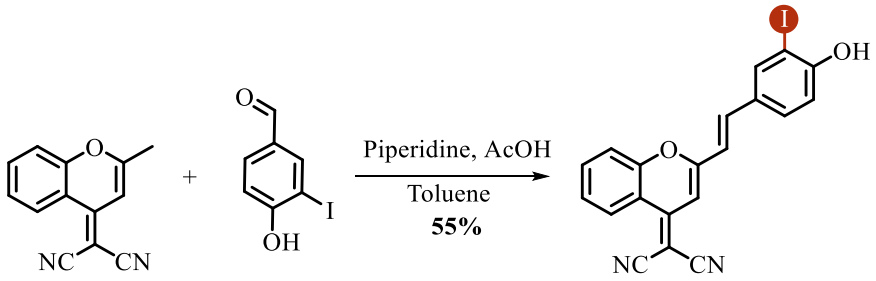

3 **5** **DCM$_O$-I**

Compound **3** (35 mg, 168 mmol) and compound **5** (40 mg, 168 mmol) were dissolved in 10 mL toluene and piperidine (16 µL) and acetic acid (16 µL) were added to the solution under argon atmosphere at room temperature. Then, the mixture was refluxed for 16 hours and the solvent was evaporated in *vacuo*. The obtained crude product was

purified by silica column chromatography with DCM to DCM: MeOH (50:1.5, v/v) to get **DCM$_O$-I** as orange solid (40 mg, 55% yield).

^{1}H NMR (500 MHz, d_6-DMSO): δ 11.09 (s, 1H), 8.79 (dd, *J* = 8.4, 1.5 Hz, 1H), 8.25 (d, *J* = 2.2 Hz, 1H), 7.98 (ddd, *J* = 8.6, 7.2, 1.5 Hz, 1H), 7.83 (dd, *J* = 8.5, 1.3 Hz, 1H), 7.71 (d, *J* = 16.0 Hz, 1H), 7.67 (dtt, *J* = 10.3, 4.4, 2.2 Hz, 2H), 7.42 (d, *J* = 15.9 Hz, 1H), 7.04 (s, 1H), 7.00 (d, *J* = 8.4 Hz, 1H). ^{13}C NMR (126 MHz, d_6-DMSO): δ 159.3, 159.0, 153.4, 152.5, 139.2, 137.9, 135.8, 130.8, 128.8, 126.0, 125.1, 119.5, 117.8, 117.6, 117.6, 116.4, 115.7, 106.6, 86.2, 60.0. Mass spectrometry (ESI positive ion mode for $[M+H]^+$): Calcd. For $C_{20}H_{11}IN_2O_2$ 437.9865, found 438.9948.

*Synthesis of **DCM$_O$-I-Cys***

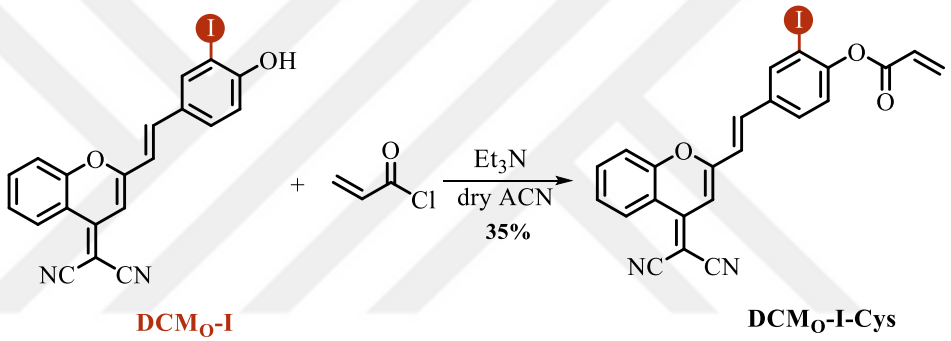

DCM$_O$-I **DCM$_O$-I-Cys**

DCM$_O$-I (40 mg, 91 mmol) and acryolyl chloride (34 mg, 365 mmol) in the presence of triethyl amine (25 mg, 250 mmol) were dissolved in 10 mL of dry ACN at room temperature and stirred for 0.5 h. Then, the solvent was evaporated in vacuo. The obtained crude product was purified by silica column chromatography chromatography with DCM: Hex (70:30, v/v) get **DCM$_O$-I-Cys** as dark orange solid (15 mg, 35% yield).

^{1}H NMR (500 MHz, $CDCl_3$): δ 8.92 (dd, *J* = 8.4, 1.5 Hz, 1H), 8.07 (d, *J* = 2.1 Hz, 1H), 7.76 (ddd, *J* = 8.6, 7.2, 1.5 Hz, 1H), 7.62 – 7.55 (m, 2H), 7.52 (s, 1H), 7.47 (ddd, *J* = 8.4, 7.1, 1.3 Hz, 1H), 7.24 (d, *J* = 8.4 Hz, 1H), 6.89 (s, 1H), 6.79 (dd, *J* = 15.9, 1.4 Hz, 1H), 6.73 (dd, *J* = 17.3, 1.2 Hz, 1H), 6.38 (dd, *J* = 17.3, 10.5 Hz, 1H), 6.13 (dd, *J* = 10.5, 1.1 Hz, 1H). ^{13}C NMR (126 MHz, $CDCl_3$): δ 163.3, 156.6, 152.6, 152.4, 152.3, 138.8, 138.5, 135.9, 134.8, 134.3, 134.0, 128.6, 127.3, 126.1, 125.9, 123.5, 120.0, 118.6, 117.8, 116.5, 115.5, 107.5, 91.2, 63.72. Mass spectrometry (ESI positive ion mode for $[M+H]^+$): Calcd. For $C_{23}H_{13}IN_2O_3$ 492.27, found 493.0042.

2.2.3 *Synthesis of DCM$_S$ Derivative Activatable Photosensitizers*

*Synthesis of **10***

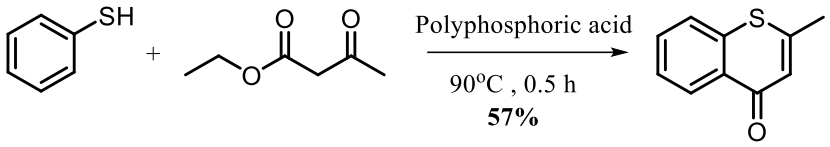

10

Ethyl acetoacetate (2.6 g, 20 mmol) and polyphosphoric acid (24 mL) were heated at 90 °C for 0.5 h and benzenethiol (2.2 g, 20 mmol) was added to the mixture at this temperature dropwise. The reaction was stirred for another 0.5 h and then the mixture was poured into an ice water bath. The crude mixture was dissolved in ethyl acetate (500 mL) and washed with brine (500 mL). Organic layer was separated and dried over Na_2SO_4. The solvent was evaporated under vacuum and the crude mixture was used for the next step without further purification. (2 g, 57 % yield)

^{1}H NMR (500 MHz, $CDCl_3$): δ 8.48 (d, *J* = 8.1 Hz, 1H), 7.59 – 7.52 (m, 2H), 7.52 – 7.47 (m, 1H), 6.83 (s, 1H), 2.44 (s, 3H). ^{13}C NMR (126 MHz, $CDCl_3$): δ 180.9, 151.6, 138.0, 131.7, 131.0, 128.9, 127.8, 126.3, 125.2, 23.6. Mass spectrometry (ESI positive ion mode for $[M+H]^+$): Calcd. for $C_{10}H_8OS$ 176.0296, found 177.0377.

*Synthesis of **11***

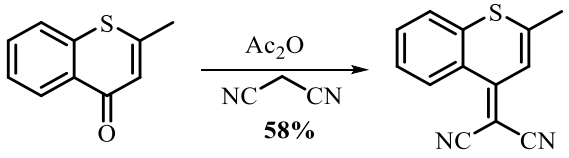

10 **11**

Compound **10** (500 mg, 3.12 mmol) and malononitrile (1.9 g, 32 mmol) were dissolved in Ac_2O (10 mL). The mixture was refluxed for 4 h. After that, 15 mL methanol was added and the reaction mixture was refluxed for another 2 h. Then the solvent was evaporated under vacuum. The crude product was purified by silica gel chromatography Hex:EtOAc (85:15, v/v) to give compound **11** as a brown solid (350 mg, 58% yield).

^{1}H NMR (500 MHz, $CDCl_3$): δ 8.95 (d, *J* = 7.9 Hz, 1H), 7.66 – 7.55 (m, 3H), 7.41 (s, 1H), 2.53 (s, 3H). ^{13}C NMR (126 MHz, $CDCl_3$): δ 156.3, 149.2, 136.4, 132.2, 128.8, 128.7, 127.4, 125.3, 121.0, 117.3, 116.0, 23.8. Mass spectrometry (ESI positive ion mode for $[M+H]^+$): calcd for $C_{13}H_8N_2S^+$ 224.0410, found: 224.0433.

Synthesis of **DCM$_S$-Cl**

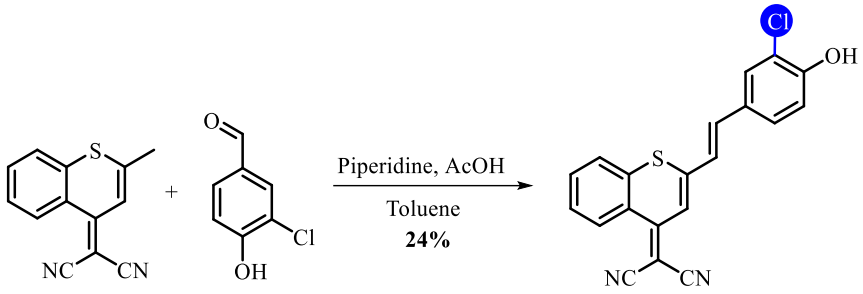

11 **6** **DCM$_S$-Cl**

Compound **11** (25 mg, 112 mmol) and compound **6** (25 mg, 160 mmol) were dissolved in 8 mL toluene with piperidine (20 µL) and acetic acid (20 µL) under argon atmosphere at room temperature. Then, the mixture was refluxed for 16 hours and the solvent was evaporated in *vacuo*. The crude product was diluted with EtOAc (100 mL) and washed with 0.1 N HCl (50 mL). The organic layer was separated, washed with brine, dried over Na_2SO_4 and evaporated under reduced pressure. The residue was purified by column chromatography on silica gel with DCM to get **DCM$_S$-Cl** as a dark brown solid (10 mg, 24% yield).

^{1}H NMR (500 MHz, d_6-DMSO): δ 8.83 (dd, *J* = 8.4, 1.3 Hz, 1H), 8.05 (dd, *J* = 8.2, 1.3 Hz, 1H), 7.96 (d, *J* = 2.1 Hz, 1H), 7.89 – 7.84 (m, 1H), 7.78 (ddd, *J* = 8.5, 7.1, 1.4 Hz, 1H), 7.70 (d, *J* = 16.1 Hz, 1H), 7.68 (s, 1H), 7.62 (dd, *J* = 8.6, 2.2 Hz, 1H), 7.39 (d, *J* = 16.2 Hz, 1H), 7.05 (d, *J* = 8.4 Hz, 1H). ^{13}C NMR (126 MHz, d_6-DMSO): δ 156.2, 149.1, 136.7, 134.9, 133.1, 129.8, 129.4, 128.9, 128.5, 128.1, 125.1, 124.3, 121.2, 121.0, 117.4. Mass spectrometry (ESI negative ion mode for $[M-H]^-$): calcd for $C_{20}H_{11}ClN_2OS^-$ 362.0281, found: 361.0219

Synthesis of **DCMs-I**

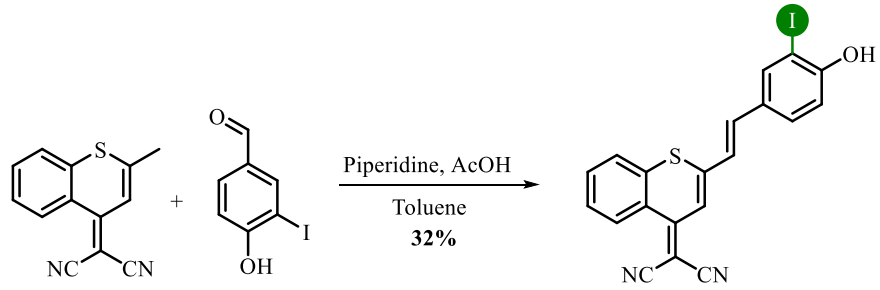

11 **5** **DCM$_S$-I**

Compound **11** (57 mg, 255 mmol) and compound **5** (56 mg, 228 mmol) were dissolved in 8 mL toluene and then piperidine (25 µL) and acetic acid (25 µL) were added under argon atmosphere at room temperature. The resulting mixture was refluxed for 24 hours and the solvent was evaporated in *vacuo*. The crude product was diluted with EtOAc (100 mL) and washed with 0.1 N HCl (50 mL). The organic layer was separated, washed with brine, dried over Na_2SO_4 and solvent was evaporated under reduced pressure. The residue was purified by column chromatography on silica gel with DCM to get **DCMs-Cl** as a light orange solid (38 mg, 24% yield).

^{1}H NMR (500 MHz, d_6-DMSO): δ 10.96 (s, 1H), 8.76 (d, *J* = 8.3 Hz, 1H), 8.21 (s, 1H), 7.98 (d, *J* = 8.1 Hz, 1H), 7.80 (d, *J* = 15.1 Hz, 1H), 7.72 (d, *J* = 15.6 Hz, 1H), 7.62 (d, *J* = 16.2 Hz, 3H), 7.31 (d, *J* = 16.3 Hz, 1H), 6.92 (d, *J* = 8.4 Hz, 1H). ^{13}C NMR (126 MHz, d_6-DMSO): δ 159.0, 156.2, 149.1, 138.9, 136.4, 134.9, 133.1, 130.6, 128.9, 128.4, 128.2, 125.0, 124.2, 121.1, 117.9, 116.4, 115.5, 86.1, 67.5, 66.8, 25.6. Mass spectrometry (ESI negative ion mode for [M-H]-): calculated for $C_{20}H_{11}IN_2OS$-: 453.9637, found: 452.9565

Synthesis of ***12***[92]

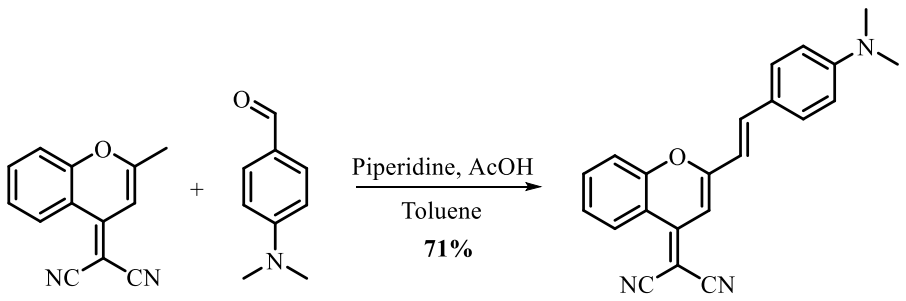

3 **12**

Compound **3** (80 mg, 0.38 mmol) and 4-hydroxy benzaldehyde (57.3 mg, 0.38 mmol) were dissolved in 20 mL of toluene. Piperidine (85 µL) and acetic acid (40 µL) were

added to solution under inert atmosphere. The solution was heated to reflux for 20 hours. After reaction was completed, toluene was evaporated under vacuum. The residue was purified by silica gel chromatography with dichloromethane to get **12** as green solid (93 mg, 71% yield).

^{1}H NMR (500 MHz, $CDCl_3$): δ 8.90 (dd, *J* = 8.4, 1.4 Hz, 1H), 7.70 (ddd, *J* = 8.5, 7.0, 1.4 Hz, 1H), 7.57 (d, *J* = 16 Hz, 1H), 7.52 (dd, *J* = 8.5, 1.3 Hz, 1H), 7.49 – 7.45 (m, 2H), 7.41 (m, 1H), 6.77 (s, 1H), 6.72 – 6.68 (m, 2H), 6.56 (d, *J* = 16 Hz, 1H), 3.07 (s, 6H). ^{13}C NMR (126 MHz, $CDCl_3$): δ 158.9, 152.9, 152.4, 151.9, 139.9, 134.2, 129.9, 125.8, 125.6, 122.5, 118.5, 118.1, 117.5, 116.4, 112.9, 112.0, 105.3, 60.3, 40.1.

2.3 *Photophysical Characterization*

2.3.1 *Photophysical Characterization of DCM Derivatives*

All DCM probes were used at a final concentration of 10 μM. Absorption and fluorescence spectra were performed in a 3 mL, 1 cm cuvette, using a total volume of PBS buffer (pH 7.4) with varying DMSO amounts. In all fluorescence measurements, both excitation and emission slit widths were set to 10 nm.

Fluorescence Quantum Yield Calculations:

The fluorescence quantum yield measurements of **DCM-Cu, $\mathbf{DCM_O}$** and **$\mathbf{DCM_S}$** aPSs were carried out using Compound **12** (quantum yield was reported as 59.58% in DCM)[92] as the reference. For both measurements, the samples were dissolved in DMSO (10 mM, containing 1% PBS) and absorbance values of samples at their excitation wavelengths were kept less than 0.1. Yield calculation was done by using the following formula;

$$\mathbf{QY}_{sample} = \mathbf{QY}_{standard} \frac{\boldsymbol{F}_{sample}\, \boldsymbol{A}_{standard}\, \boldsymbol{n}^2_{sample}}{\boldsymbol{F}_{standard}\, \boldsymbol{A}_{sample}\, \boldsymbol{n}^2_{standard}}$$

Where, QY_{sample} and $QY_{standard}$ are the fluorescence quantum yields of the sample and the standard (Compound **12**), respectively. F_{sample} and $F_{standard}$ are the integrated fluorescence emission of the sample, A_{sample} and $A_{standard}$ represent the absorbance of the sample and standard at their respective excitation wavelengths. Measurements were carried out in 1 cm quartz cuvettes with a total sample volume of 3 mL.

pH titration:

pH dependent absorption and fluorescence spectrum of **DCM$_O$** and **DCM$_S$** derivatives were evaluated by using solutions buffered at different pHs: (glycine (pH 2.5-3.5), sodium acetate (pH 4.0- 5.5), MES (6.0-6.8), PBS (pH 7.2-8.2) and carbonate (pH 9.2-10.0) in 50 mM concentration). Aqueous solutions with different pH values of **DCM$_O$** and **DCM$_S$** with final concentration 10 μM and final DMSO amount %50 were prepared. Absorption and emission of these solutions were recorded.

Singlet Oxygen Detection Experiments:

Singlet oxygen generation capacities of **DCM, DCM$_O$** and **DCMs** in solution were determined by using 1,4-diphenylbenzofuran (DPBF) as a trap molecule in DMSO–PBS buffer (10 mM, pH 7.4, 1:1, v/v). Methylene blue ($\Phi\Delta$ = 0.49 in DMSO)[93] was used as a reference compound for singlet oxygen quantum yield calculations. **DCM, DCM$_O$** and **DCMs** were mixed in oxygen bubbled PBS and DMSO. The solutions were exposed to LED light source of 630 nm from 15 cm distance and 20 second time interval for all the samples. The absorbance of DPBF was determined after each irradiation to evaluate producing $^1O_2$. Singlet oxygen quantum yields were calculated according to the equation given below:

$$\phi_{\Delta sample} = \phi_{\Delta standard} \left(\frac{1-10^{-A_{std}}}{1-10^{-A_{sam}}}\right)\left(\frac{m_{sample}}{m_{standard}}\right)$$

Where, ϕ_{sample} and $\phi_{standard}$ represent **DCM, DCM$_O$** and **DCMs** derivatives and methylene blue respectively. m is the slope of absorbance maxima of DPBF at 414 nm versus time graph. A is the absorbance value of both sample and standard at irradiation wavelength, 630 nm.

HPLC Kinetic Profile:

HPLC analysis was performed using RP-HPLC System with UV-Vis detection and a reversed-phase C18 column (4 μm, 4.6 × 150 mm). The data collection and analysis were carried out using the Chemstation software. The oven temperature was maintained at 25 ℃, the injection volume was 20 μL and the flow rate was 1.0 mL/min with detection

wavelength at 480 nm. The separation program of gradient elution was as follows ; where solvent A was water with 0.1% TFA and solvent B was acetonitrile.

Table 2 RP-HPLC Conditions

Time/min	Phase A/%	Phase B/%
0	10.0	5.0
7.0	5.0	95.0
13.0	5.0	95.0
16.0	95.0	5.0

2.4 *In Vitro Experiments*

Cell Culture and Treatments:

Human cervical cancer cells (HeLa) and mouse fibroblast cells (L929) were cultured in DMEM high glucose supplemented with 10% heat inactivated fetal bovine serum (FBS),1% penicilin/stremptomycin, 0.5% amphothericin B and 2 mM glutamine in a humidified atmosphere at 37ºC with 5% CO_2. Cells were subcultured at 80–90% confluency in every 2-3 days. For photodynamic therapy, cells were treated with various concentrations (0.02-10 µM) of **DCM_O-I** or **DCM_O-I-Cys** for 1 or 2 h at dark, followed by LED light (595 nm, 9.83 mW/cm^2) illumination for 2 h (with fresh media), then kept at incubator up to 24 h at dark. For the dark toxicity, cells were treated under same conditions without any LED illumination and incubated up to 24 h, and then cell viability analysis were held.

Copper Targeted Imaging.

Cells (2 x10^4 /well) were seeded on 96 well plates and incubated for 24hours.Then, treated with increasing concentrations (1, 5 or 10 µM) of DCM-Cu alone or pretreated with copper (II) chloride ($CuCl_2$) 100 µM for 4 h, followed by incubation with DCM-Cu in fresh media for 15, 30 and 60 min at dark. After incubation periods, cells were washed twice with 1X PBS and fixed with 4% paraformaldehyde for 15-20 min at RT. After three washes with 1X PBS, cells nuclei were stained with Hoechst 33342 (1 µg/ml in PBS) and confocal images were taken at 361⁄497 nm (ex/em) and 550/680-704 (ex/em) wavelenghts for Hoechst and DCM-Cu by Zeiss LSM 900 CLSM, respectively. (10X) (n=3)

Cell Viability Assay:

Cells (3 x10^4/well) were seeded on 96 well plates and incubated for 24 hours.Then, treated with **DCM$_O$-I** or **DCM$_O$-I-Cys** according to the PDT protocol. After incubation periods, cells media was removed and 100 µL fresh medium containing MTT (0.5 mg/mL) was added to each well, then incubated at 37°C for 2-4 h. After incubation period, formazan crystals were dissolved with equal volumes of 10% SDS in PBS (0.01 N HCl) at 37°C, overnight. The absorbance of each well was measured at a wavelength of 490 and 570 nm using a microplate reader (MultiskanSky, Thermo Scientific, USA). (n=6)

Cellular Internalization Assay:

Cells were seeded on 35 mm glass bottom confocal dishes (1x10^4), then treated with **DCM$_O$-I** or **DCM$_O$-I-Cys** (2 µM) for 30 min, 1 or 2 h at 37°C. After incubation period, cells were washed three times with 1X PBS and fixed with 4% paraformaldehyde for 15-20 min at RT. After three washes with 1X PBS, cells nuclei were stained with Hoechst 33342 (2 µg/ml in PBS) and confocal images were taken at 361⁄497 nm (ex/em) and 550/680-704 (ex/em) wavelengths for Hoechst and **DCM$_O$-I** or **DCM$_O$-I-Cys** by Zeiss LSM 900 CLSM, respectively. (40X) (n=3)

ROS Generation Assay:

Cells were treated with the IC_{50} values of **DCM$_O$-I** or **DCM$_O$-I-Cys** for 2 h at dark, then illuminated with LED light for 2 h in the presence or absence of increasing concentrations of scavengers for ROS (*N*-acetylcysteine, NAC) or singlet oxygen (Sodium azide, NaN_3 then incubated up to 24 h at dark for MTT analysis. For confocal imaging, cells were seeded at a density of 2 × 10^4 cells/well on 96 well plates and treated with **DCM$_O$-I** or **DCM$_O$-I-Cys** for 2 h at dark and illuminated with LED in the presence or absence of NAC or NaN3 for 2 h. After illumination cells were washed twice with 1X PBS, then stained with DCFH-DA (20 µM), PI (10 µg/ml) and Hoechst 33342 (2 µg/ml) in serum free media for 30-45 min. After washing steps with 1XPBS, confocal images were taken at 488/535 nm (ex/em), 550/617 nm (ex/em) and 361⁄497 nm (ex/em) wavelengths for DCF, PI and Hoechst by Zeiss LSM 900 CLSM, respectively (Carl Zeiss, Oberkochen, Germany). Six images of duplicate wells were taken for each experiment (10X).

AO/Etbr Staining For Apoptosis and Necrosis:

Cells were seeded at a density of 2×10^4 cells/well on black walled, clear bottom 96 well plates and treated with **DCM_O-I** or **DCM_O-I-Cys** and additional 2 h w/wo LED illumination. After illumination period, cells were kept at 37°C for 30 min and washed twice with 1X PBS. Equal volumes of AO (1 µg/mL) and EtBr (1 µg/mL) in serum free media was added after the last wash and incubated for 30 min at 37 °C. Cells were washed with 1X PBS and images were taken at 500/525 (ex/em) and 530/617 nm (ex/em) wavelengths by Zeiss LSM 900 CLSM (Carl Zeiss, Oberkochen, Germany). Six images of duplicate wells were taken for each experiment (10X).

Statistical Analysis:

MTT results were expressed as the percentages of DMSO treated vehicle controls. IC_{50} values were calculated by the concentration-normalized response curves obtained from non-linear regression analysis. One-way analysis of variance (ANOVA) with Tukey post hoc tests were performed using GraphPad Prism 8.0 Software for viability and scavenger assays. Data were expressed as mean ± SD and values of $p<0.05$, $p<0.01$ and $p<0.001$ were considered as statistically significant.

Chapter 3:
RESULTS AND DISCUSSION

3.1 *DCM-Cu as a Selective Fluorescent Probe*

3.1.1 *Synthesis of DCM-Cu*

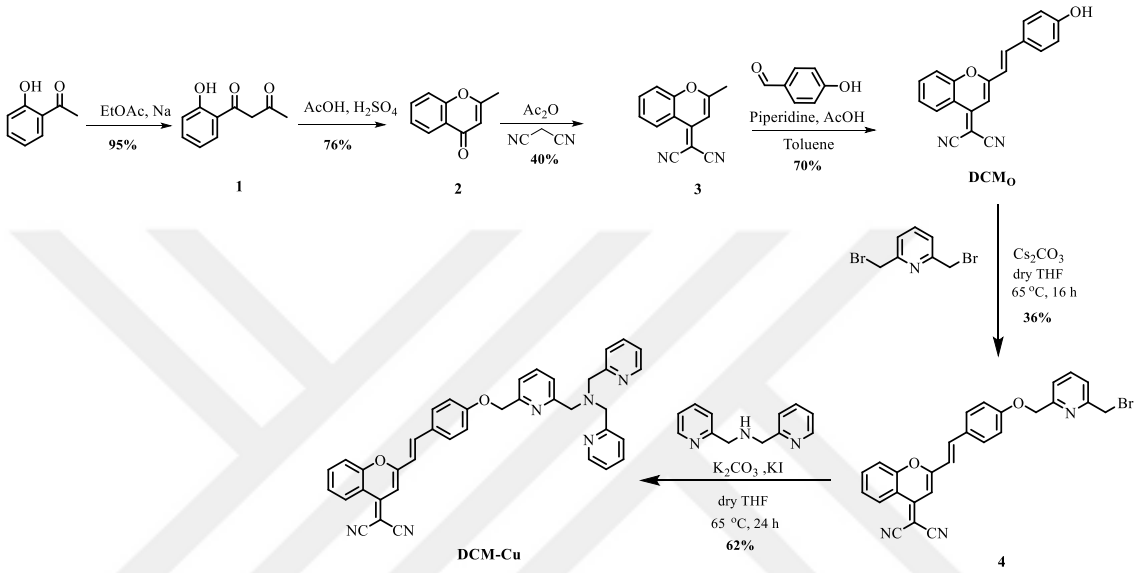

Figure 3.1 Synthetic route for **DCM-Cu**

DCM_O was synthesized according to the literature report[94] as shown in Figure 3.1. In the first step, 2-hydroxyacetophenone formed an enolate with sodium metal and then reacted with ethyl acetate to get compound **1**. After that, intramolecular condensation took place under acidic conditions (**2**). The key intermediate, compound **3**, was obtained by Knoevenagel condensation reaction between malononitrile and compound **2**. Then, the D-π-A type pyran derivative DCM_O was obtained in high yields by classical Knoevenagel condensation with the reaction of compound **3** and 4-hydroxy benzaldehyde. The masking group, TPA unit, was introduced to DCM_O after two successful substitution reactions. **DCM-Cu** was synthesized with 30% yield overall, and the final probe was fully characterized by ^{1}H, ^{13}C NMR and mass spectroscopy.

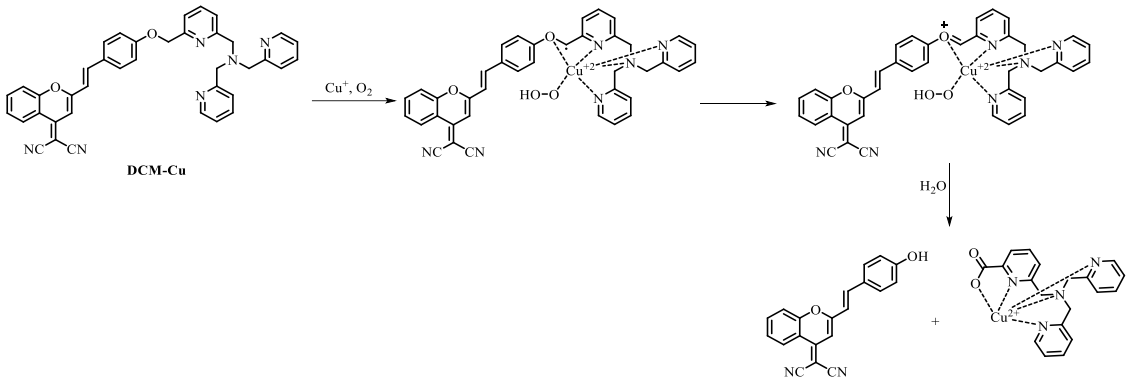

Figure 3.2 Response mechanism of **DCM-Cu** to Cu^{+} analyte

The selective Cu^{+}-dependent oxidative C-O etheric bond cleavage of the TPA unit leads to a fluorescent response of DCM_O. Cu^{+} binding to TPA [to produce an initial Cu^{+} – **DCM-Cu** tetrahedral complex] causes an oxidative cleavage of the pendant ether bond, releasing the latent dye and Cu^{2+}–TPA, resulting in a trigonal bipyramidal geometry change. (Figure 3.2)

3.1.2 *Photophysical Characterization of DCM-Cu*

After synthesizing **DCM-Cu**, its response to Cu^{+} (*introduced as* $[Cu(CH_3CN)_4]PF_6$) was tested. In this direction, **DCM-Cu** was dissolved in DMSO with a final concentration of 10 µM. All the UV-Vis absorption and fluorescence spectra measurements were performed in a 3 mL total volume and a 1 cm quartz cuvette containing PBS-DMSO buffer solution (1:1, v/v, pH=7.4, 2 mM glutathione). The photophysical experiments were tested in PBS-DMSO buffer solution that contains glutathione to mimic the reductive intracellular environment.

In the caged form, DCM-Cu exhibited a strong absorption signal centered at 450 nm. Upon addition of Cu^{+} (50 µM), the signal intensity at 445 nm decreased, while a new red shifted peak appeared around 560 nm (Figure 3.3a, Table 3). Accordingly, two different excitation wavelengths were utilized for **DCM-Cu** to show its ratiometric imaging capability in fluorescence measurements. Excitation at 535 nm resulted in a turn-on response in NIR fluorescent peak at 685 nm (Figure 3.3b, Table 3). On the other side, when excited from the isobestic point (460 nm), the probe showed a new broad fluorescence signal with two distinct shoulders at 560 and 685 nm and a decrease in intensity at 540 nm (Figure 3.3c).

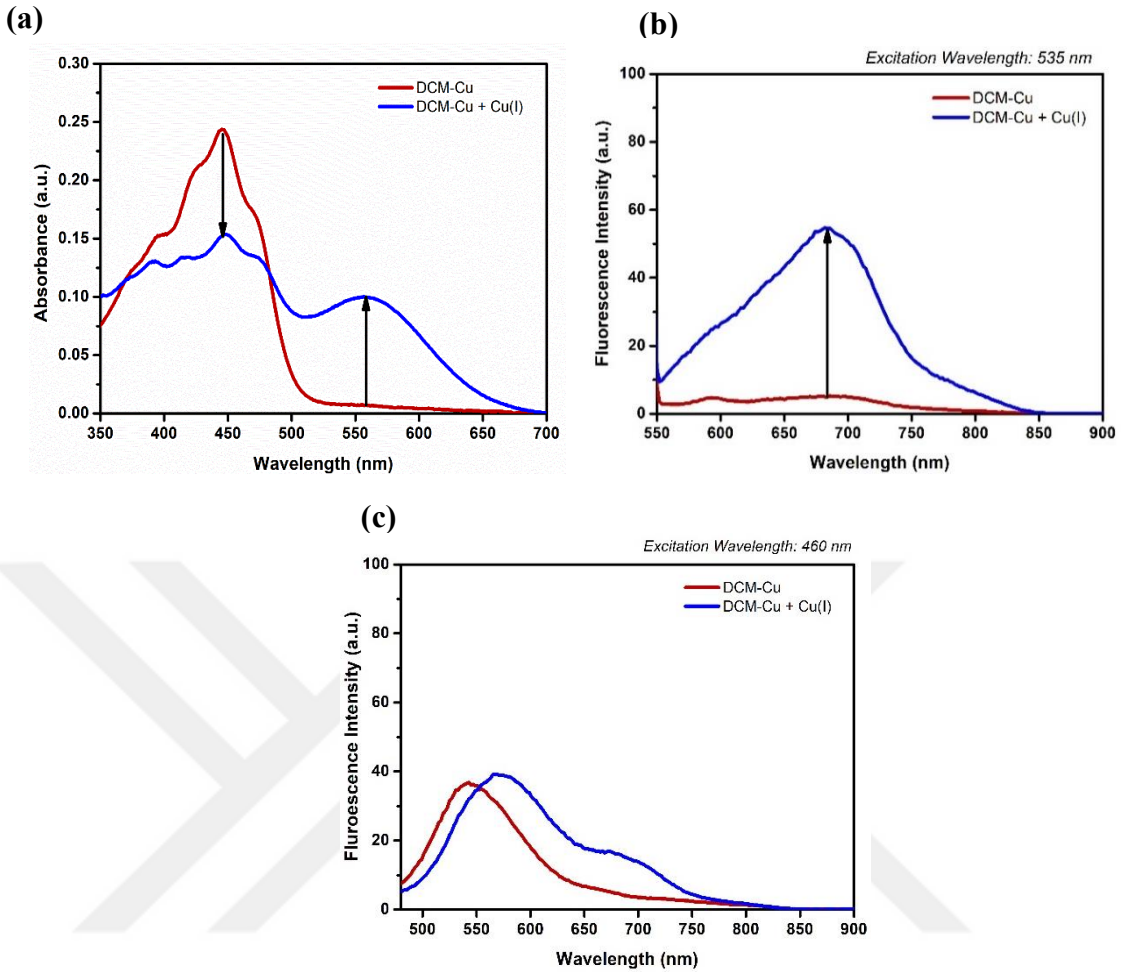

Figure 3.3 (a) The absorption and (b) fluorescence spectra of **DCM-Cu** (10 µM) with addition of Cu^+ (50 µM) in PBS-DMSO buffer solution, λ_{ex} = 535 nm, (1:1, v/v, pH=7.4, 2 mM glutathione) and (c) Fluorescence spectra of **DCM-Cu** (10 µM) after adding Cu^+ 50 µM) in PBS-DMSO buffer solution, λ_{ex} = 450 nm, (1:1, v/v, pH=7.4, 2 mM glutathione) λ_{ex} = 460 nm, the slit widths were 10 nm.

Table **3** Photophysical properties of **DCM-Cu** and **DCM-Cu+ Cu^+**

	λ_{abs} (nm)[(a)]	**λ_{em} (nm) [(a)]**	**ε ($M^{-1}cm^{-1}$) [(a)]**	**ϕ_F (%)[b]**
DCM-Cu	445	n.d	24370	1.39
DCM-Cu + Cu^+	560	685	10000	6.99

[(a)] Measured in PBS-DMSO buffer solution (1:1, v/v, pH=7.4) [(b)] The fluorescence quantum yield measurement was carried out using Compound **12** in DCM (quantum yield was reported as 0.5958 in DCM)

For further investigation, the kinetic studies of the probe with addition of the analyte were also performed via determining the changes in both absorbance and fluorescence spectrum. Upon addition of Cu^{+} (50 µM), a time dependent decrease in the absorption signal at 445 nm and appearance of a new signal at 560 nm were detected (Figure 3.4a). The NIR fluorescence signal at 685 nm increased rapidly and reached its plateau after 80 min (Figure 3.4b). Kinetic studies were completed after 130 minutes of adding Cu^{+} (50 µM) to the probe as in Figure 3.4b.

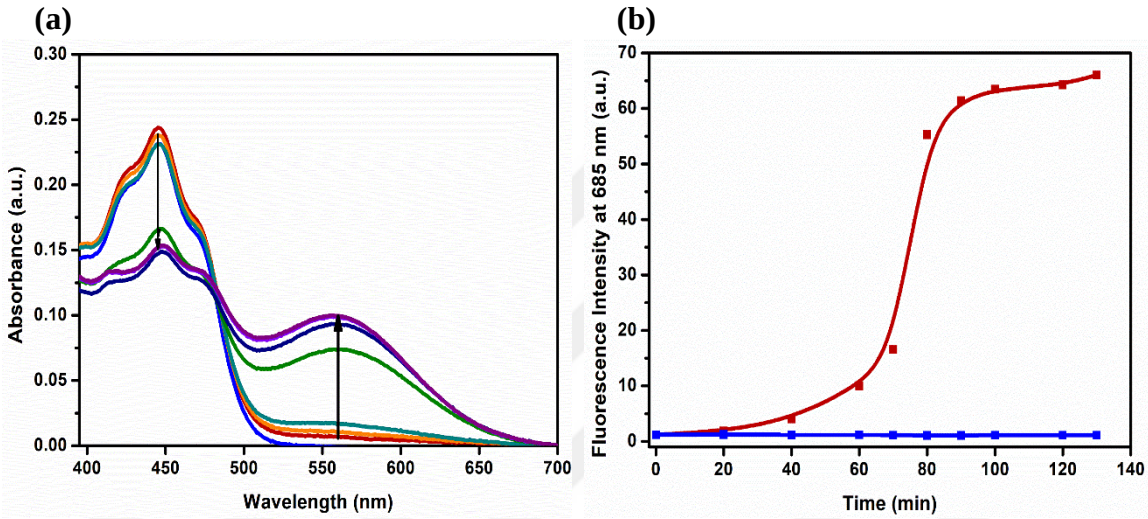

Figure 3.4 (a) Time dependent absorption spectra of **DCM-Cu** (10 µM) with addition of Cu^{+} (50 µM) in PBS-DMSO buffer solution (1:1, v/v, pH=7.4, 2 mM glutathione) from 0-130 min. (b) Time dependence of fluorescence intensity at 685 nm for **DCM-Cu** (10 µM) in PBS-DMSO buffer solution (1:1, v/v, pH=7.4, 2 mM glutathione) in the presence (red) and absence (blue) of Cu^{+}.λ_{ex} = 535 nm, λ_{em} = 540-900 nm, the slit widths were 10 nm.

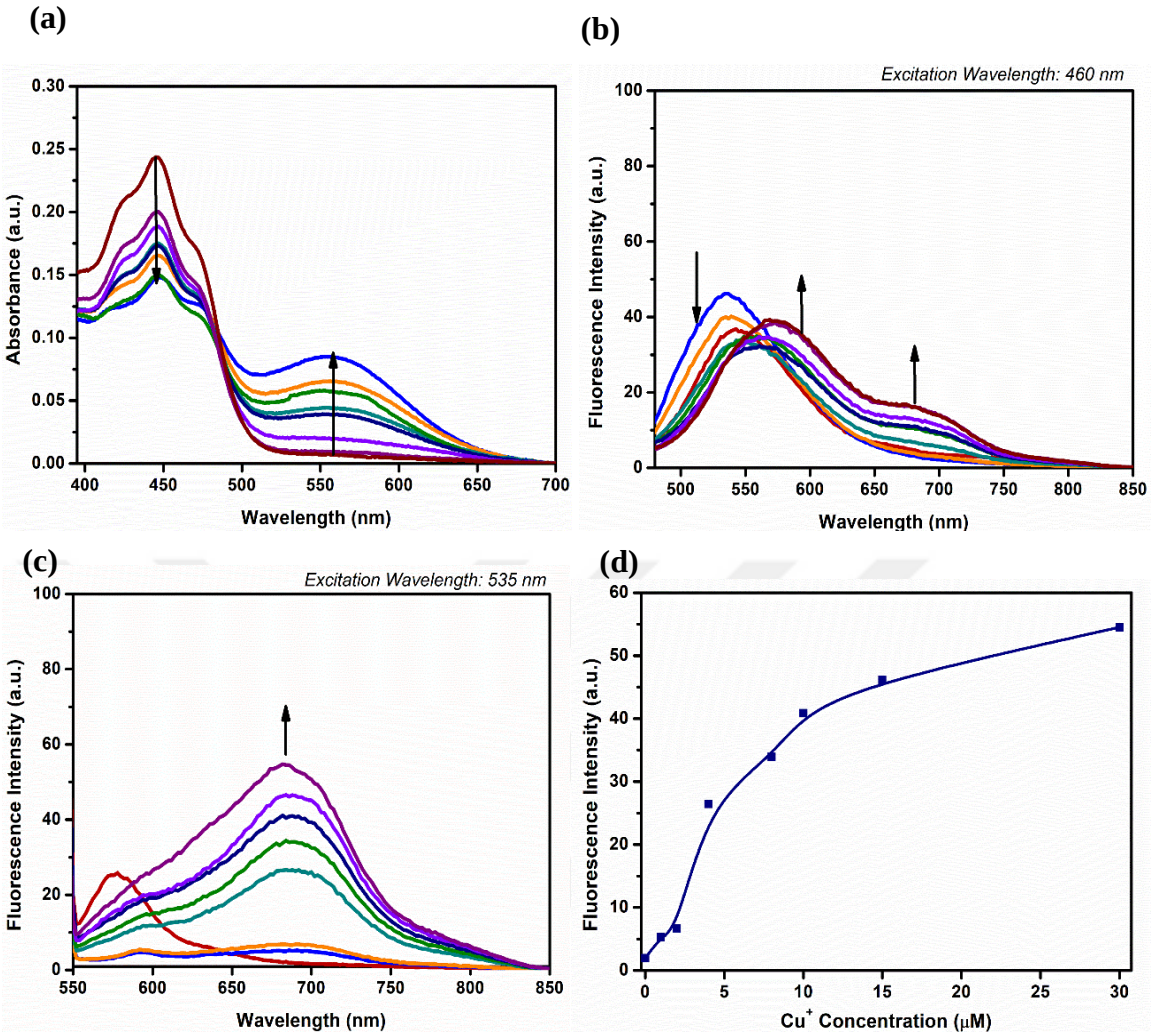

Figure 3.5 (a) Concentration dependent absorption spectra of **DCM-Cu** (10 μM) with addition of Cu^{+} (0,1,2,4,8,15,30, 50 μM) in PBS-DMSO buffer solution (1:1, v/v, 0.1 M PBS in pH=7.4, 2 mM glutathione) from 0-130 min. (b) The fluorescence spectra of **DCM-Cu** (10 μM) upon the addition of Cu^{+} (0-50 μM). λex = 460 nm and (c) λex = 535 nm, the slit widths were 5 nm. (d) Time dependence of fluorescence intensity at 685 nm for **DCM-Cu** (10 μM) in PBS-DMSO buffer solution (1:1, v/v, 0.1 M PBS in pH=7.4, 2 mM glutathione) with increasing analyte concentration.

Upon addition of increasing concentrations of Cu^{+}, the absorption band at 445 nm decreased gradually as expected, and a new absorption peak around 560 nm appeared as in the case of kinetic measurements (Figure 3.5.a). In the absence of Cu^{+}, the fluorescence signal of the probe showed no remarkable changes. Excitation of the probe at 460 nm in the presence of Cu^{+} showed increasing fluorescence signals at 560 and 685 nm, and a detectable decrease at 540 nm in good correlation with the ratiometric response. In all

experiments Cu^{+} was added in stoichiometric concentrations as follows: 1, 2, 4, 8, 15, 30 and 50 μM.

For testing fluorescence response of **DCM-Cu** in the presence of different analytes, the reactivity of **DCM-Cu** with various cations and anions were examined. Not surprisingly, in the presence of GSH and Cu^{+} both absorbance and fluorescence spectra of the probe were changed compared to other cations as both can be seen in Figure 3.6.

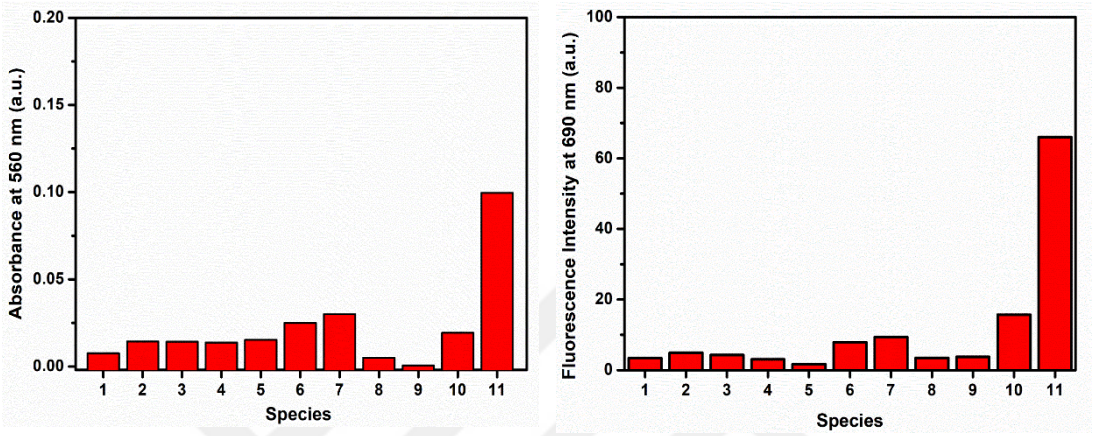

Figure 3.6 Absorbance and Flourescence responses of **DCM-Cu**(10 μM) to various species (100 μM) : (1) Ca^{2+}; (2) Mg^{2+}; (3) Zn^{2+}; (4) Mn^{2+}; (5) Ni^{2+} ; (6) Fe^{2+} ; (7) Co^{2+} ; (8) Na^{+} ; (9) K^{+} ; (10) Cu^{2+} ; (11) Cu^{+} The measurements were performed in DMSO–PBS buffer (10 mM, pH 7.4, 1 : 1, v/v) at 37 °C . Excitation 535 nm with slit width: (10, 10).

The possible reaction mechanism of **DCM-Cu** towards Cu^{+} was studied through HPLC and MS analysis. **DCM-Cu**, **DCM-Cu** after adding Cu^{+} and deprotonated solution of DCM core itself were subjected to HPLC analysis to investigate the reaction mechanism. **DCM-Cu** displayed a single peak at the retention time of 8.52 min. After addition of Cu^{+}, a new peak with retention time at 9.47 min appeared gradually in 80 minutes, which overlaps with the DCM core signal, suggesting that DCM core was clearly released in the reaction (Figure 3.7).

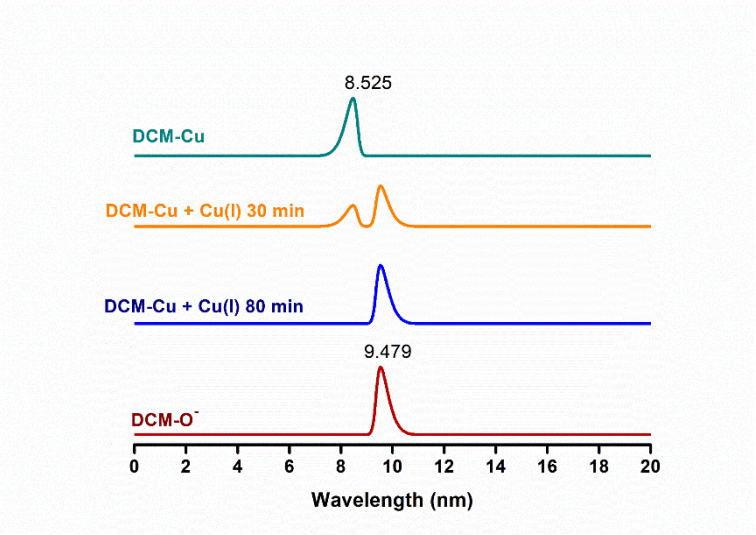

Figure 3.7 HPLC chromatograms of DCM-Cu, **DCM-Cu** reacted with Cu^{+} at different time and DCM_O.

In addition to HPLC analysis, the reaction of the **DCM-Cu** with Cu^{+} was analyzed by MS spectra. The peak at *m/z* 313.09 clearly showed the DCM core formation, whereas the peak at *m/z* 396.06 showed the formation of Cu^{2+}-TPA complex at the end of the reaction (Figure 3.8).

3.1.3 *In Vitro Experiments of DCM-Cu*

In-vitro imaging experiments of the probe were carried out with HeLa cancer cells and the induced fluorescent signals have been visualized via confocal microscopy. In this direction, a group of cells was treated with $CuCl_2$ (100 μM) for 4 hours, while another group (control) was used without addition of $CuCl_2$. As given in Figure 3.9, $CuCl_2$-treated cells exhibited a strong and time dependent red emission, suggesting that the probe can be activated in the cells and start to emit its NIR emission. Furthermore, it is worth mentioning that as the concentration of the probe increases, the signal is getting stronger. On the other side, in control cells, a very weak signal was detected even at high doses of the agent was employed, which can be attributed to endogenous Cu^{+} activity in HeLa cells. Cumulative data suggest that **DCM-Cu** can monitor changing copper fluxes in a cellular environment.

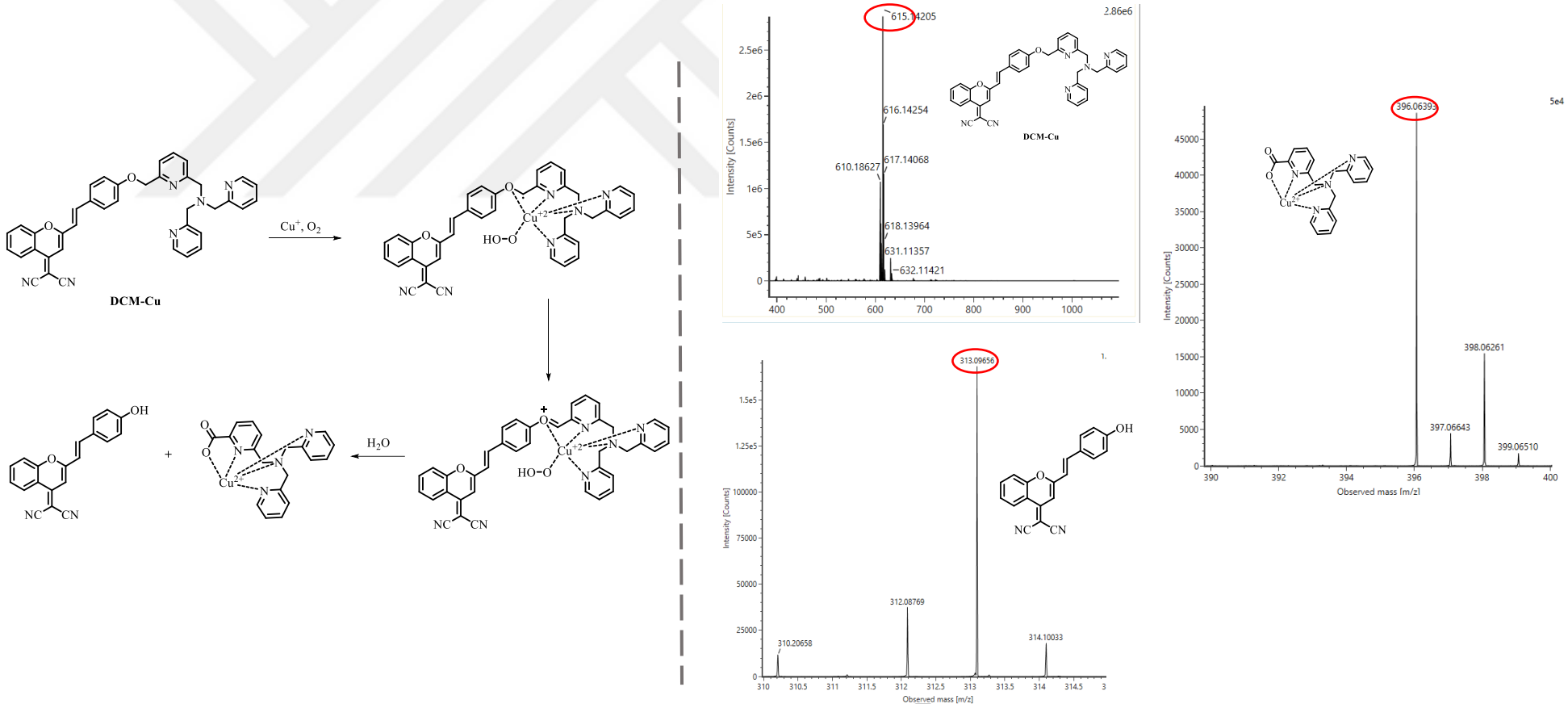

Figure 3.8 Proposed mechanism of the reaction between **DCM-Cu** and Cu^{+}

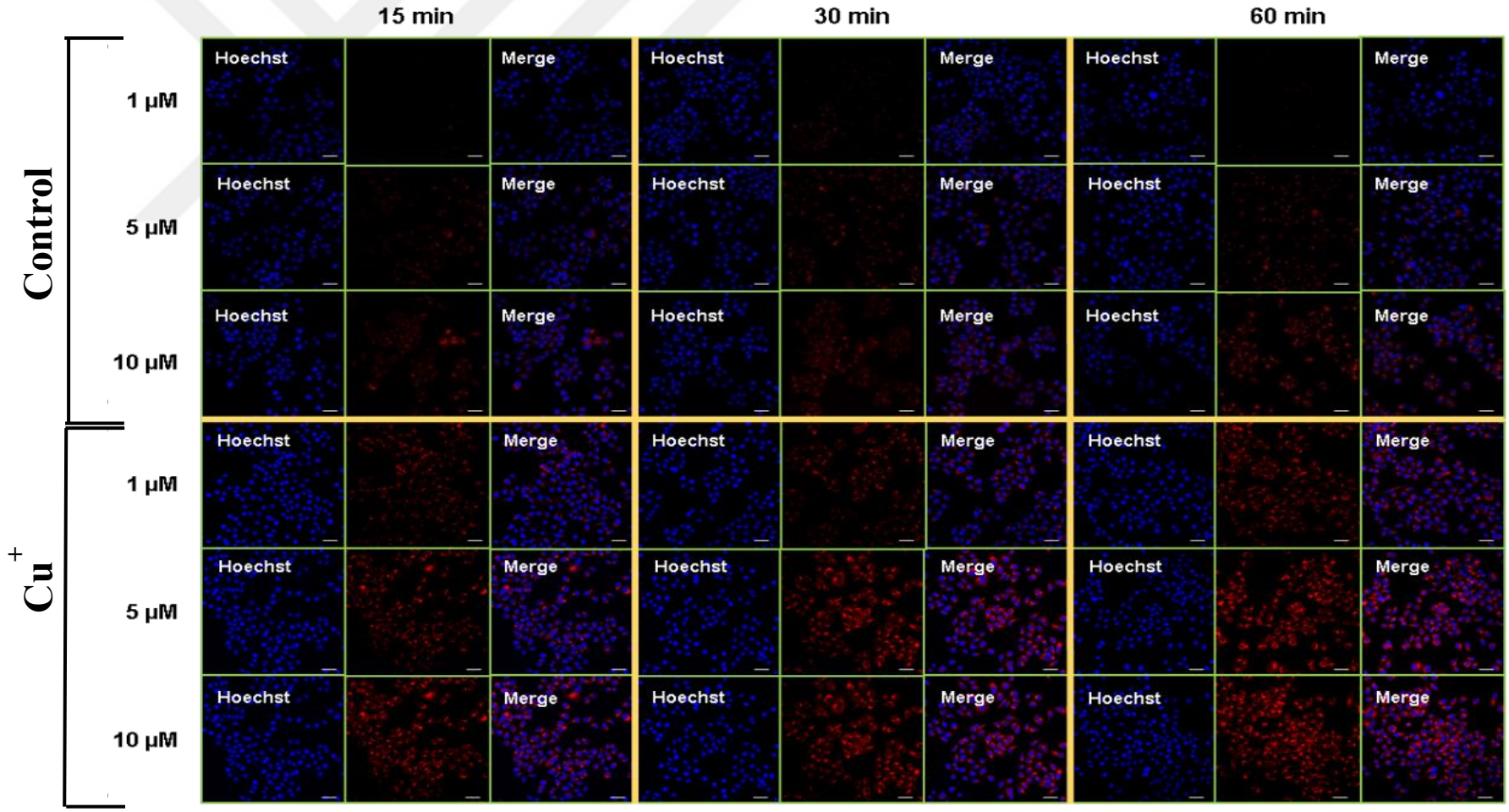

Figure 3.9 Confocal images of HeLa cells treated with either **DCM-Cu (1,5 or 10 μM)** alone or pre-treated with **$CuCl_2$ (100 μM, 4 h)**, followed by **DCM-Cu (1,5 or 10 μM)** treatment for 15, 30 and 60 min

3.2 *DCM_O-Based Activatable Photosensitizers*

3.2.1 *Synthesis of DCM_O Based Photosensitizers*

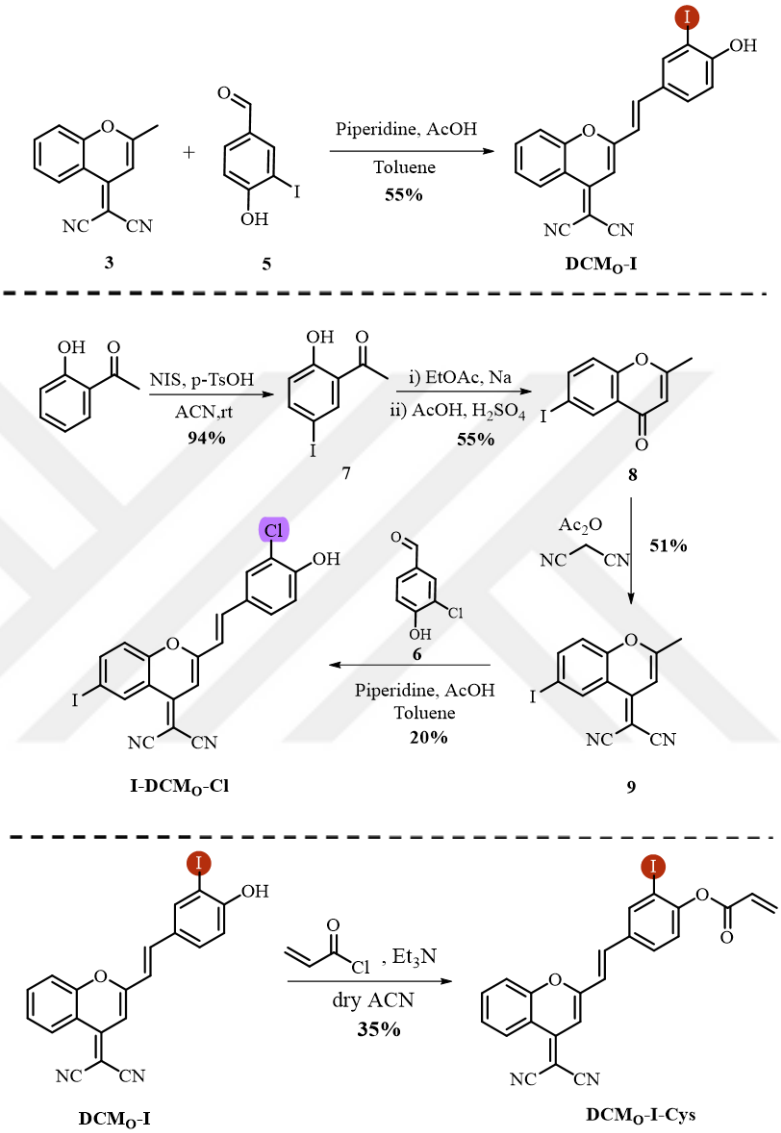

Figure 3.10 Synthetic route for **DCM_o** Based aPSs

In this study, we synthesized two different PSs to examine the PDT potential of heavy atom integrated oxygen-substituted DCM derivatives and synthesized two different PSs (Figure 3.10). The oxygen substituted DCM core (**DCM_O-I**) with an *ortho*-iodinated phenolate had the highest singlet oxygen quantum yield, and it was then converted to a cysteine (Cys) activatable PS (**DCM_O-I-Cys**) to get a cancer cell selective theranostic PS. In the design of DCM-based PSs, we focused on easily accessible oxygen-substituted DCM cores (DCM_O) and synthesized **DCM_O-I**, which has a mono-iodo substituted

phenolate unit. Iodine activates ISC and lowers the pKa of the phenol, which consequently increases the phenolate concentration at physiological medium (pH 7.4). To determine the effect of iodine position on ISC efficiency, we transferred the iodine from the phenolate ring to the DCM core (**I-DCM$_O$-Cl**) and added an *ortho* chlorine to lower the pKa of the phenolic unit, as in **DCM$_O$-I**. Figure 3.10 shows the PSs' synthetic routes. The Knoevenagel reaction between DCM core (**3**) and compound (**5**) was carried out under reflux conditions. An iodinated DCM core (**9**) was first produced for the synthesis of **I-DCM$_O$-Cl**. To this end, 2-hydroxyacetophenone was iodinated with NIS to produce compound (**7**), which was then followed by the production of chromone rings (**8**). Later, by reacting iodinated chromone and malononitrile, an iodinated DCM scaffold (**9**) was synthesized. Finally, **I-DCM$_O$-Cl** was obtained by condensation of (**9**) with compound (**6**).

3.2.2 *Photophysical Characterization of DCM$_O$ Based aPS Cores*

The photophysical characteristics of DCM$_O$-based PSs were initially tested in aqueous solutions (PBS, pH 7.4, 50% DMSO) after finishing the synthesis. The absorption peaks of heavy atom carrying oxygen substituted PSs, **DCM$_O$-I** and **I-DCM$_O$-Cl** were found as 555 nm and 560 nm, which are identical to the parent DCM core (λ_{abs} = 560 nm) that can be clearly seen in Figure 3.11.a.

Table 4 Photophysical parameters and $^1O_2$ quantum yields of DCM$_O$ derivatives.

	λ_{abs} (nm)	λ_{em} (nm)	$\varepsilon(M^{-1}cm^{-1})$	ϕ_F (%)[a]	ϕ_Δ (%)
DCM$_O$	560	705	20600	58	n.d.
DCM$_O$-I	555	728	22750	24	5.2
I-DCM$_O$-Cl	560	738	11500	6	0.6

(a) The fluorescence quantum yield measurement was carried out using Compound **12** in DCM (quantum yield was reported as 0.5958 in DCM). All tests were measured in DMSO (containing 1% PBS). For fluorescence measurement all spectra was collected with a slit width: (10/10)

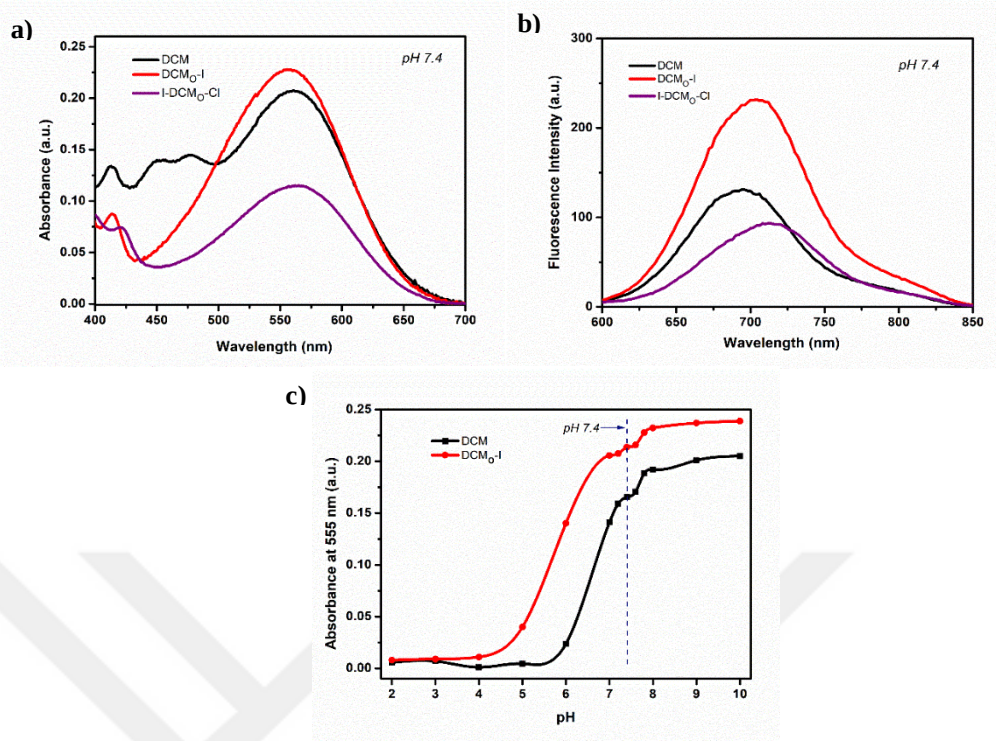

Figure 3.11 (a) Absorption and (b) fluorescence spectra of **DCM$_O$, DCM$_O$-I** and **I-DCM$_O$-Cl**. (c) pH-dependent absorption signal of **DCM$_O$-I** and **DCM$_O$** at 555 nm in aqueous solutions.

For the fluorescence measurements, **DCM$_O$-I** and **I-DCM$_O$-Cl** produced signals at 728 nm and 738 nm, respectively, which are red-shifted when compared to the DCM scaffold (Figure 3.11.b). **DCM$_O$-I** had a higher fluorescence quantum yield (Φ_F = 0.24), which was significantly lower than DCM, and that was expected since ISC and fluorescence are two competing pathways (Table 4). Both agents demonstrated comparable pH dependence in aqueous solutions buffered at different pHs (Figure 3.12 and Figure 3.13). As shown by their absorption and emission signals and they were almost completely deprotonated at physiological pH 7.4, stayed as phenolate anions, and achieved their maximum fluorescence intensities.

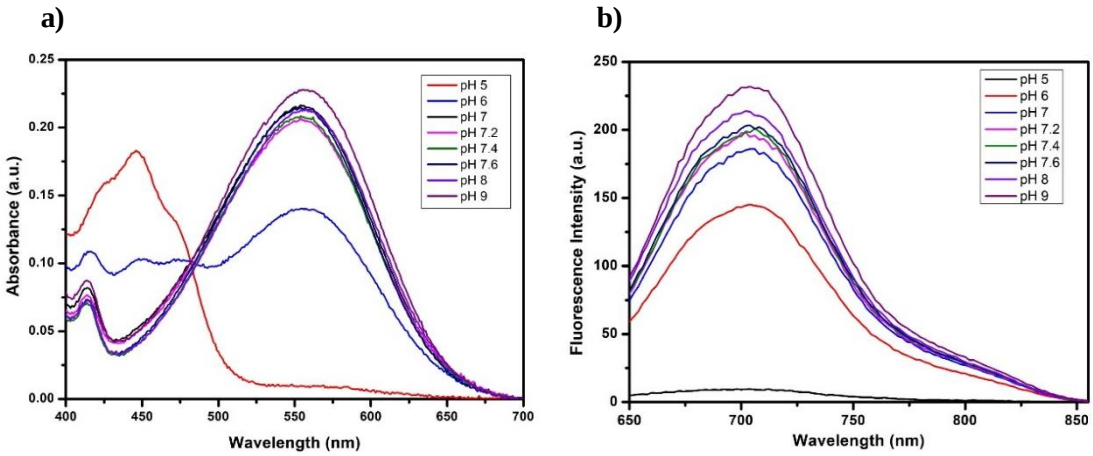

Figure 3.12 (a)Absorption and (b) fluorescence emission spectra of **DCMo-I** in aqueous solutions with different pH values.

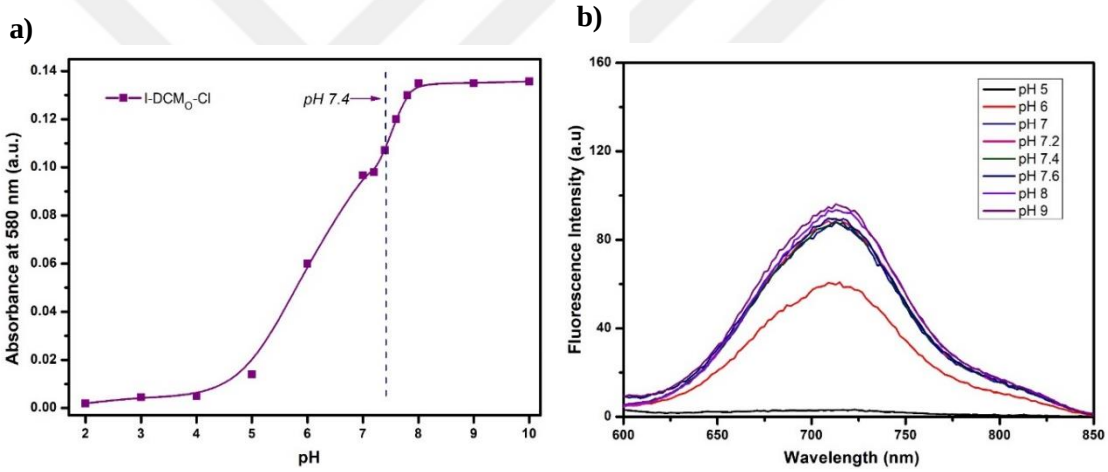

Figure 3.13 (a) Absorption and (b) fluorescence emission spectra of **I-DCMo-Cl** in aqueous solutions with different pH values.

3.2.3 *Chemical Detection of Singlet Oxygen Production of DCMo Based PS Cores*

$^1O_2$ production capabilities of DCMo-based PSs were initially studied chemically in DMSO (1% PBS, pH 7.4) solutions utilizing the well-known trap molecule 1,4-diphenylbenzofuran (DPBF). PSs were irradiated with a 630 nm LED (24.3 mW/cm^2), which resulted in a significant reduction in DPBF absorption, implying photosensitized $^1O_2$ production (Figure 3.14). The singlet oxygen quantum yields of the agents were determined using methylene blue as a standard reference.

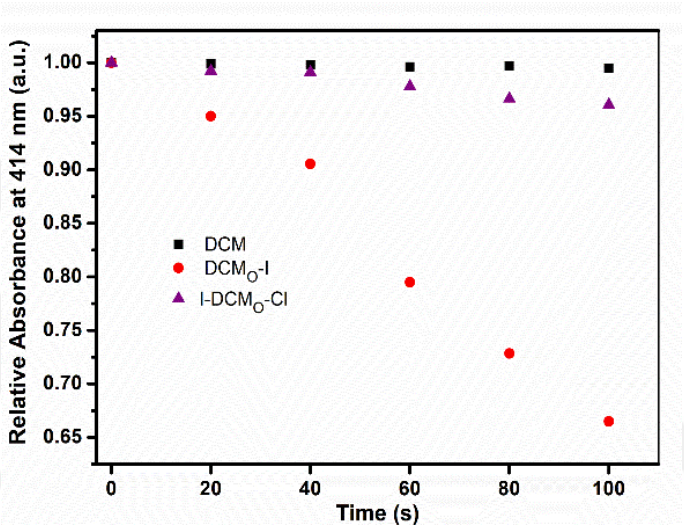

Figure 3.14 Decrease in the absorption signal of DPBF at 414 nm upon irradiating **DCM$_O$**, **DCM$_O$-I** or **I-DCM$_O$-Cl** containing DMSO (1% PBS, pH 7.4) solutions with a 630 nm LED (24.3 mW/cm^2).

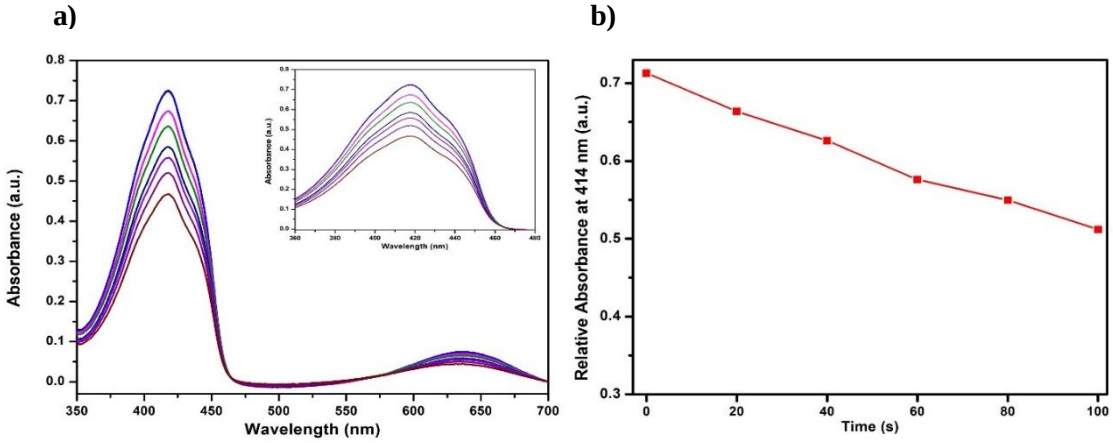

Figure 3.15 (a) Absorption spectra of DPBF upon irradiating **DCM$_O$-I** (10 μM) containing DMSO solution (1% PBS, pH 7.4) with a 630 nm LED light. (b) change in the absorption signal of DPBF at 414 nm upon irradiation with 630 nm LED light.

The **DCM$_O$-I**, which has an iodine on the phenolate ring, had the best yield (Φ_Δ= 5.2%). As shown in Figure 3.15, a gradual reduction in 414 nm, the absorption signal of DPBF, indicated the photosensitized $^1O_2$ formation.

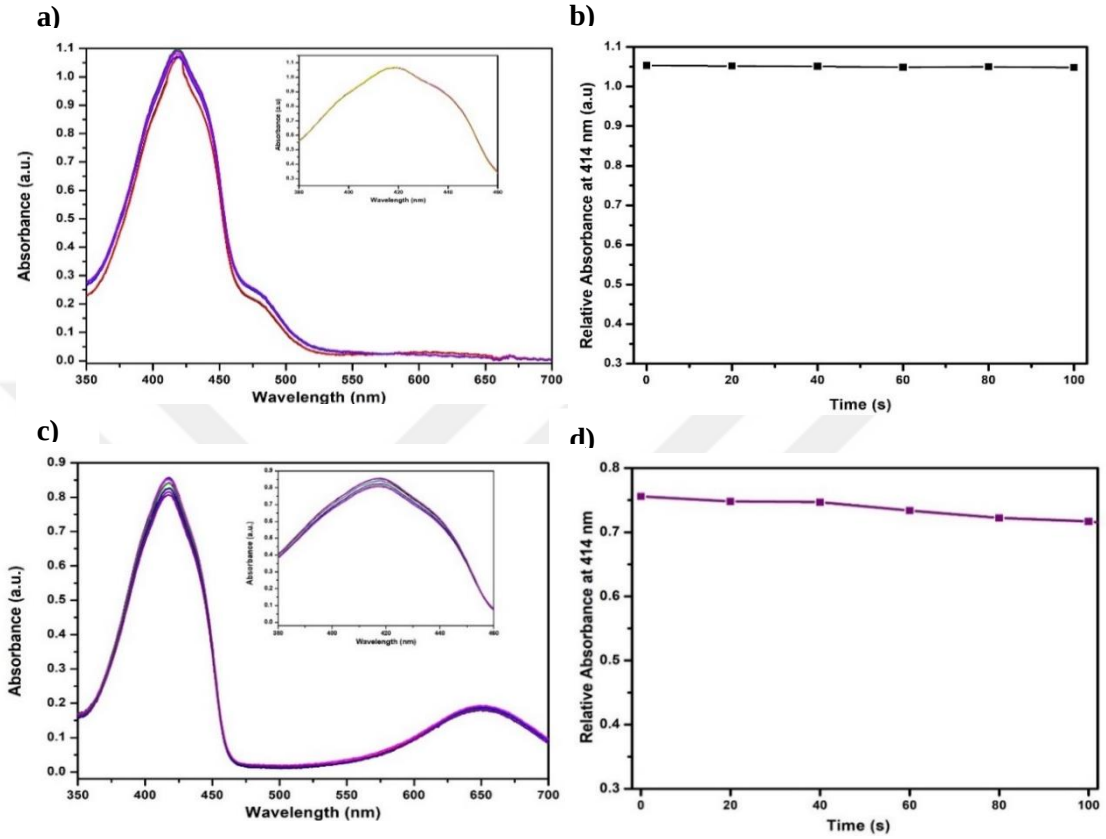

Figure 3.16 Change in the absorption spectra of (a) **DCM** and (c) **I-DCM$_O$-Cl** in DMSO solution (1% PBS, pH 7.4) containing DPBF trap molecule upon irradiation with a 630 nm LED light; (b), (d) change in the absorption signal of DPBF at 414 nm upon irradiation (b) **DCM** and (d) **I-DCM$_O$-Cl** with 630 nm.

Interestingly, when the iodine was placed on the chromone ring of the DCM core (**I-DCM$_O$-Cl**), $^1O_2$ generation yield (Φ_Δ= 0.6%) dropped dramatically, suggesting that the location of heavy atom on DCM based PSs is highly critical. DCM core itself did not show any sign of $^1O_2$ generation under 630 nm LED irradiation as expected (Figure 3.16). $^1O_2$ production of the reference, methylene blue, was further confirmed with the same conditions as applied to DCM$_O$ based PSs. (Figure 3.17)

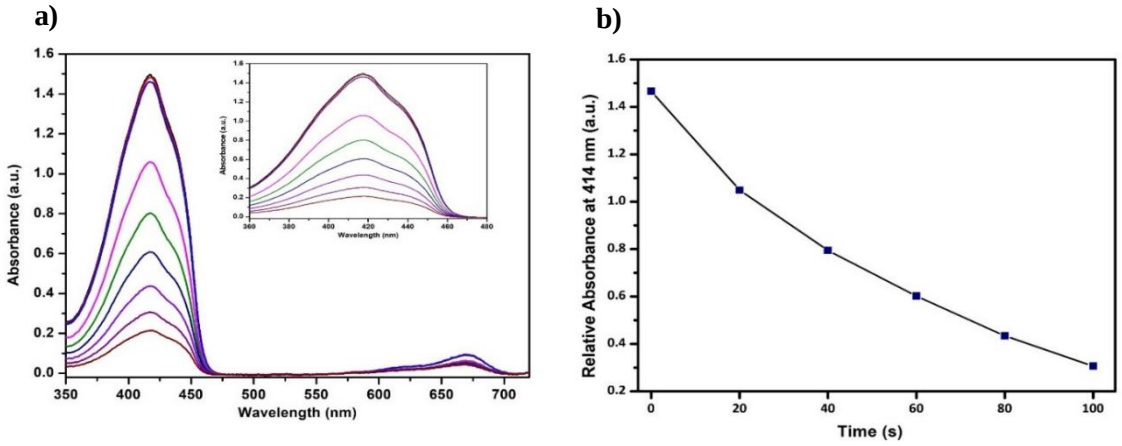

Figure 3.17 (a) Absorption spectra of DPBF upon irradiating methylene blue containing DMSO solution (1% PBS, pH 7.4) with a 630 nm LED light. (b) Change in the absorption signal of DPBF at 414 nm upon irradiation with 630 nm LED light.

3.2.4 *In vitro Experiments of DCM_O*

We focused our attention on DCM_O-I since it has the greatest $^1O_2$ quantum yield, and tested its potential in cell culture studies. The photocytotoxicity of **DCM_O-I** was first evaluated in cancerous HeLa cells using the MTT test. After 1- and 2-hours of LED light irradiation of **DCM_O-I** treated cells, a dose-dependent reduction in cell viability was observed, with a lower IC_{50} value (3.74 μM) in the case of 2 hours irradiation (Table 5). After 2 hours of treatment with a 10 μM dosage, almost total cell death was observed (Figure 3.18). When **DCM_O-I** incubated cells were held in the dark, no cell death was observed, even at high concentrations, indicating that there was no dark toxicity, which is one of the fundamental prerequisites of a successful PDT agent.

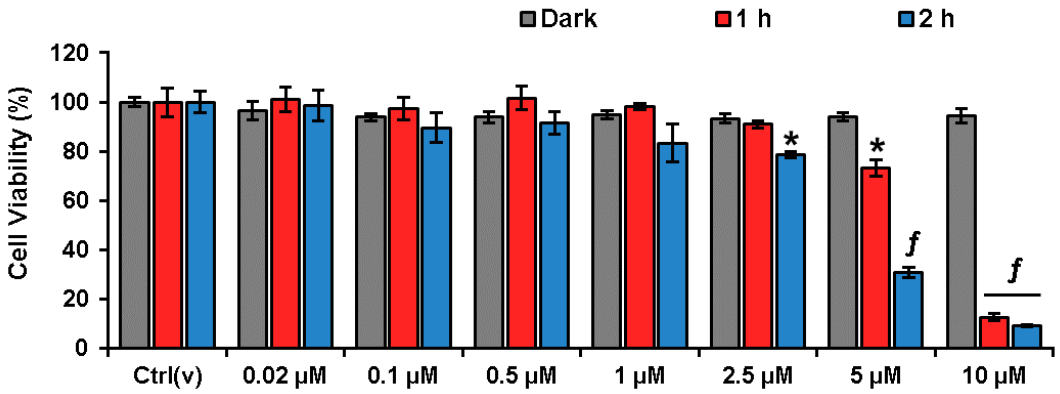

Figure 3.18 Cell viability of Hela cells treated with the increasing concentrations (0.02-10 µM) of **DCM$_O$- I** for 24 h or 1 h or 2 h at dark, followed by 2 h LED light (595 nm 9.83 mw/cm^2) illumination in fresh media and then dark incubation up to 24 h. Ctrl(v): vehicle control. Data is presented as mean ± SD. (n=6). *p<0.05, ^{f}p<0.001 *vs* Dark.

Following that, HeLa cells were treated with sodium azide (NaN_3) and *N*-acetyl cysteine (NAC), both of which are well-known $^1O_2$ quenchers and radical scavengers. Cell viability increased significantly in NaN_3-treated cells, and not in NAC-treated cells, demonstrating that $^1O_2$ is the major ROS produced during DCM$_O$-I-induced PDT activity (Figure 3.19).

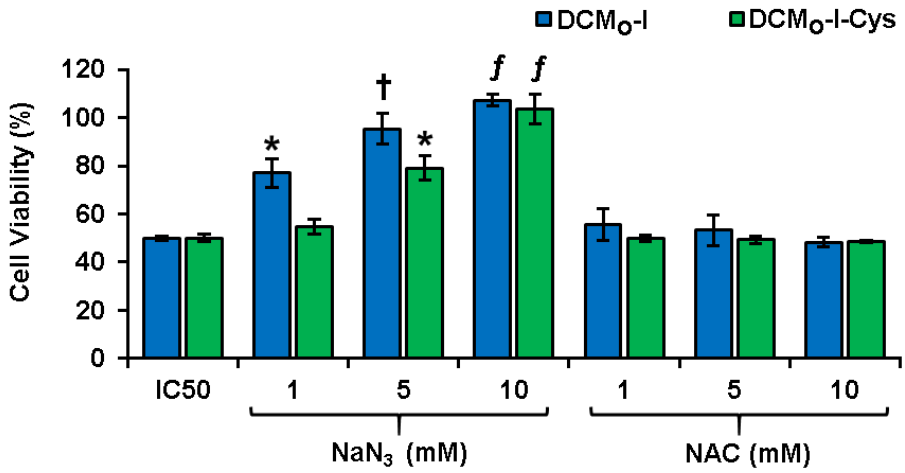

Figure 3.19 Cell viability of **HeLa** cells treated with the IC_{50} values of **DCM$_O$-I** (3.74 µM) or **DCM$_O$-I-Cys** (4.33 µM) for 2 h at dark, followed by 2 h LED light (595 nm 9.83 mw/cm^2) ilumination in the presence or absence of NaN_3 (1-10 mM) or NAC (1-5 mM) and then dark incubation up to 24 h. Ctrl(v): vehicle control, NAC: N-acetlycsyteine, NaN_3: sodium azide. (n=5-6). *p<0.05, †p<0.01, ^{f}p<0.001 vs IC_{50}.

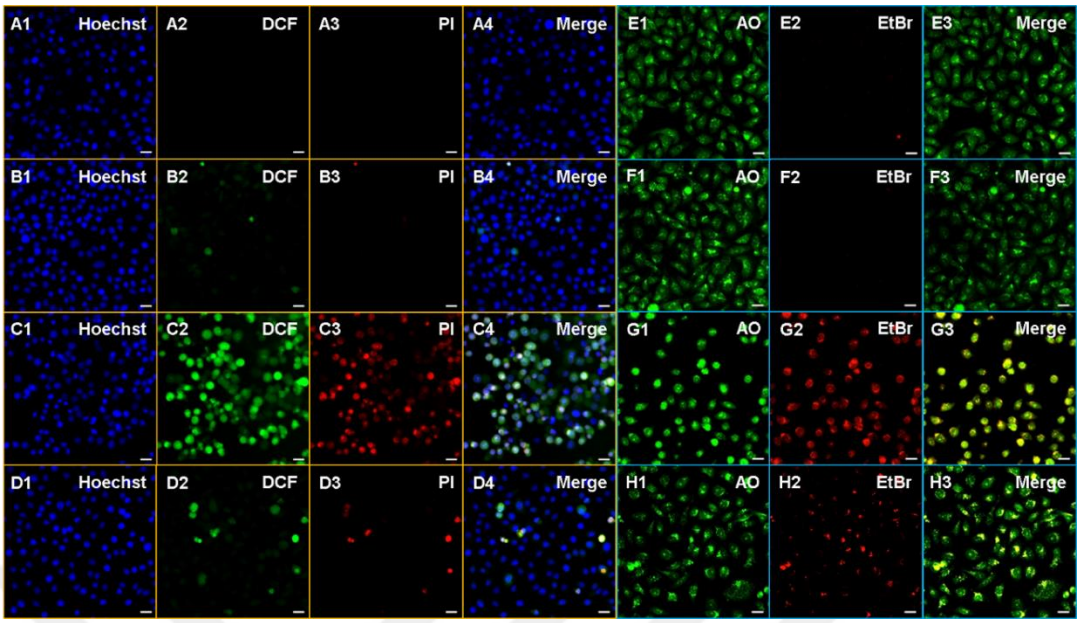

Figure 3.20 Images of triple Hoechst/DCF-DA/PI **(A-D)** and dual AO/EtBr **(E-H)** staining of **HeLa** cells treated with DMSO (0.2%) **(A1-4, E1-3)** or IC_{50} values of **DCM_O-I** for 2 h at dark **(B1-4, F1-3)**, followed by 2 h LED light (595 nm 9.83 mw/cm^2) illumination **(C1-4, G1-3)** in the presence of NaN_3 (10 mM) **(D1-4, H1-3)**. Hoechst 33342; DCF: 2′,7′-dichlorofluorescein; PI: Propium iodide; AO: Acridine orange; EtBr: Ethidium bromide. Scale bar: 50 µm.

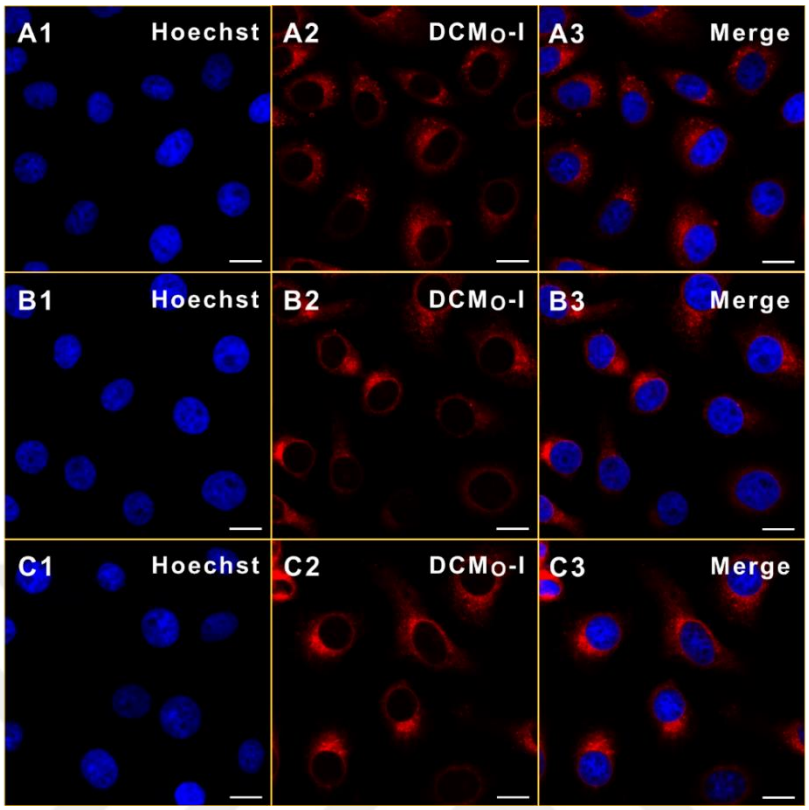

Figure 3.21 Time dependent cellular internalization of **DCM_O-I** in HeLa cells after 30 min (A1-3), 1 h (B1-3), 2 h (C1-3). Blue:Hoechst 33342; red: **DCM_O-I.** Scale bar: 10 μm.

Using a cell permeable ROS sensor 2′,7′-dichloro-fluorescein diacetate ($DCFH_2$-DA), which emits characteristic green light when oxidized to DCF by ROS, and propidium iodide (PI), which allows detection of cell death with its red fluorescence, intracellular $^1O_2$ formation and subsequent cell death were further demonstrated under confocal microscopy. After 2 hours of PDT, both green and red signals were seen in **DCM_O-I** treated HeLa cells (Figure 3.20). Because the $DCFH_2$-DA is a broad ROS sensor that is not sensitive for singlet oxygen, an inhibition experiment was carried out to demonstrate that $^1O_2$ is the primary ROS produced during the PDT action. Even when cells were exposed to light, both DCF and PI signals were significantly reduced in NaN_3-treated cells. Furthermore, no signal was seen in other control cells that were either kept dark or did not contain the PS. These findings imply that when **DCM_O-I** is exposed to light, it largely produces $^1O_2$, which causes oxidative damage and cell death. Co-staining of AO/ethidium bromide (EtBr) was used to understand better the cell death mechanism. The merging channel in **DCM_O-I** treated cells showed a reddish tint, indicating that the cells experienced predominantly early apoptosis during the PDT action. Only green

emission was seen in the control groups, showing that the cells were alive. We also wanted to see if **DCM$_O$-I** could be used for intracellular imaging and **DCM$_O$-I** (1 µM) was incubated with HeLa cells, rinsed, and confocal microscopy pictures were acquired.

3.2.5 *Intersystem Crossing in DCM$_O$-I*

To further understand the dynamics of ISC in different DCM-based PSs, we conducted computational studies. Unfortunately, we could not explain why the sulfur attachment on DCM$_S$ core resulted in lower photosensitivity than the same halogenated DCM$_O$ based one. We first determined the method of choice by performing an extensive benchmark of functionals, basis sets, and solvation. Then, we analyzed the electronic structure of DCM$_O$-I with a particular interest on the mechanism underlying the intersystem crossing phenomenon that populates the triplet states of the dye. Our results were summarized in Figure 3.22. We found that only one triplet state, T5, is significantly coupled to S1 with a total magnitude of the spin orbit coupling of 175 cm^{-1}. The difference in energy between S1 and T5 in the geometry of S0 is, however, substantial (0.94 eV). T4 is found slightly lower than T5 and also couples with S1, yet with a significantly lower coupling constant of 26 cm^{-1}. The spin orbit coupling between S1 and T5 calculated for DCM$_O$-I (i.e, 175 cm^{-1}) is therefore likely to induce intersystem crossing, yet the high and positive energy gap between the states is prohibitive.

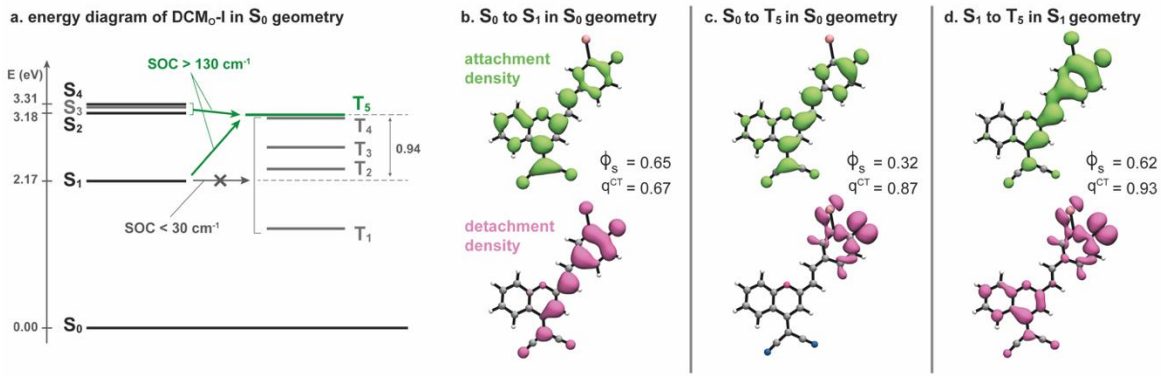

Figure 3.22 Energy diagram and excited states topology for DCM$_o$-I at the B3LYP/aug-cc-pVDZ/cc-pVTZ-DK(iodine)/CPCM(DMSO) level. a) Energy diagram in the minimum geometry of S0. S1, S2, and S4 are coupled with T5 with a magnitude of spin orbit coupling of 175, 136, and 208 cm^{-1}, respectively. b) detachment and attachment electron densities involved in the transition from S0 to S1 in the geometry of S0. c) same as b showing the effective electron density reorganization to reach T5 from S0 (via any

intermediate singlet state). d) same as b showing the electron density reorganization upon transition from S1 to T5, in the geometry of S1. All surfaces are plotted with an isodensity value of 0.001. Detachment/attachment densities overlap integral (ϕ_s) and magnitude of the net transferred charge upon electron density reorganization (q^{CT}) are given for each transition.

Relaxing the structure to the geometry of S1 yields a similar picture with a spin orbit coupling of 184 cm^{-1} and an energy gap of 1.07 eV. A comparison of the electron density between different states of DCM_O-I was represented in Figure 3.22 b-d with detachment/attachment electron densities and related descriptors as calculated with a locally modified version of the Mesra software. In brief, the detachment density corresponds to the portion of electron density that is displaced from the initial state upon a given transition, and the attachment density indicates were this portion of density relocates in the target excited state. The ϕ_S descriptor corresponds to the overlap between detachment and attachment densities, ranging from 0 to 1, transcribing the charge transfer character of the reorganization of electron density (i.e, the lower the value of ϕ_S, the greater the charger transfer). The q^{CT} descriptor quantifies the net charge being effectively transferred upon electronic structure reorganization. The transition from S0 to S1 upon absorption has a $\pi \rightarrow \pi^*$ character and shows little charge transfer Figure 3.22b). Comparing the electron densities in the S0 and T5 states (Figure 3.22c) indicates that reaching T5 *via* S1 (or any other singlet sate) would result in a significant effective charge transfer and an overall $n \rightarrow \pi^*$ transition involving the lone pair on the phenolate moiety of the molecules as departing density (detachment). It is noteworthy that this departing density is in close proximity to the heavy Iodine atom in DCM_O-I. The actual transition from S1 to T5 was depicted in Figure 3.22d, where the electronic structure was calculated in the geometry of S1.

The departing density in the transition involved mainly the lone pair of the phenolate moiety, and marginally other parts of the molecules. The rather large overlap between detachment and attachment densities of the S1 to T5 transition ($\phi_S = 0.62$) indicates that the significant, effective charge relocation between S0 and T5 ($\phi_S = 0.32$) is sequential, with parts resulting from the S0 to S1 transition and the rest occurring upon intersystem crossing from S1 to T5.

3.2.6 *Synthesis of DCM$_O$-I-Cys:*

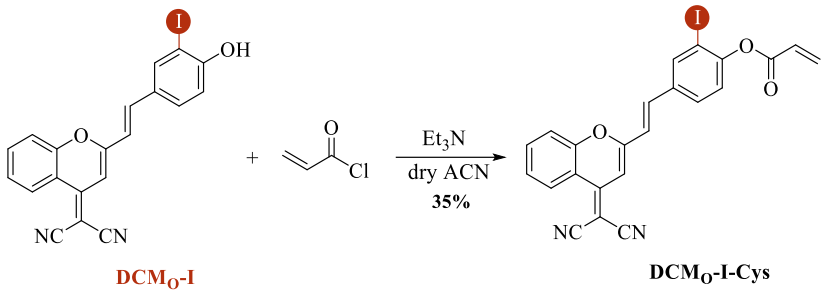

Figure 3.23 Synthesis of **DCM$_O$-I-Cys**

We aimed to turn **DCM$_O$-I** into a cancer cell selective activity-based PS (aPS) after demonstrating that it is a potential theranostic core (Figure 3.23). As a result, it can only be triggered in cancer cells, reducing the risk of harmful side effects in healthy cells. In this regard, we used a cysteine (Cys) sensitive acrylate moiety as a masking unit to cage the phenolic group, as in DCM-based imaging probes, and produced the first example of a Cys activatable DCM-based PS (**DCM$_O$-I-Cys**). Cys is an intracellular antioxidant that is overexpressed in most cancer cells in order to minimize oxidative damage. As a result, it has been widely regarded as a tumor marker, and it has been employed in a variety of activity-based fluorescence sensor designs. Cys-responsive therapeutic compounds, on the other hand, have remained elusive. Our group recently published our findings on Cys activated hemicyanine-based PS, which is the first example of a Cys-responsive phototherapy agent. Because of the constrained intramolecular charge transfer (ICT) mechanism, both $^1O_2$ production and fluorescence of **DCM$_O$-I-Cys** are suppressed in the caged form. Michael addition of Cys to acrylate and following intramolecular cyclization cleaves the cage unit and releases the active phototheranostic agent **DCM$_O$-I**. By treating **DCM$_O$-I** with an acryloyl chloride, the synthesis of **DCM$_O$-I-Cys** was accomplished in one step.

3.2.7 *Chemical Detection of Singlet Oxygen Production of DCMo-I-Cys*

Using DPBF as a trap molecule in DMSO, the $^1O_2$ production capability of **DCMo-I-Cys** was also assessed (1% PBS, pH 7.4). No trace of $^1O_2$ formation was found when **DCMo-I-Cys** was irradiated with a 630 nm LED (24.3 mW/cm^2), as demonstrated by the steady absorption signal of the DPBF (Figure 3.24).

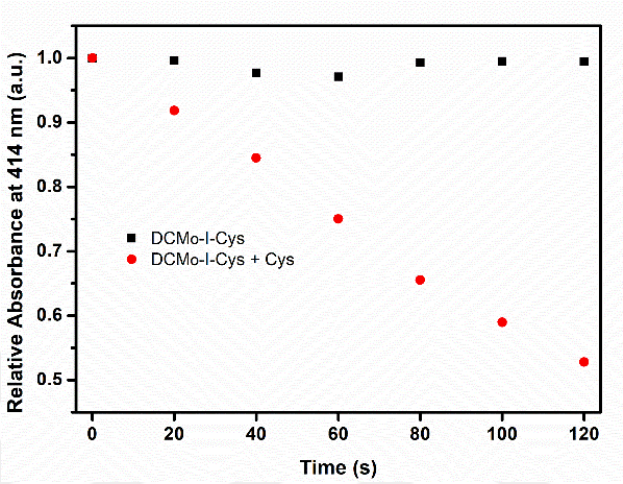

Figure 3.24 Relative $^1O_2$ generation efficiency of **DCMo-I-Cys** (10 μM) prior to and after addition of Cys (100 μM) by using DPBF as a $^1O_2$ trap molecule. In the case of fluorescence measurements excitation wavelength and slid withs were adjusted to 555 nm and 10/10 respectively.

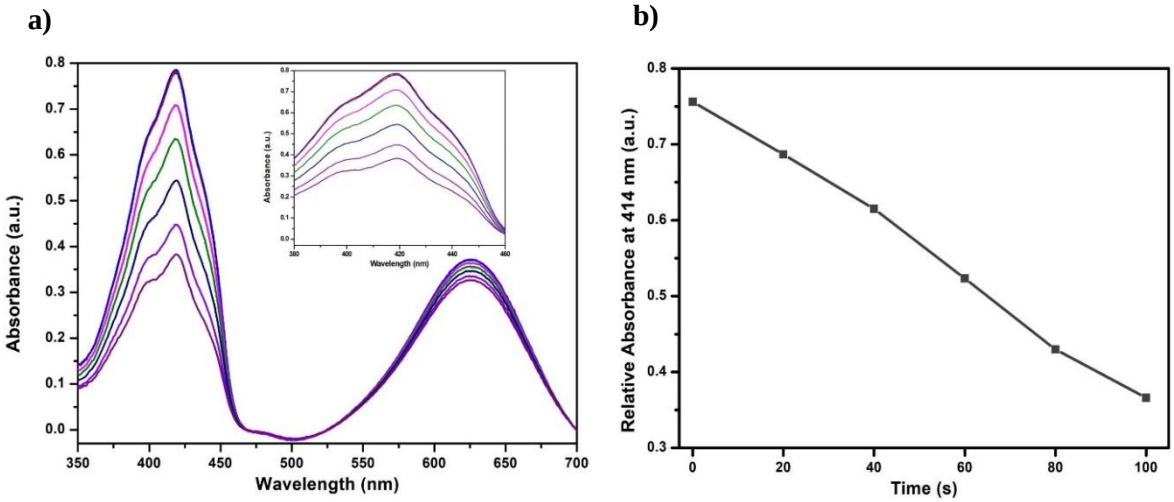

Figure 3.25 (a) Absorption spectra of DPBF upon irradiating **DCMo-I-Cys + Cys** containing DMSO solution (1% PBS, pH 7.4) with a 630 nm LED light. (b) change in the absorption signal of DPBF at 414 nm upon irradiation with 630 nm LED light.

A steady reduction in trap absorption was seen with the addition of Cys (100 µM) (Figure 3.25), demonstrating the creation of an active **DCM$_O$-I** core in the presence of Cys and the generation of photosensitized $^1O_2$. Whereas, in the caged form, no reduction in the trap absorption was observed that can be seen in Figure 3.26.

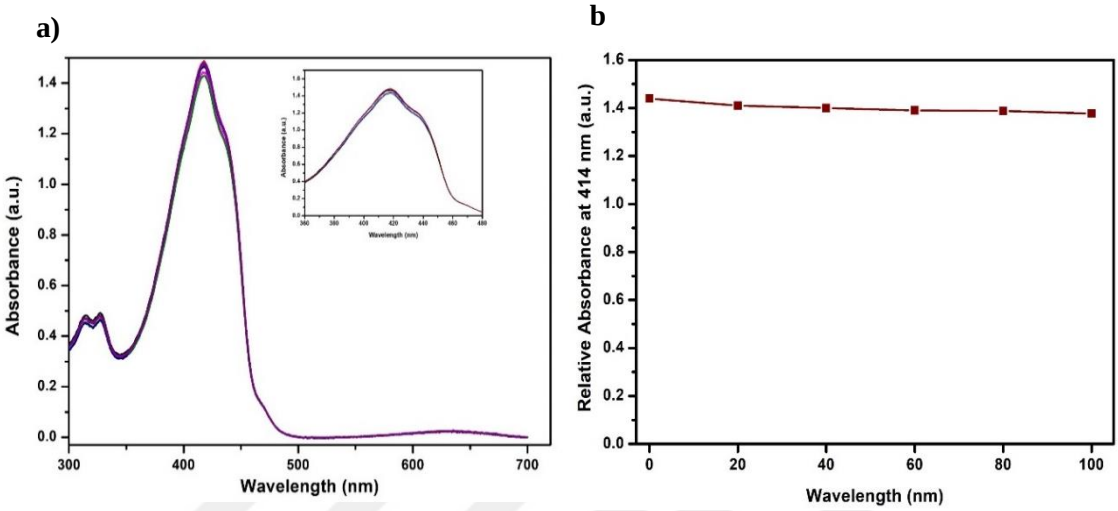

Figure 3.25 (a) Absorption spectra of DPBF upon irradiating **DCM$_O$-I-Cys** containing DMSO solution (1% PBS, pH 7.4) with a 630 nm LED light. (b) change in the absorption signal of DPBF at 414 nm upon irradiation with 630 nm LED light.

3.2.8 *Photophysical Characterization of DCM$_O$-I-Cys:*

In PBS-DMSO buffer solution (1:1, v/v, pH=7.4), **DCM$_O$-I-Cys** showed a blue shifted absorption signal centered at 395 nm. When **DCM$_O$-I-Cys** was exposed to increasing concentrations of Cys (0-100 µM), a prominent absorption peak at 555 nm emerged quickly (approximately in 1 min.) and belonged to the active core of **DCM$_O$-I**. (Figure 3.26, Figure 3.28). When 100 µM Cys was added on to the Ps in fluorescence experiments, a very quick turn-on response was recorded at 705 nm following addition of Cys (λ_{ex} = 555 nm), which had a 14-fold increase in emission intensity with a substantial Stokes shift (150 nm).

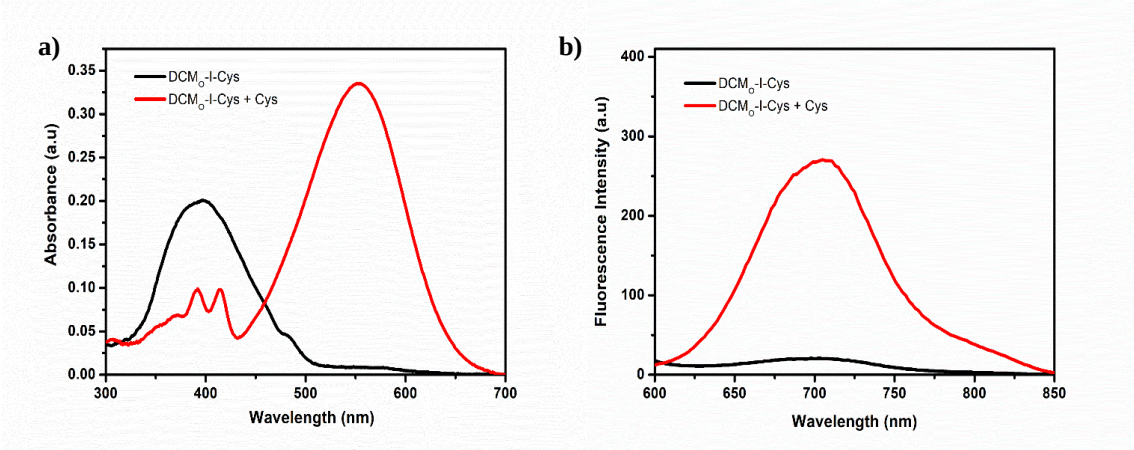

Figure 3.27 (a) Absorption and (b) Fluorescence emission spectra of **DCM$_O$-I-Cys** (10 μM) with addition of Cys (100 μM) in PBS-DMSO buffer solution (1:1, v/v, 0.1 M PBS in pH=7.4) at 37 °C.

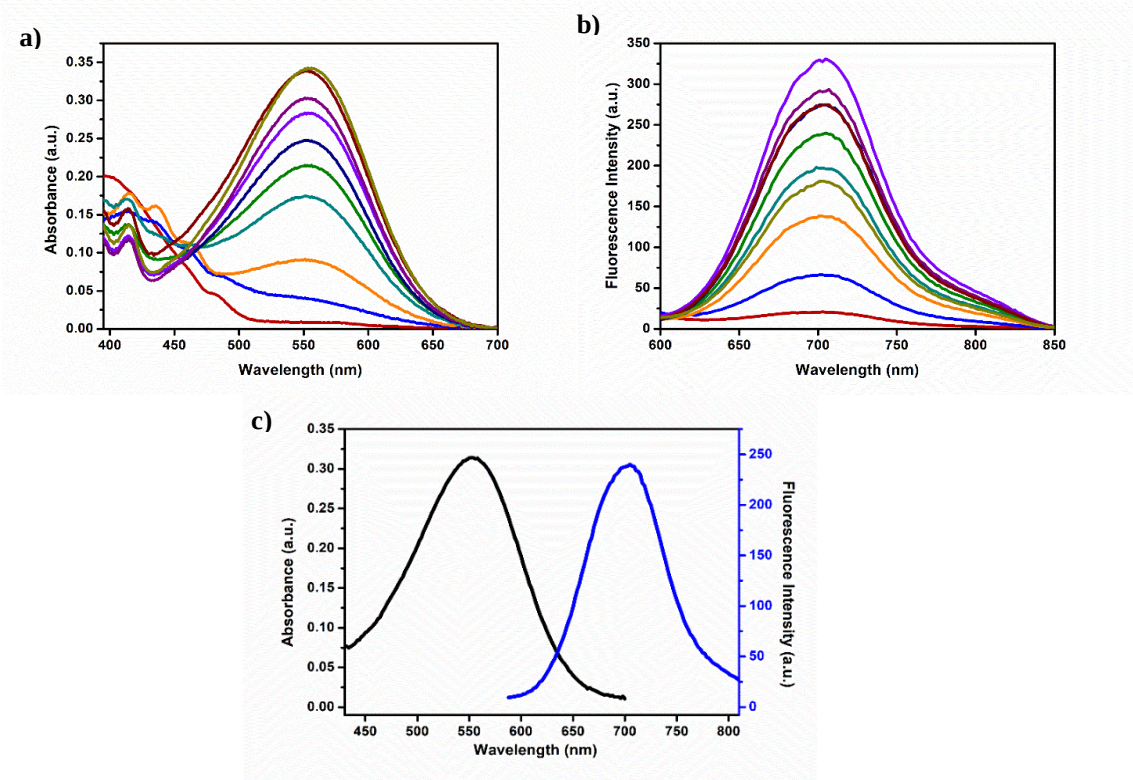

Figure 3.28 a) Absorbance and (b) fluorescence spectra of **DCM$_O$-I-Cys** (10 μM) upon addition of different concentrations of Cys (from 0.5 to 140 μM) in PBS buffer (50% DMSO, pH 7.4) at 37˚C. (c) Stokes shift of **DCM$_O$-I-Cys** in the presence of Cys (100 μM).

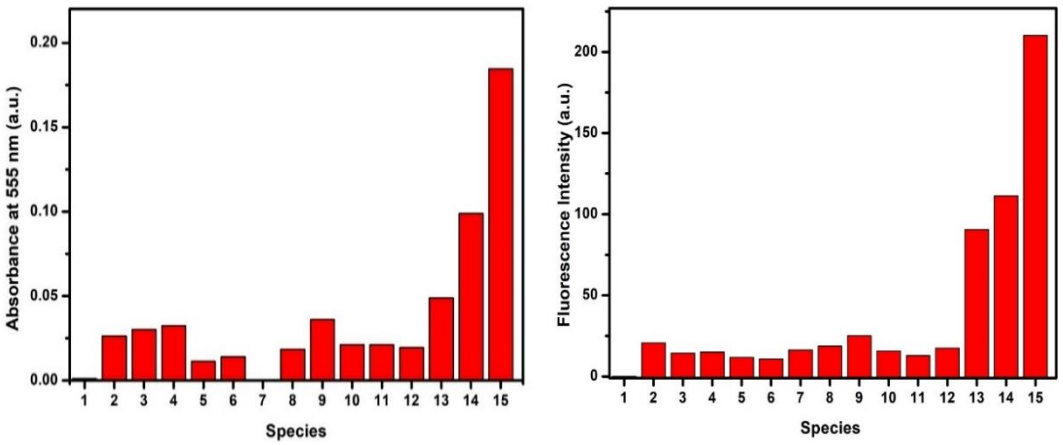

Figure 3.28 Absorbance and Fluorescence responses of **DCM$_O$-I-Cys** (10 μM) to various species (100 μM) : (1) blank; (2) Glu; (3) Ala; (4) NO_2^-; (5) HCO_3^- ; (6) CO_3^{-2} ; (7) OAc^- ; (8) SO_4^{-2} ; (9) SO_3^- ; (10) $S_2O_3^-$; (11) SCN^-; (12) NaHS; (13) GSH; (14) HCy ; (15) Cys; The measurements were performed in DMSO–PBS buffer (10 mM, pH 7.4, 1 : 1, v/v) at 37˚C at 37 °C. Excitation 555 nm with slit width: (10, 10).

Next, the selectivity of **DCM$_O$-I-Cys** by treating it with biothiols and other potentially competing analytes were tested (Figure 3.29). To investigate the selectivity, **DCM$_O$-I-Cys** was treated with various analytes including various anions (NO_2^-, HCO_3^-, CO_3^-,OAc^- ,SO_4^{2-}, SO_3^{2-}, $S_2O_3^-$, SCN^-, sodium salts were used for anions), amino acids (Glu, Ala,) and biothiols (Cys, Hcy, GSH). Most of these analytes are widespread in cells. As shown Figure 3.28, aexcept for NaHS, sligthly fluorescence signals can observed upon addition of other biothiols. This shows that, **DCM$_O$-I-Cys** showed a clear selectivity preference for Cys as evidenced from both absorption and fluorescence spectra.

The reaction of Cys with **DCM$_O$-I-Cys** involves two major steps (Figure 3.29). Michael addition reaction of the thiol to the acryloyl group of **DCM$_O$-I-Cys** is the first one, and then it is followed by a spontaneous intramolecular cyclization to release the NIR fluorescent compound **DCM$_O$-I**.

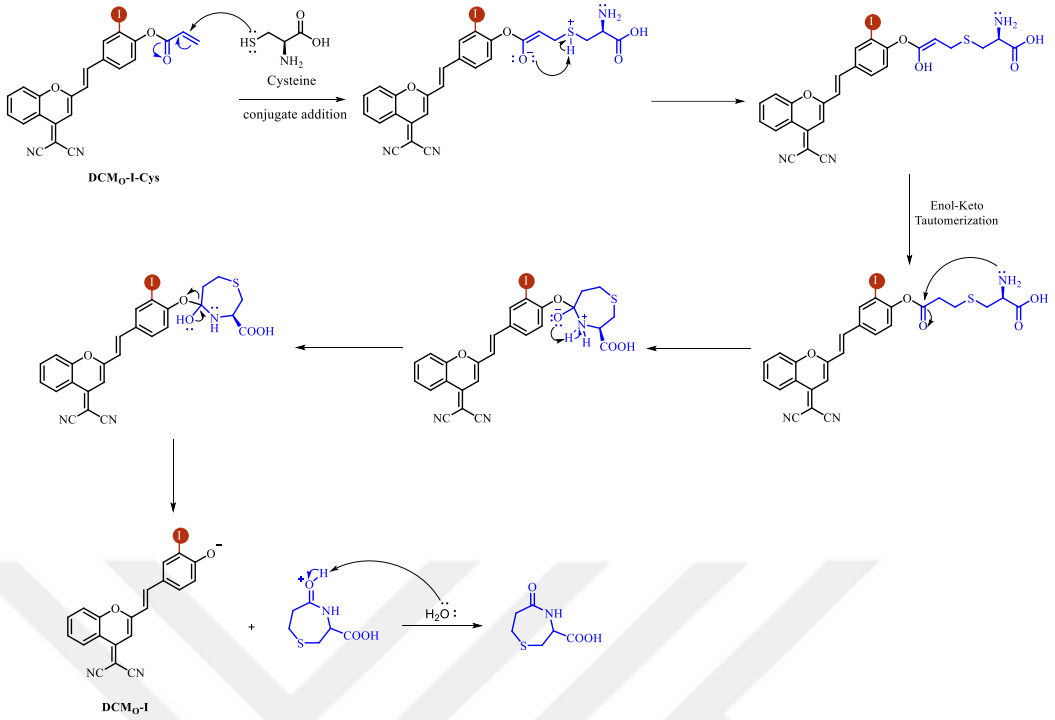

Figure 3.30 Activation mechanism of **DCM$_O$-I-Cys** in the presence of cysteine.

The reaction between **DCM$_O$-I-Cys** and Cys was monitored using HPLC. To determine the probe's reaction, **DCM$_O$-I-Cys**, **DCM$_O$-I-Cys** containing Cys at different concentrations, and DCM$_O$-I were injected to HPLC individually. Treating **DCM$_O$-I-Cys** with a Cys (100 µM) resulted a signal that was eluted at the same minute with the parent DCM$_O$-I core, indicating DCM$_O$-I was released upon activation process. At the retention time of 9.54 min, **DCM$_O$-I-Cys** showed a single peak. After addition of Cys, a new single peak with a retention duration of 8.72 min progressively developed (Figure 3.31).

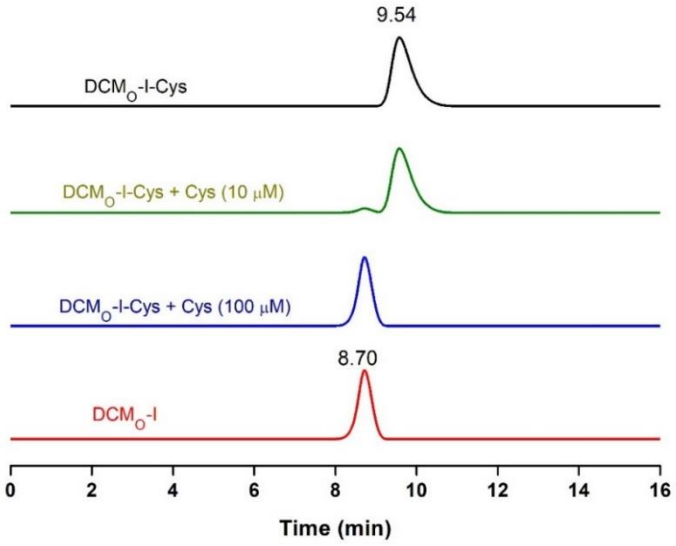

Figure 3.31 HPLC chromatograms of **DCM$_O$-I-Cys, DCM$_O$-I-Cys** reacted with Cys at different concentrations and **DCM$_O$-I**

3.2.9 *In vitro Experiments of DCM$_O$-I-Cys*

To study **DCM$_O$-I-Cys** selectivity, we investigated its cytotoxicity in malignant HeLa cells with high Cys levels and normal L929 cells. In the whole concentration range (0-10 μM), **DCM$_O$-I-Cys** showed no dark toxicity. After 1h and 2h of light (595 nm, 9.83 mw/cm^2) irradiation, **DCM$_O$-I-Cys** treated HeLa cells died in a dose-dependent manner. At a 10 μM dosage, cell viability reduced to 15%, and the IC_{50} for 2h excitation was determined to be 4.33 μM. In the case of 1 h irradiation, the IC_{50} was computed as 6.11 μM, which is slightly higher as expected (Figure 3.31, Table 5).

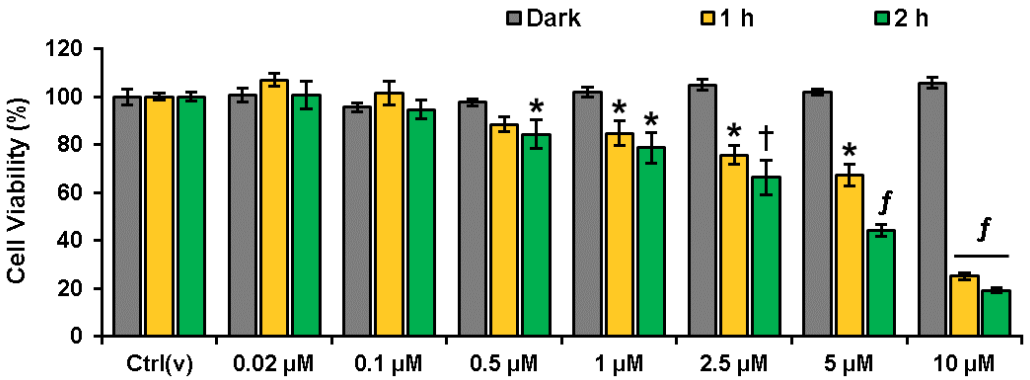

Figure 3.32 Cell viability of Hela cells treated with the increasing concentrations (0.02-10 µM) of **DCM$_O$-I-Cys** for 24 h or 1 h or 2 h at dark, followed by 2 h LED light (595 nm 9.83 mw/cm^2) ilumination in fresh media and then dark incubation up to 24 h. Ctrl(v): vehicle control. Data is presented as mean ± SD. (n=6). *p<0.05, †p<0.01, ^{f}p<0.001 vs Dark.

When normal L929 cells were subjected to the same experiment under same circumstances, cell mortality was dramatically reduced, and cell viability remained about 80% even at the maximum dose (10 µM) (IC_{50} > 10 µM) (Figure 3.32). Cell viability reduced to 40% when L929 cells were treated with "always on" **DCM$_O$-I** (10 µM) because it was unable to distinguish between normal and malignant cells (Figure 3.33). NaN_3 treatment boosted cell survival in HeLa cells in a concentration-dependent manner, but NAC inhibition had no impact, as in the case of **DCM$_O$-I** core.

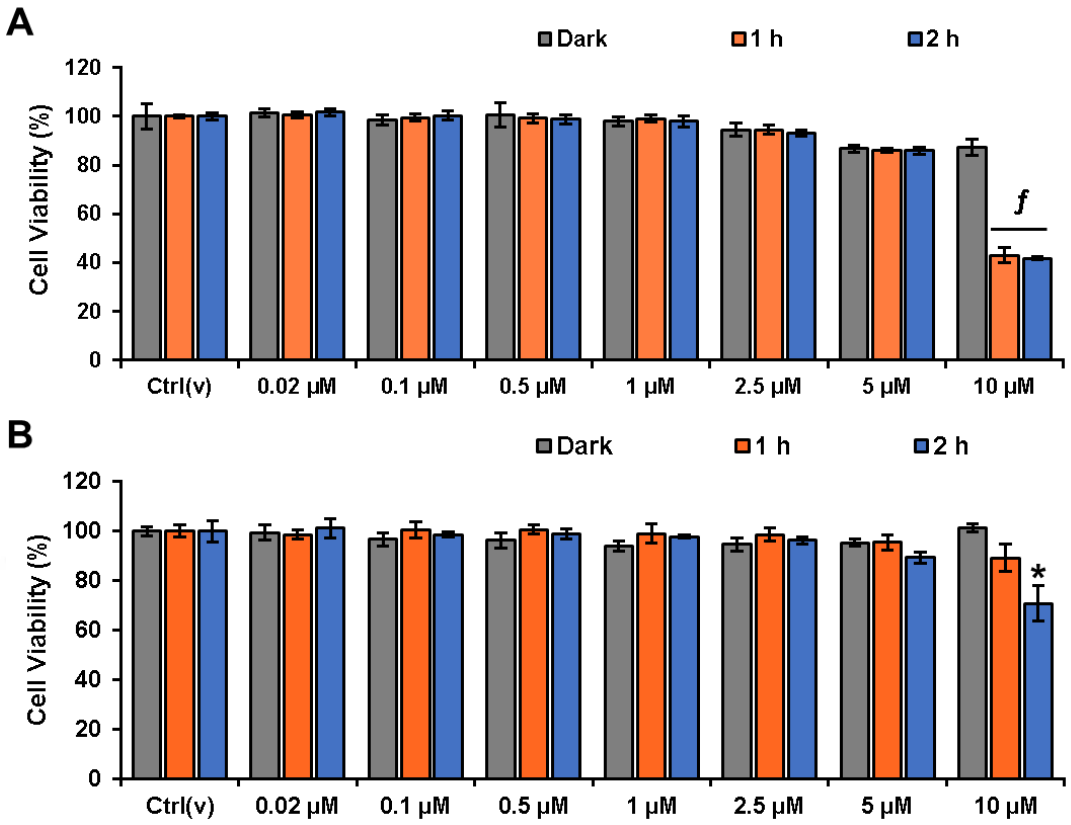

Figure 3.33 Cell viability of **L929** cells treated with the increasing concentrations (0.02-10 µM) of **DCM$_O$- I (A)** and **DCM$_O$-I-Cys (B)** for 24 h or 1 h or 2 h at dark, followed by 2 h LED light (595 nm 9.83 mw/cm^2) illumination in fresh media and then dark incubation up to 24 h. Ctrl(v): vehicle control. Data is presented as mean ± SD. (n=6). *p<0.05, ^{f}p<0.001 vs Dark.

Table 5 IC$_{50}$ values of DCM$_O$-I and DCM$_O$-I-Cys in HeLa and L929 cells

HeLa	DCM$_O$-I.	DCM$_O$-I-Cys	**L929**	DCM$_O$-I.	DCM$_O$-I-Cys
2 h	3.74 µM	4.33 µM	2 h	8.96 µM	10 µM <
1 h	6.32 µM	6.11 µM	1 h	9. 10 µM	10 µM <

The DCM$_O$-I-Cys generated ROS production in HeLa cells was also measured using the DCFH$_2$-DA sensor, with green emission found only when the DCM$_O$-I-Cys treated cells were irradiated (Figure 3.32). Cell death was also exclusively found in the same group of HeLa cells. After PDT action, PI staining and AO/EtBr imaging revealed that primarily late apoptotic/necrotic cells persist (Figure 3.34). NaN_3 inhibition lowered $^1O_2$ production significantly, and the alive cell ratio looked to be greater, similar to DCM$_O$-I core. Control cells that were either not treated with DCM$_O$-I-Cys or maintained in the

dark did not produce ROS or demonstrate cytotoxicity, as predicted (Figure 3.34). The findings show that endogenous Cys activates DCM_O-I-Cys, which then causes $^1O_2$-induced selective photocytotoxicity in cancer cells with high Cys activity.

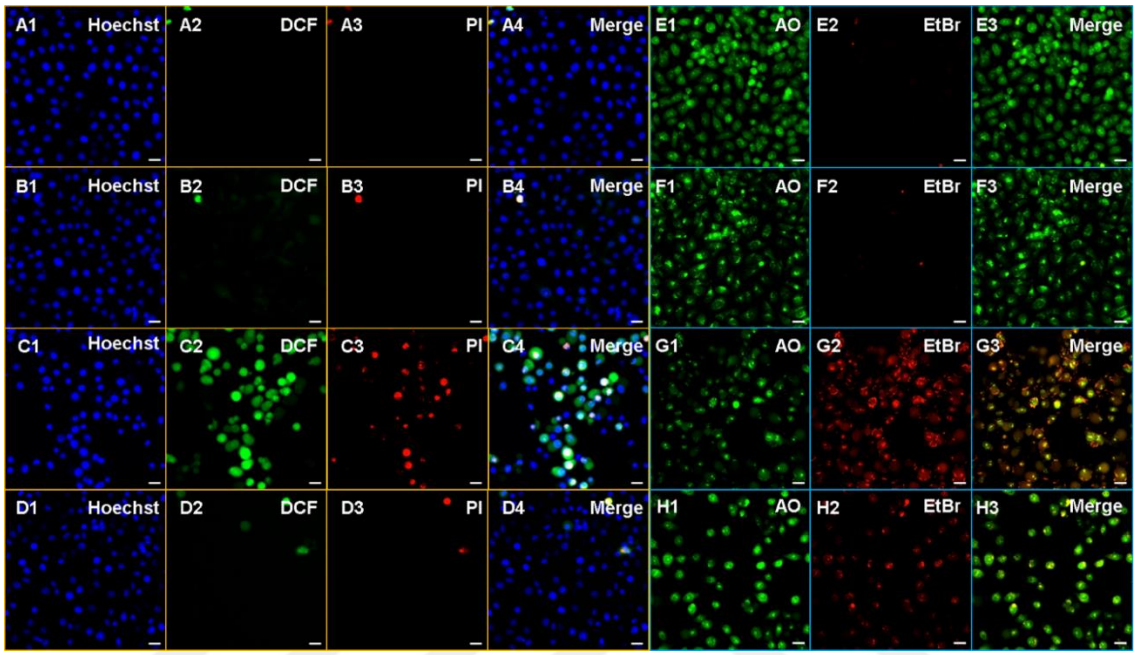

Figure 3.34 Images of triple Hoechst/DCF-DA/PI (A-D) and dual AO/EtBr (E-H) staining of Hela cells treated with DMSO (0.2%) (A1-4, E1-3) or IC_{50} values of DCM_O-I-Cys for 2 h at dark (B1-4, F1-3), followed by 2 h LED light (595 nm 9.83 mw/cm^2) illumination (C1-4, G1-3) in the presence of NaN_3 (10 mM) (D1-4, H1-3). Hoechst 33342; DCF: 2′−7′- dichlorofluorescein; PI: Propium iodide; AO: Acridine orange; EtBr: Ethidium bromide. Scale bar: 50 μm.

Furthermore, confocal microscopy was used to evaluate the imaging capabilities of DCM_O-I-Cys. A time-dependent rise in cytosolic fluorescence signal was seen in HeLa cells, suggesting that the agent might be used as an activatable theranostic agent (Figure 3.35). On the other hand, DCM_O-I-Cys was activated to some amount in L929 cells, but the signal was less than in HeLa cells (Figure 3.36), indicating that the agent was not sufficiently activated to promote efficient cell death, as seen by cell viability data.

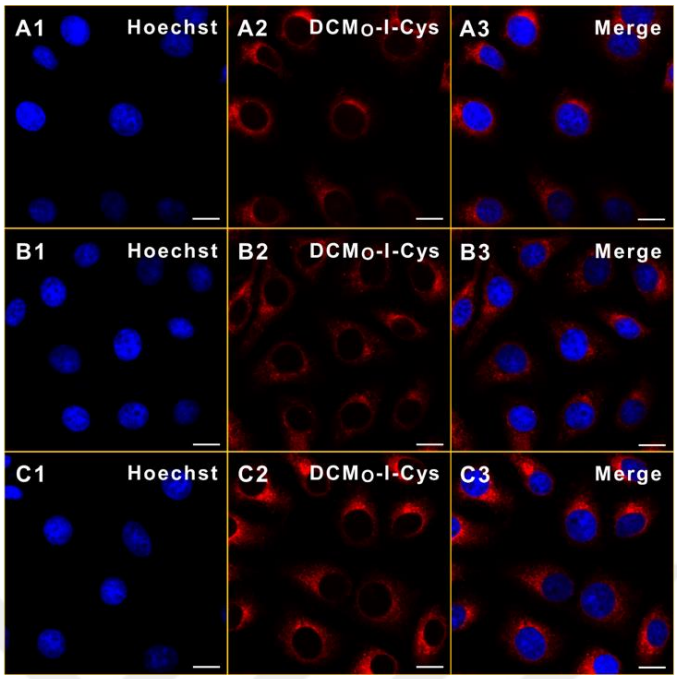

Figure 3.35 Time dependent cellular internalization of DCM_O-I-Cys in HeLa cells after 30 min (A1-3), 1 h (B1-3), 2 h (C1-3). Blue:Hoechst 33342; red: DCM_O-I-Cys. Scale bar: 10 μm.

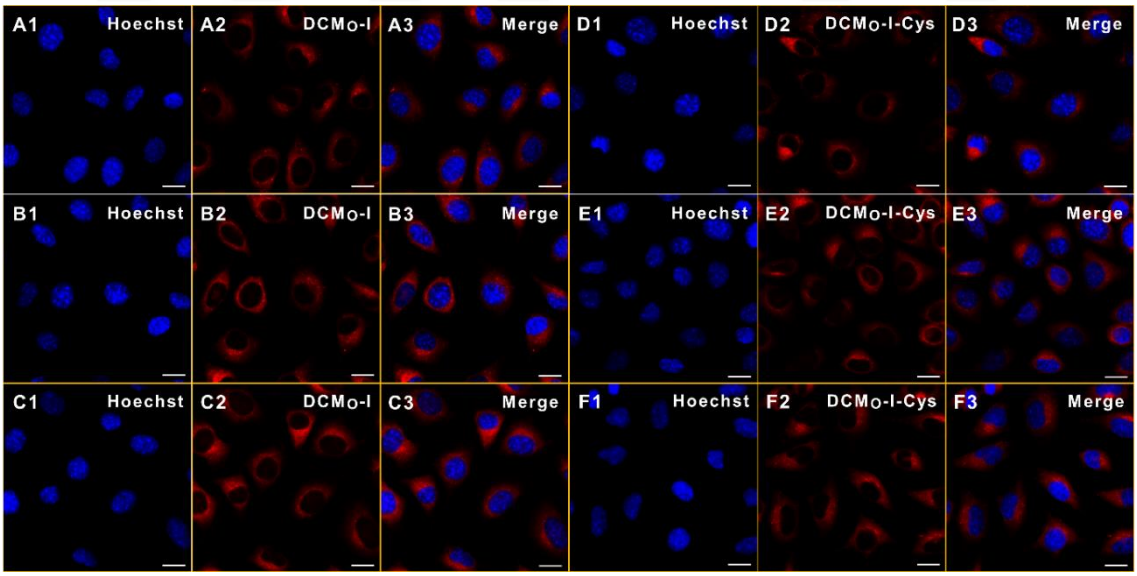

Figure 3.36 Time dependent cellular internalization of **DCM_O- I (A-C)** and **DCM_O-I-Cys (D-F)** in **L929** cells after 30 min **(A1-3, D1-3)**, 1 h **(B1-3, E1-3)**, 2 h **(C1-3, F1-3)**. Blue:Hoechst 33342; red: **DCM_O- I** or **DCM_O-I-Cys**. Scale bar: 10 μm.

3.3 *DCM$_S$ Derivative as Photosensitizers*

3.3.1 *Synthesis of DCM$_S$ Derivative as Photosensitizers*

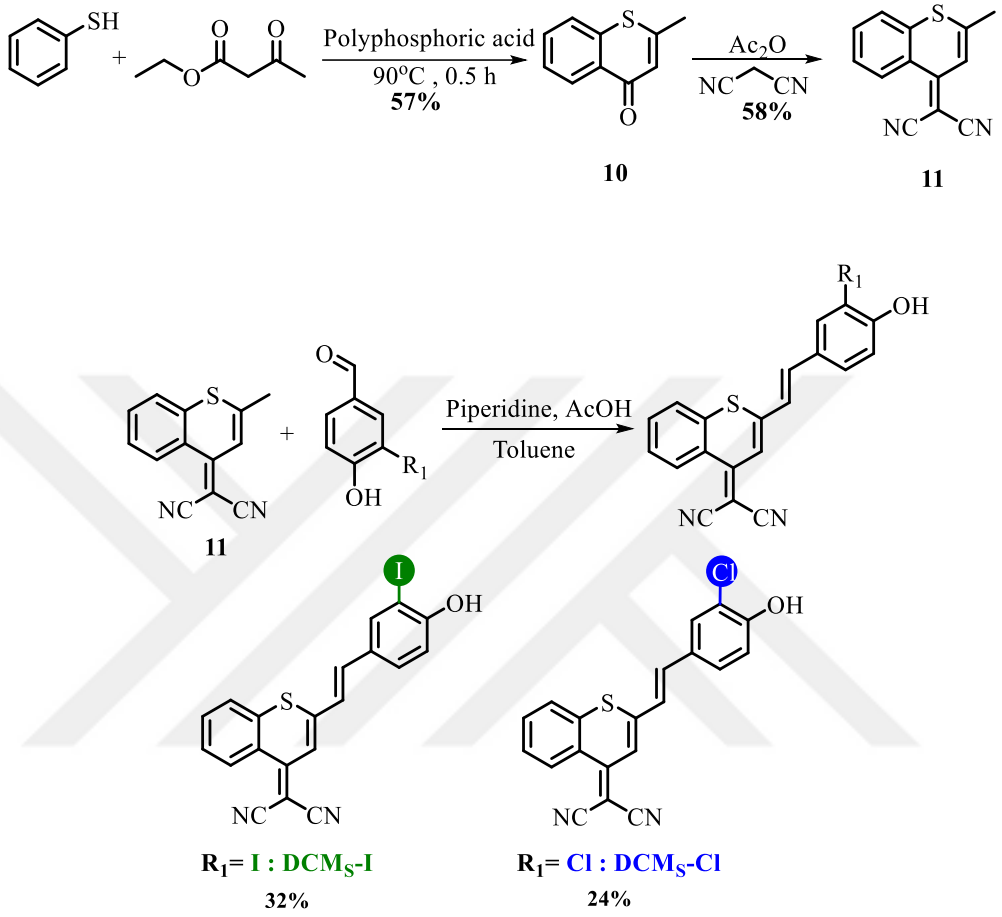

Figure 3.36 Synthetic procedure for DCM$_S$ Based Photosensitizers

As shown in Figure 3.37, **DCM$_S$-Cl** and **DCM$_S$-I** were prepared by replacing oxygen atom with sulfur atom. We focused on sulfur analogues and initially developed heavy-atom free **DCM$_S$-Cl** to see whether sulfur itself will be able to allow ISC as in the case of several sulfur-substituted PSs such as methylene blue[95,96] and thionapthalimides.[97] Finally, we introduced DCM$_S$-I, an iodine carrying sulfur-substituted DCM to observe the effect of a heavy atom on the sulfur analogue. To obtain sulfur analogues, first sulfur substituted DCM core was synthesized. Benzenethiol and ethyl acetoacetate were initially reacted in polyphosphoric acid to afford sulfur-chromone (**10**) and then sulfur-DCM (**11**) was obtained by reacting (**10**) and malononitrile in the presence of acetic anhydride. Knoevenagel condensation of (**11**) either with compoun (**6**) or compound (**5**) gave **DCM$_S$-Cl** and **DCM$_S$-I** respectively.

3.3.2 *Photophysical Characterization of DCM_S Based aPS Cores*

After replacement of the oxygen atom with the sulfur atom, the DCM_S based cores showed red shifted signals compared to DCM_O based ones that can be clearly seen in Figure 3.37. **DCM_S-Cl** and **DCM_S-I** exhibited absorption peaks at 570 nm and 580 nm respectively, which is slightly red-shifted (10 to 20 nm) signals compared to DCM_O based PSs. In the case of fluorescence measurements, significantly red-shifted emission signals were observed with **DCM_S-Cl** (λ_{em} = 762 nm) and **DCM_S-I** (λ_{em} = 756 nm).

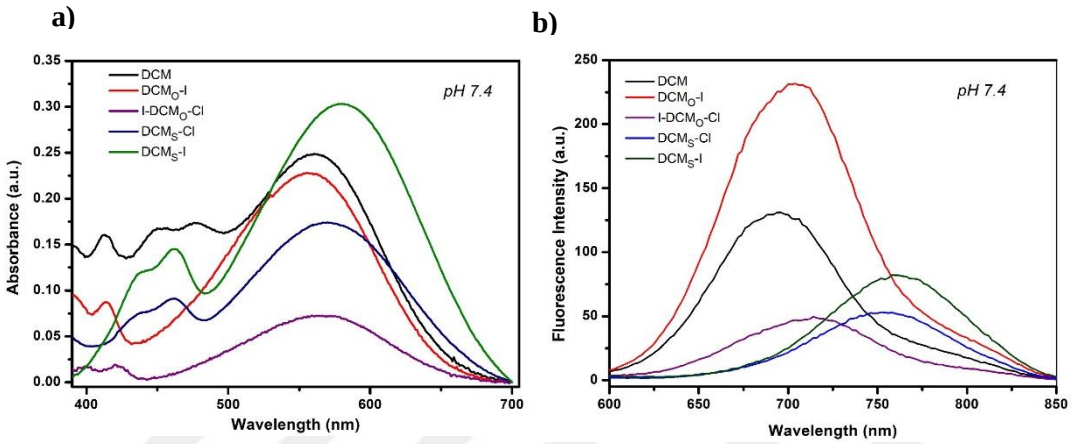

Figure 3.38 (a) Absorption and (b) fluorescence spectra of **DCM_S-Cl** and **DCM_S-I** compared to **DCM, DCMo-I** and **I-DCM_O-Cl.**

Introducing an electron-withdrawing group, **Cl** or **I,** into the phenol ring of DCM_S decreased the pKa of the phenolic hydroxyl group and made deprotonation effective under physiological conditions. The pH value was established to be 7.4 based on the plot of the pH-dependent increase in both absorbance and fluorescence spectrums of **DCM_S-Cl** and **DCM_S-I.** (Figure 3.39 and Figure 3.40). The fluorescence quantum yields of fully deprotonated **DCM_S-Cl** and **DCM_S-I** were calculated to be 3.2 and 5.3% in DMSO solvent.

Table 6 Photophysical parameters and $^1O_2$ quantum yields of DCM_S derivatives.

	λ_{abs} (nm)	λ_{em} (nm)	$\varepsilon(M^{-1}cm^{-1})$	ϕ_F (%)[a]	ϕ_Δ (%)
DCM_S-Cl	570	762	17380	3.2	1.3
DCM_S-I	580	756	30320	5.3	2.7

(a) The fluorescence quantum yield measurement was carried out using Compound **12** in DCM (quantum yield was reported as 0.5958 in DCM). All tests were measured in DMSO (containing 1% PBS). For fluorescence measurement all spectra was collected with a slit width: (10/10)

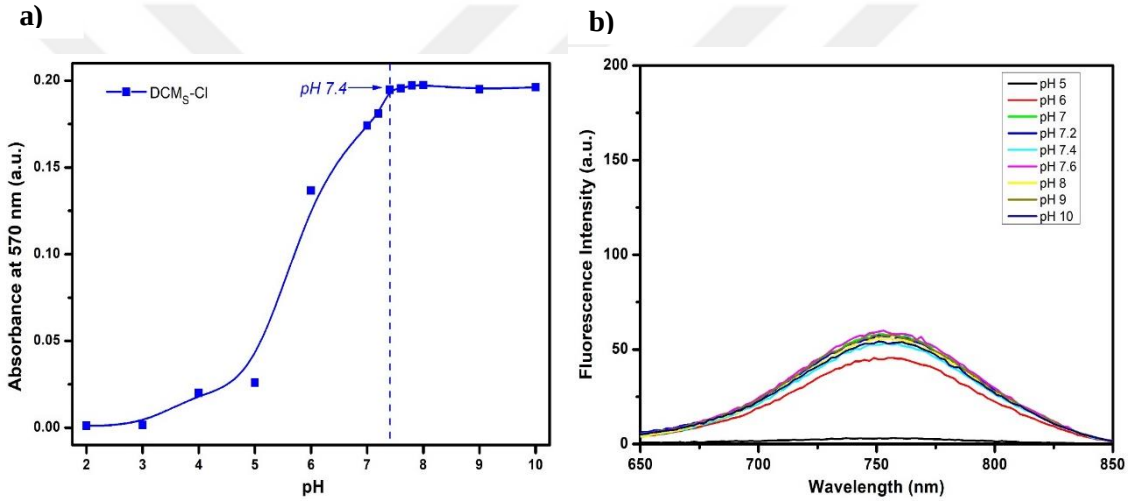

Figure 3.39 (a) Absorption and (b) fluorescence emission spectra of **DCM_S-Cl** in aqueous solutions with different pH values.

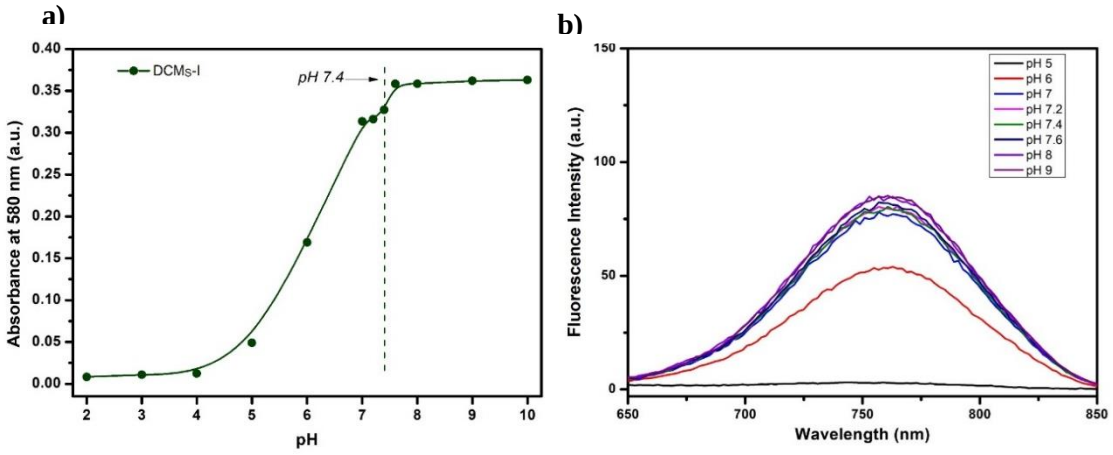

Figure 3.39 (a) Absorption and (b) fluorescence emission spectra of **DCM_S-I** in aqueous solutions with different pH values.

3.3.3 *Chemical Detection of Singlet Oxygen Production of DCM$_S$ Based aPS Cores*

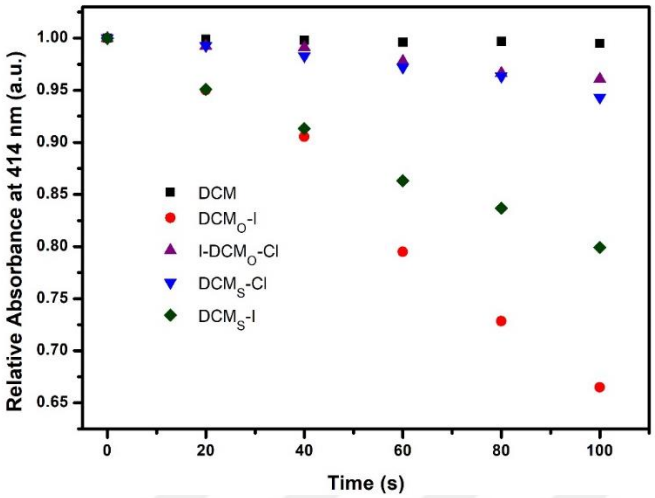

Figure 3.40 Relative $^1O_2$ generation efficiency of **DCM$_S$-Cl** and **DCM$_S$-I** (10 μM) compared to DCM, DCMo-I and I-DCM$_O$-Cl.by using DPBF as a $^1O_2$ trap molecule. In the case of fluorescence measurements, excitation wavelength and slid withs were adjusted to 555 nm and 10/10 respectively.

Replacing oxygen with a sulfur atom on chromone ring to generate heavy atom free DCM$_S$-Cl resulted in lower $^1O_2$ generation capacity (ϕ_Δ = 1.3 %). Insertion of heavy iodine on the phenolate ring of the sulfur analogue increased the yield by 2-fold (ϕ_Δ = 2.7 %), again proving the impact of iodine but still its performance appeared to be poor compared to DCM$_O$-I (Figure 3.41, Figure 3.42 and Figure 3.43).

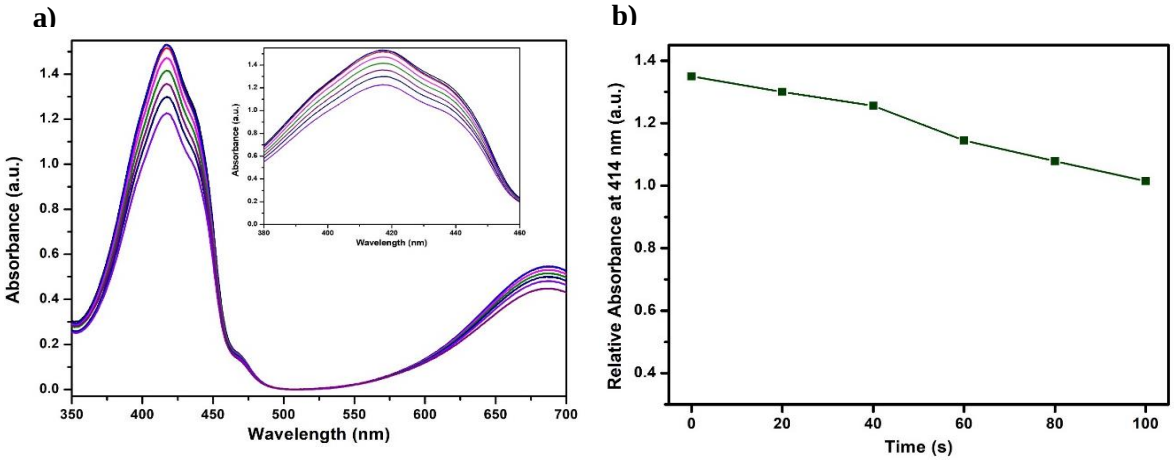

Figure 3.41 (a) Absorption spectra of DPBF upon irradiating **DCM$_S$-I** (10 μM) containing DMSO solution (1% PBS, pH 7.4) with a 630 nm LED light. (b) change in the absorption signal of DPBF at 414 nm upon irradiation with 630 nm LED light.

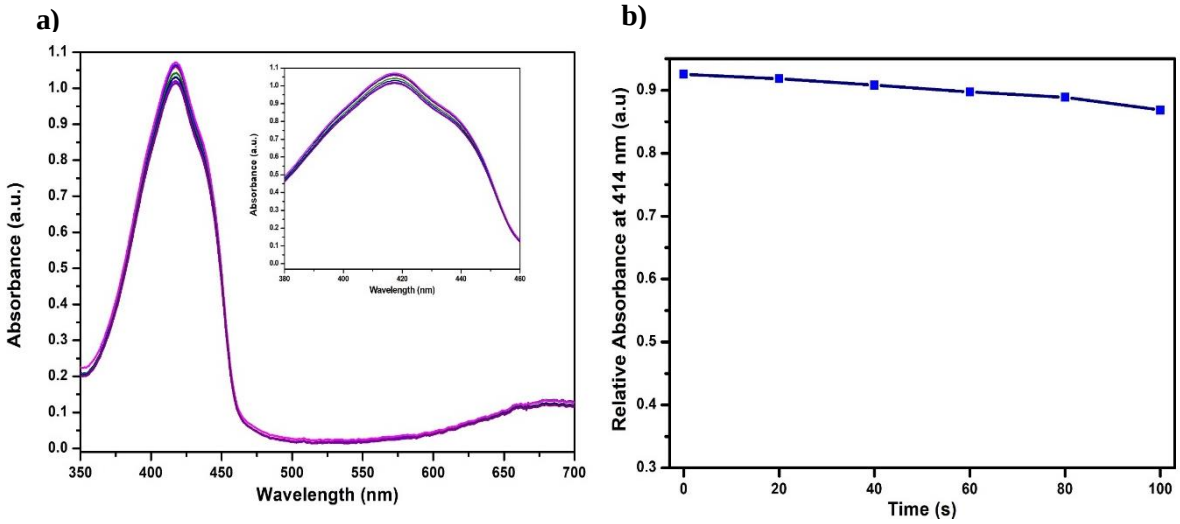

Figure 3.42 (a) Absorption spectra of DPBF upon irradiating **DCMs-Cl** (10 μM) containing DMSO solution (1% PBS, pH 7.4) with a 630 nm LED light. (b) change in the absorption signal of DPBF at 414 nm upon irradiation with 630 nm LED light.

Chapter 4:

CONCLUSION

This thesis covers three topics: selective fluorescence sensing of Cu^+, development of DCM-based aPSs, while investigating the effect of heavy atom positioning in D-π-A structure and finding alternative pathways for the generation of singlet oxygen for PDT applications using sulfur substituted DCM derivatives. Almost all of these studies gave novel and exciting results such as (i) fluorescent detection of the Cu^+ for the first time using ratiometric DCM fluorophore (ii) first example of introducing iodine in different positions in DCM core (iii) detailed computational studies about DCM based aPSs and their impact in PDT action (iv) first example of an activatable Cys targeted DCM sensitizer for targeted PDT.

Firstly, a Cu^+ selective fluorescent ratiometric probe was designed and the main goal was to introduce a new probe to image the Cu^+ pools in living cells selectively. Due to its ratiometric response, **DCM-Cu** could visualize dynamic changes in labile Cu^+ levels in live cells with copper supplementation and monitoring endogenous labile Cu^+ levels in HeLa cells.

Two different types of photosensitizers for activatable PDT action were synthesized in the second part. This study has demonstrated the importance of heavy atom replacement in parental core or *ortho* positions for the activation process of the PDT. Oxygen-substituted DCM was designed as a phototheranostic PDT agent for the first time by introducing an iodine atom into the core structure. It was found that the presence of the iodine atom alone is not sufficient to get high $^1O_2$ generation yield as understood from chemical trap experiments, but its location is also highly critical. DCM_O-I, which bears the iodine on the phenolate ring, performed better. TDDFT calculations suggested a rationale for the enhanced singlet oxygen production activity of DCMo-I. Analysis of the electronic topology of the target triplet state involved in intersystem crossing shows that the departing density, i.e., the electron density moved from the initial to the final state, is highly localized on the phenolate moiety of the molecule. The proximity of the iodine to the departing electron density appears to significantly impact the magnitude of spin orbit coupling, explaining the lower activity in I-DCM_O-Cl. When DCM_O-I was tested in cell cultures, it exhibited high photocytotoxicity in HeLa cancer cells along with a strong fluorescence signal, proving its phototheranostic nature. Based on the promising results

obtained with DCM_O-I, the core was utilized to develop a Cys activatable aPSs (DCM_O-I-Cys) by masking the phenol with a Cys responsive cage unit. DCM_O-I-Cys induced significant photocytotoxicity in HeLa cells when activated by an endogenous Cys. In contrast, it stayed in its off state in normal L929 cells and cell viabilities remained unperturbed. DCM_O-I-Cys was also used successfully to image the Cys activity in cancer cells under confocal microscopy.

To close, this study suggests that DCM_O-I can be utilized as a highly attractive phototheranostic scaffold, which can be easily converted to an aPSs as in the case of DCM_O-I-Cys. DCM_O-I-Cys marks the first-ever example of a Cys-responsive DCM-based PS. DCM-based PSs introduce exciting new opportunities for cancer cell-specific therapeutics, particularly in the scope of phototherapies. Finally, it is worth mentioning that the DCM cores exhibit strong two-photon absorption characteristics, which can be implemented for deep tissue penetration in *in vivo* studies.

BIBLIOGRAPHY

(1) Senga, S. S.; Grose, R. P. Hallmarks of Cancer—the New Testament. *Open Biol.* **2021**, *11* (1).

(2) Tohme, S.; Simmons, R. L.; Tsung, A. Surgery for Cancer: A Trigger for Metastases. *Cancer Res.* **2017**, *77* (7), 1548.

(3) Ward, R. A.; Fawell, S.; Floc'h, N.; Flemington, V.; Mckerrecher, D.; Smith, P. D. Challenges and Opportunities in Cancer Drug Resistance. *Chem. Rev.* **2020**.

(4) Gunaydin, G.; Gedik, M. E.; Ayan, S. Photodynamic Therapy for the Treatment and Diagnosis of Cancer–A Review of the Current Clinical Status. *Front. Chem.* **2021**, *9*, 608.

(5) Sobhani, N.; Samadani, A. A. Implications of Photodynamic Cancer Therapy: An Overview of PDT Mechanisms Basically and Practically. *J. Egypt. Natl. Cancer Inst. 2021 331* **2021**, *33* (1), 1–13.

(6) Castano, A. P.; Mroz, P.; Hamblin, M. R. Photodynamic Therapy and Anti-Tumour Immunity. *Nat. Rev. Cancer* **2006**, *6* (7), 535.

(7) Verma, S.; Watt, G. M.; Mai, Z.; Hasan, T. Strategies for Enhanced Photodynamic Therapy Effects†. *Photochem. Photobiol.* **2007**, *83* (5), 996–1005.

(8) Nguyen, L.; Li, M.; Woo, S.; You, Y. Development of Prodrugs for PDT-Based Combination Therapy Using a Singlet-Oxygen-Sensitive Linker and Quantitative Systems Pharmacology. *J. Clin. Med.* **2019**, *8* (12).

(9) Aubry, J. M.; Pierlot, C.; Rigaudy, J.; Schmidt, R. Reversible Binding of Oxygen to Aromatic Compounds. *Acc. Chem. Res.* **2003**, *36* (9), 668–675.

(10) Dougherty, T. J.; Gomer, C. J.; Henderson, B. W.; Jori, G.; Kessel, D.; Korbelik, M.; Moan, J.; Peng, Q. Photodynamic Therapy. *J. Natl. Cancer Inst.* **1998**, *90* (12), 889.

(11) Celli, J. P.; Spring, B. Q.; Rizvi, I.; Evans, C. L.; Samkoe, K. S.; Verma, S.; Pogue, B. W.; Hasan, T. Imaging and Photodynamic Therapy: Mechanisms, Monitoring, and Optimization. *Chem. Rev.* **2010**, *110* (5), 2795–2838.

(12) Zhou, Z.; Song, J.; Nie, L.; Chen, X. Reactive Oxygen Species Generating Systems Meeting Challenges of Photodynamic Cancer Therapy. *Chem. Soc. Rev.* **2016**, *45* (23), 6597–6626.

(13) Fan, W.; Huang, P.; Chen, X. Overcoming the Achilles' Heel of Photodynamic Therapy. *Chem. Soc. Rev.* **2016**, *45* (23), 6488–6519.

(14) Liu, M.; Li, C. Recent Advances in Activatable Organic Photosensitizers for Specific Photodynamic Therapy. *Chempluschem* **2020**, *85* (5), 948–957.

(15) Yang, M.; Li, X.; Yoon, J. Activatable Supramolecular Photosensitizers: Advanced Design Strategies. *Mater. Chem. Front.* **2021**, *5* (4), 1683–1693.

(16) Lovell, J. F.; Liu, T. W. B.; Chen, J.; Zheng, G. Activatable Photosensitizers for Imaging and Therapy. *Chem. Rev.* **2010**, *110* (5), 2839–2857.

(17) Filatov, M. A. Heavy-Atom-Free BODIPY Photosensitizers with Intersystem Crossing Mediated by Intramolecular Photoinduced Electron Transfer. *Org. Biomol. Chem.* **2019**, *18* (1), 10–27.

(18) Prudhomme, D. R.; Wang, Z.; Rizzo, C. J. An Improved Photosensitizer for the Photoinduced Electron-Transfer Deoxygenation of Benzoates and m-(Trifluoromethyl)Benzoates. *J. Org. Chem.* **1997**, *62* (23), 8257–8260.

(19) Lovell, J. F.; Liu, T. W. B.; Chen, J.; Zheng, G. Activatable Photosensitizers for Imaging and Therapy. *Chem. Rev.* **2010**, *110* (5), 2839–2857.

(20) Majumdar, P.; Nomula, R.; Zhao, J. Activatable Triplet Photosensitizers: Magic Bullets for Targeted Photodynamic Therapy. *J. Mater. Chem. C* **2014**, *2* (30), 5982–5997.

(21) Zhao, X.; Liu, J.; Fan, J.; Chao, H.; Peng, X. Recent Progress in Photosensitizers for Overcoming the Challenges of Photodynamic Therapy: From Molecular Design to Application. *Chem. Soc. Rev.* **2021**, *50* (6), 4185–4219.

(22) Hu, W.; Liu, M.; Zhang, X. F.; Shi, M.; Jia, M.; Hu, X.; Liu, L.; Wang, T. Miniizing the Electron Donor Size of Donor-Acceptor-Type Photosensitizer: Twisted Intramolecular Charge-Transfer-Induced Triplet State and Singlet Oxygen Formation. *J. Phys. Chem. C* **2020**, *124* (43), 23558–23566.

(23) Wu, X.; Sun, X.; Guo, Z.; Tang, J.; Shen, Y.; James, T. D.; Tian, H.; Zhu, W. In Vivo and in Situ Tracking Cancer Chemotherapy by Highly Photostable NIR Fluorescent Theranostic Prodrug. *J. Am. Chem. Soc.* **2014**, *136* (9), 3579–3588.

(24) Wang, X.; Li, P.; Ding, Q.; Wu, C.; Zhang, W.; Tang, B. Observation of Acetylcholinesterase in Stress-Induced Depression Phenotypes by Two-Photon Fluorescence Imaging in the Mouse Brain. *J. Am. Chem. Soc.* **2019**, *141* (5), 2061–2068.

(25) Zhai, W.; Zhang, Y.; Liu, M.; Zhang, H.; Zhang, J.; Li, C. Universal Scaffold for an Activatable Photosensitizer with Completely Inhibited Photosensitivity. *Angew. Chem* **2019**, *131* (46), 16754–16762.

(26) Gu, K.; Xu, Y.; Li, H.; Guo, Z.; Zhu, S.; Zhu, S.; Shi, P.; James, T. D.; Tian, H.; Zhu, W. H. Real-Time Tracking and in Vivo Visualization of β-Galactosidase Activity in Colorectal Tumor with a Ratiometric Near-Infrared Fluorescent Probe. *J. Am. Chem. Soc.* **2016**, *138* (16), 5334–5340.

(27) Atilgan, A.; Tanriverdi Eçik, E.; Guliyev, R.; Uyar, T. B.; Erbas-Cakmak, S.; Akkaya, E. U. Near-IR-Triggered, Remote-Controlled Release of Metal Ions: A Novel

Strategy for Caged Ions. *Angew. Chem. Int. Ed. Engl.* **2014**, *53* (40), 10678–10681.

(28) Digby, E. M.; Sadovski, O.; Beharry, A. A. An Activatable Photosensitizer Targeting Human NAD(P)H: Quinone Oxidoreductase 1. *Chem. - A Eur. J.* **2020**, *26* (12), 2713–2718.

(29) Yang, Z.; Xu, W.; Wang, J.; Liu, L.; Chu, Y.; Wang, Y.; Hu, Y.; Yi, T.; Hua, J. Diketopyrrolopyrrole-Based Multifunctional Ratiometric Fluorescent Probe and γ-Glutamyltranspeptidase-Triggered Activatable Photosensitizer for Tumor Therapy. *J. Mater. Chem. C* **2020**, *8* (24), 8183–8190.

(30) Tian, X.; Baek, K. H.; Shin, I. Dual-Targeting Delivery System for Selective Cancer Cell Death and Imaging. *Chem. Sci.* **2013**, *4* (3), 947–956.

(31) Yuan, Y.; Xu, S.; Zhang, C. J.; Zhang, R.; Liu, B. Dual-Targeted Activatable Photosensitizers with Aggregation-Induced Emission (AIE) Characteristics for Image-Guided Photodynamic Cancer Cell Ablation. *J. Mater. Chem. B* **2015**, *4* (1), 169–176.

(32) Lau, J. T. F.; Lo, P. C.; Jiang, X. J.; Wang, Q.; Ng, D. K. P. A Dual Activatable Photosensitizer toward Targeted Photodynamic Therapy. *J. Med. Chem.* **2014**, *57* (10), 4088–4097.

(33) Sun, J.; Du, K.; Diao, J.; Cai, X.; Feng, F.; Wang, S. GSH and H2O2 Co-Activatable Mitochondria-Targeted Photodynamic Therapy under Normoxia and Hypoxia. *Angew. Chemie - Int. Ed.* **2020**, *59* (29), 12122–12128.

(34) Celli, J. P.; Spring, B. Q.; Rizvi, I.; Evans, C. L.; Samkoe, K. S.; Verma, S.; Pogue, B. W.; Hasan, T. Imaging and Photodynamic Therapy: Mechanisms, Monitoring, and Optimization. *Chem. Rev.* **2010**, *110* (5), 2795–2838.

(35) Yi, X.; Wang, F.; Qin, W.; Yang, X.; Yuan, J. Near-Infrared Fluorescent Probes in Cancer Imaging and Therapy: An Emerging Field. *Int. J. Nanomedicine Dovepress* **2014**.

(36) Wang, Z.; Meng, Q.; Li, S. The Role of NIR Fluorescence in MDR Cancer Treatment: From Targeted Imaging to Phototherapy. *Curr. Med. Chem.* **2019**, *27* (33), 5510–5529.

(37) Wang, Y.; Yu, H.; Zhang, Y.; Jia, C.; Ji, M. Development and Application of Several Fluorescent Probes in near Infrared Region. *Dye. Pigment.* **2021**, *190*, 109284.

(38) Yi, X. M.; Wang, F. L.; Qin, W. J.; Yang, X. J.; Yuan, J. L. Near-Infrared Fluorescent Probes in Cancer Imaging and Therapy: An Emerging Field. *Int. J. Nanomedicine* **2014**, *9* (1), 1347–1365.

(39) Luo, S.; Zhang, E.; Su, Y.; Cheng, T.; Shi, C. A Review of NIR Dyes in Cancer Targeting and Imaging. *Biomaterials* **2011**, *32* (29), 7127–7138.

(40) Almammadov, T.; Kolemen, S. A Hydrogen Peroxide Responsive Resorufin-Based Phototheranostic Agent for Selective Treatment of Cancer Cells. *Dye. Pigment.* **2021**, *193* (April), 109499.

(41) Arslan, B.; Bilici, K.; Demirci, G.; Almammadov, T.; Khan, M.; Sennaroglu, A.; Acar, H. Y.; Kolemen, S. A Leucine Aminopeptidase Activatable Photosensitizer for Cancer Cell Selective Photodynamic Therapy Action. *Dye. Pigment.* **2021**, *195*, 109735.

(42) Cetin, S.; Elmazoglu, Z.; Karaman, O.; Gunduz, H.; Gunbas, G.; Kolemen, S. Balanced Intersystem Crossing in Iodinated Silicon-Fluoresceins Allows New Class of Red Shifted Theranostic Agents. *ACS Med. Chem. Lett.* **2021**, *12* (5), 752–757.

(43) Guo, Z.; Zhu, W.; Tian, H. Dicyanomethylene-4H-Pyran Chromophores for OLED Emitters, Logic Gates and Optical Chemosensors. *Chem. Commun.* **2012**, *48* (49), 6073–6084.

(44) Tang, C. W.; Vanslyke, S. A.; Chen, C. H. Electroluminescence of Doped Organic Thin Films. *J. Appl. Phys.* **1989**, *65* (9), 3610.

(45) Peng, X.; Du, J.; Fan, J.; Wang, J.; Wu, Y.; Zhao, J.; Sun, S.; Xu, T. A Selective Fluorescent Sensor for Imaging Cd 2+ in Living Cells. *J. Am. Chem. Soc.* **2007**, *129* (6), 1500–1501.

(46) Yu, D.; Huang, F.; Ding, S.; Feng, G. Near-Infrared Fluorescent Probe for Detection of Thiophenols in Water Samples and Living Cells. *Anal. Chem* **2014**, *86*, 50.

(47) Yu, D.; Zhang, Q.; Ding, S.; Feng, G. A Colorimetric and Near-Infrared Fluorescent Probe for Biothiols and Its Application in Living Cells. *RSC Adv.* **2014**, *4* (87), 46561–46567.

(48) Ma, J.; Fan, J.; Li, H.; Yao, Q.; Xia, J.; Wang, J.; Peng, X. Probing Hydrazine with a Near-Infrared Fluorescent Chemodosimeter. *Dye. Pigment.* **2017**, *138*, 39–46.

(49) Zeng, X.; Chen, Z.; Tang, L.; Yang, H.; Liu, N.; Zhou, H.; Li, Y.; Wu, J.; Deng, Z.; Yu, Y.; Deng, H.; Hong, X.; Xiao, Y. A Novel Near-Infrared Fluorescent Light-up Probe for Tumor Imaging and Drug-Induced Liver Injury Detection †. *Chem. Commun* **2019**, *55*, 2541.

(50) Wang, W. X.; Jiang, W. L.; Liu, Y.; Li, Y.; Zhang, J.; Li, C. Y. Near-Infrared Fluorescence Probe with a Large Stokes Shift for Visualizing Hydrogen Peroxide in Ulcerative Colitis Mice. *Sensors Actuators, B Chem.* **2020**, *320*.

(51) Wu, X.; Wang, R.; Qi, S.; Kwon, N.; Han, J.; Kim, H.; Li, H.; Yu, F.; Yoon, J. Rational Design of a Highly Selective Near-Infrared Two-Photon Fluorogenic Probe for Imaging Orthotopic Hepatocellular Carcinoma Chemotherapy. *Angew. Chemie - Int. Ed.* **2021**.

(52) Li, M.; Wu, X.; Wang, Y.; Li, Y.; Zhu, W.; James, T. D. A Near-Infrared Colorimetric Fluorescent Chemodosimeter for the Detection of Glutathione in Living Cells. *Chem. Commun.* **2014**, *50* (14), 1751–1753.

(53) Bao, B.; Liu, M.; Liu, Y.; Zhang, X.; Zang, Y.; Li, J.; Lu, W. NIR Absorbing

DICPO Derivatives Applied to Wide Range of PH and Detection of Glutathione in Tumor. *Tetrahedron* **2015**, *71* (41), 7865–7868.

(54) Yang, D.; Tian, H. Y.; Zang, T. N.; Li, M.; Zhou, Y.; Zhang, J. F. Hypoxia Imaging in Cells and Tumor Tissues Using a Highly Selective Fluorescent Nitroreductase Probe. *Sci. Reports 2017 71* **2017**, *7* (1), 1–8.

(55) Wang, Y.; Yu, F.; Luo, X.; Li, M.; Zhao, L.; Yu, F. Visualization of Carboxylesterase 2 with a Near-Infrared Two-Photon Fluorescent Probe and Potential Evaluation of Its Anticancer Drug Effects in an Orthotopic Colon Carcinoma Mice Model. *Chem. Commun.* **2020**, *56* (32), 4412–4415.

(56) Yang, Z.; Li, W.; Chen, H.; Mo, Q.; Li, J.; Zhao, S.; Hou, C.; Qin, J.; Su, G. Inhibitor Structure-Guided Design and Synthesis of near-Infrared Fluorescent Probes for Monoamine Oxidase A (MAO-A) and Its Application in Living Cells and in Vivo. *Chem. Commun.* **2019**, *55* (17), 2477–2480.

(57) Wang, P.; Wang, K.; Chen, D.; Mao, Y.; Gu, Y. A Novel Colorimetric and Near-Infrared Fluorescent Probe for Hydrogen Peroxide Imaging in Vitro and in Vivo. *RSC Adv.* **2015**, *5* (104), 85957–85963.

(58) He, M.; Li, C.; Pang, Z.; Chen, K.; Tan, Y.; Huang, Y.; Lu, Z. A New Phenolate-Ion-Type Two-Photon Near Infrared Fluorophore-Based Biosensor for High-Performance Detection of HNO. *Chem. – A Eur. J.* **2020**, *26* (53), 12140–12144.

(59) Zhang, Y. Y.; Chen, X. Z.; Liu, X. Y.; Zhang, X. Y.; Gao, G.; Hou, S. C.; Wang, H. M. A Highly Selective and Ultrafast Near-Infrared Fluorescent Turn-on and Colorimetric Probe for Hypochlorite in Living Cells. *Anal. Chim. Acta* **2019**, *1078*, 135–141.

(60) Xu, F.; Wang, Q.; Jiang, L.; Zhu, F.; Yang, L.; Zhang, S.; Song, X. Evaluation of Nitric Oxide Fluctuation Via a Fast, Responsive Fluorescent Probe in Idiopathic Pulmonary Fibrosis Cells and Mice Models. *Anal. Chem.* **2022**, acs.analchem.1c05643.

(61) Mulay, S. V.; Kim, Y.; Lee, K. J.; Yudhistira, T.; Park, H. S.; Churchill, D. G. A Fluorogenic and Red-Shifted Diphenyl Phosphinate-Based Probe for Selective Peroxynitrite Detection as Demonstrated in Fixed Cells. *New J. Chem.* **2017**, *41* (20), 11934–11940.

(62) Jie, X.; Wu, M.; Yang, H.; Wei, W. Red–Near-Infrared Fluorescent Probe for Time-Resolved in Vivo Alkaline Phosphatase Detection with the Assistance of a Photoresponsive Nanocontainer. *Anal. Chem.* **2019**, *91* (20), 13174–13182.

(63) Li, Q.; Yan, C.; Zhang, J.; Guo, Z.; Zhu, W. H. Ratiometric and Light-up near-Infrared Fluorescent DCM-Based Probe for Real-Time Monitoring Endogenous Tyrosinase Activity. *Dye. Pigment.* **2019**, *162*, 802–807.

(64) Cotruvo, J. A.; Aron, A. T.; Ramos-Torres, K. M.; Chang, C. J. Synthetic Fluorescent Probes for Studying Copper in Biological Systems. *Chem. Soc. Rev.* **2015**,

44 (13), 4400–4414.

(65) Maity, D.; Raj, A.; Karthigeyan, D.; Kundu, T. K.; Govindaraju, T. Reaction-Based Probes for Co(Ii) and Cu(i) with Dual Output Modes: Fluorescence Live Cell Imaging. *RSC Adv.* **2013**, *3* (37), 16788–16794.

(66) Qian, X.; Zhu, W.; Yu, H.; Xu, Y.; Liu, W.; Wang, H. Y.; Liu, Y. Mitochondria-Targeted near-Infrared Fluorescent Probe for Monitoring of a Copper(I) in Living Cells and In Vivo. *Dye. Pigment.* **2021**, *194*, 109561.

(67) Kardos, J.; Héja, L.; Simon, Á.; Jablonkai, I.; Kovács, R.; Jemnitz, K. Correction to: Copper Signalling: Causes and Consequences. *Cell Commun. Signal.* **2018**, *16* (1), 1–22.

(68) Ge, E. J.; Bush, A. I.; Casini, A.; Cobine, P. A.; Cross, J. R.; DeNicola, G. M.; Dou, Q. P.; Franz, K. J.; Gohil, V. M.; Gupta, S.; Kaler, S. G.; Lutsenko, S.; Mittal, V.; Petris, M. J.; Polishchuk, R.; Ralle, M.; Schilsky, M. L.; Tonks, N. K.; Vahdat, L. T.; Van Aelst, L.; Xi, D.; Yuan, P.; Brady, D. C.; Chang, C. J. Connecting Copper and Cancer: From Transition Metal Signalling to Metalloplasia. *Nat. Rev. Cancer* **2022**, *22* (2), 102–113.

(69) Yu, K. K.; Li, K.; Hou, J. T.; Yu, X. Q. Coumarin-TPA Derivative: A Reaction-Based Ratiometric Fluorescent Probe for Cu(I). *Tetrahedron Lett.* **2013**, *54* (43), 5771–5774.

(70) Zeng, L.; Miller, E. W.; Pralle, A.; Isacoff, E. Y.; Chang, C. J. A Selective Turn-on Fluorescent Sensor for Imaging Copper in Living Cells. *J. Am. Chem. Soc.* **2006**, *128* (1), 10–11.

(71) Taki, M.; Akaoka, K.; Mitsui, K.; Yamamoto, Y. A Mitochondria-Targeted Turn-on Fluorescent Probe Based on a Rhodol Platform for the Detection of Copper(I). *Org. Biomol. Chem.* **2014**, *12* (27), 4999–5005.

(72) Chung, C. Y. S.; Posimo, J. M.; Lee, S.; Tsang, T.; Davis, J. M.; Brady, D. C.; Chang, C. J. Activity-Based Ratiometric FRET Probe Reveals Oncogene-Driven Changes in Labile Copper Pools Induced by Altered Glutathione Metabolism. *Proc. Natl. Acad. Sci. U. S. A.* **2019**, *116* (37), 18285–18294.

(73) Dodani, S. C.; Leary, S. C.; Cobine, P. A.; Winge, D. R.; Chang, C. J. A Targetable Fluorescent Sensor Reveals That Copper-Deficient SCO1 and SCO2 Patient Cells Prioritize Mitochondrial Copper Homeostasis. *J. Am. Chem. Soc.* **2011**, *133* (22), 8606–8616.

(74) Yan, F.; Sun, X.; Zu, F.; Bai, Z.; Jiang, Y.; Fan, K.; Wang, J. Fluorescent Probes for Detecting Cysteine. *Methods Appl. Fluoresc.* **2018**, *6* (4).

(75) Forman, H. J.; Zhang, H.; Rinna, A. Glutathione: Overview of Its Protective Roles, Measurement, and Biosynthesis. *Mol. Aspects Med.* **2009**, *30* (1–2), 1–12.

(76) Zhang, R.; Yong, J.; Yuan, J.; Ping Xu, Z. Recent Advances in the Development

of Responsive Probes for Selective Detection of Cysteine. *Coord. Chem. Rev.* **2020**, *408*, 213182.

(77) Ding, S.; Feng, G. Smart Probe for Rapid and Simultaneous Detection and Discrimination of Hydrogen Sulfide, Cysteine/Homocysteine, and Glutathione. *Sensors Actuators, B Chem.* **2016**, *235*, 691–697.

(78) Yang, X.; Liu, W.; Tang, J.; Li, P.; Weng, H.; Ye, Y.; Xian, M.; Tang, B.; Zhao, Y. A Multi-Signal Mitochondria-Targeted Fluorescent Probe for Real-Time Visualization of Cysteine Metabolism in Living Cells and Animals. *Chem. Commun.* **2018**, *54* (81), 11387–11390.

(79) Liu, X.; Yang, D.; Chen, W.; Yang, L.; Qi, F.; Song, X. A Red-Emitting Fluorescent Probe for Specific Detection of Cysteine over Homocysteine and Glutathione with a Large Stokes Shift. *Sensors Actuators B Chem.* **2016**, *234*, 27–33.

(80) iu, T.; Huo, F.; Li, J.; Chao, J.; Zhang, Y.; Yin, C. An Off-on Fluorescent Probe for Specifically Detecting Cysteine and Its Application in Bioimaging. *Sensors Actuators, B Chem.* **2016**, *237*, 127–132.

(81) Kang, Y. F.; Qiao, H. X.; Meng, Y. L.; Xin, Z. H.; Ge, L. P.; Zheng, J. N.; Wang, Y. N. A Simple and Sensitive Fluorescent Probe for Specific Detection of Cysteine. *J. Chem. Sci.* **2017**, *129* (8), 1219–1223.

(82) Niu, W.; Guo, L.; Li, Y.; Shuang, S.; Dong, C.; Wong, M. S. Highly Selective Two-Photon Fluorescent Probe for Ratiometric Sensing and Imaging Cysteine in Mitochondria. *Anal. Chem.* **2016**, *88* (3), 1908.

(83) Kang, Y. F.; Qiao, H. X.; Meng, Y. L.; Cui, S. J.; Han, Y. J.; Wu, Z. Y.; Wu, J.; Jia, X. H.; Zhang, X. L.; Dai, M. Y. Rapid and Selective Detection of Cysteine over Homocysteine and Glutathione by a Simple and Effective Coumarin-Based Fluorescent Probe. *RSC Adv.* **2016**, *6* (97), 94866.

(84) Liu, Y.; Yu, D.; Ding, S.; Xiao, Q.; Guo, J.; Feng, G. Rapid and Ratiometric Fluorescent Detection of Cysteine with High Selectivity and Sensitivity by a Simple and Readily Available Probe. *ACS Appl. Mater. Interfaces* **2014**, *6* (20), 17543.

(85) Zhu, B.; Guo, B.; Zhao, Y.; Zhang, B.; Du, B. A Highly Sensitive Ratiometric Fluorescent Probe with a Large Emission Shift for Imaging Endogenous Cysteine in Living Cells. *Biosens. Bioelectron.* **2014**, *55*, 72.

(86) Qi, Y.; Huang, Y.; Li, B.; Zeng, F.; Wu, S. Real-Time Monitoring of Endogenous Cysteine Levels in Vivo by near-Infrared Turn-on Fluorescent Probe with Large Stokes Shift. *Anal. Chem.* **2018**, *90* (1), 1014–1020.

(87) Guo, Z.; Nam, S.; Park, S.; Yoon, J. A Highly Selective Ratiometric Near-Infrared Fluorescent Cyanine Sensor for Cysteine with Remarkable Shift and Its Application in Bioimaging. *Chem. Sci.* **2012**, *3* (9), 2760–2765.

(88) Xue, S.; Ding, S.; Zhai, Q.; Zhang, H.; Feng, G. A Readily Available Colorimetric

and Near-Infrared Fluorescent Turn-on Probe for Rapid and Selective Detection of Cysteine in Living Cells. *Biosens. Bioelectron.* **2015**, *68*, 316–321.

(89) Shen, R.; Yang, J. J.; Luo, H.; Wang, B.; Jiang, Y. A Sensitive Fluorescent Probe for Cysteine and Cu2+ Based on 1,8-Naphthalimide Derivatives and Its Application in Living Cells Imaging. *Tetrahedron* **2017**, *73* (4), 373–377.

(90) Fu, Y. J.; Li, Z.; Li, C. Y.; Li, Y. F.; Wu, P.; Wen, Z. H. Borondipyrrolemethene-Based Fluorescent Probe for Distinguishing Cysteine from Biological Thiols and Its Application in Cell Image. *Dye. Pigment.* **2017**, *139*, 381–387.

(91) Wei, L. F.; Thirumalaivasan, N.; Liao, Y. C.; Wu, S. P. Fluorescent Coumarin-Based Probe for Cysteine and Homocysteine with Live Cell Application. *Spectrochim. Acta Part A Mol. Biomol. Spectrosc.* **2017**, *183*, 204–208.

(92) Shi, C.; Guo, Z.; Yan, Y.; Zhu, S.; Xie, Y.; Zhao, Y. S.; Zhu, W.; Tian, H. Self-Assembly Solid-State Enhanced Red Emission of Quinolinemalononitrile: Optical Waveguides and Stimuli Response. *ACS Appl. Mater. Interfaces* **2012**, *5* (1), 192–198.

(93) Lutkus, L. V.; Rickenbach, S. S.; McCormick, T. M. Singlet Oxygen Quantum Yields Determined by Oxygen Consumption. *J. Photochem. Photobiol. A Chem.* **2019**, *378*, 131–135.

(94) Sun, W.; Fan, J.; Hu, C.; Cao, J.; Zhang, H.; Xiong, X.; Wang, J.; Cui, S.; Sun, S.; Peng, X. A Two-Photon Fluorescent Probe with near-Infrared Emission for Hydrogen Sulfide Imaging in Biosystems. *Chem. Commun* **2013**, *49*, 3890.

(95) Dao, H. M.; Whang, C. H.; Shankar, V. K.; Wang, Y. H.; Khan, I. A.; Walker, L. A.; Husain, I.; Khan, S. I.; Murthy, S. N.; Jo, S. Methylene Blue as a Far-Red Light-Mediated Photocleavable Multifunctional Ligand. *Chem. Commun.* **2020**, *56* (11), 1673–1676.

(96) Li, Z.; Wang, Y. F.; Zeng, C.; Hu, L.; Liang, X. J. Ultrasensitive Tyrosinase-Activated Turn-On Near-Infrared Fluorescent Probe with a Rationally Designed Urea Bond for Selective Imaging and Photodamage to Melanoma Cells. *Anal. Chem.* **2018**, *90* (6), 3666–3669.

(97) Zhang, L.; Huang, Z.; Dai, D.; Xiao, Y.; Lei, K.; Tan, S.; Cheng, J.; Xu, Y.; Liu, J.; Qian, X. Thio-Bisnaphthalimides as Heavy-Atom-Free Photosensitizers with Efficient Singlet Oxygen Generation and Large Stokes Shifts: Synthesis and Properties. *Org. Lett.* **2016**, *18* (21), 5664–5667.

APPENDIX

Appendix A : NMR Spectra

Appendix B : Mass Spectra

Appendix A: NMR Spectra

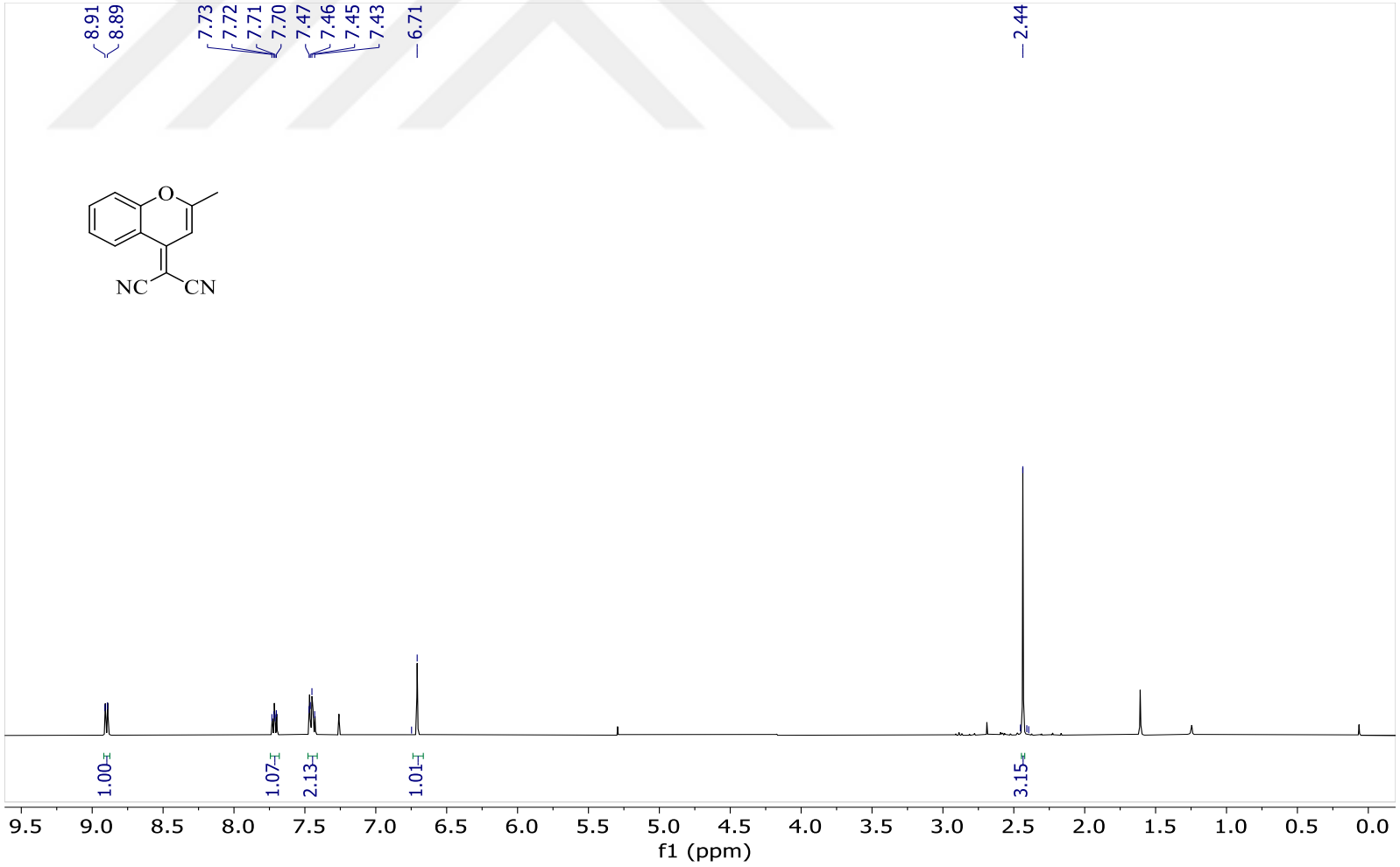

^{1}H NMR of Compound **3** in $CDCl_3$

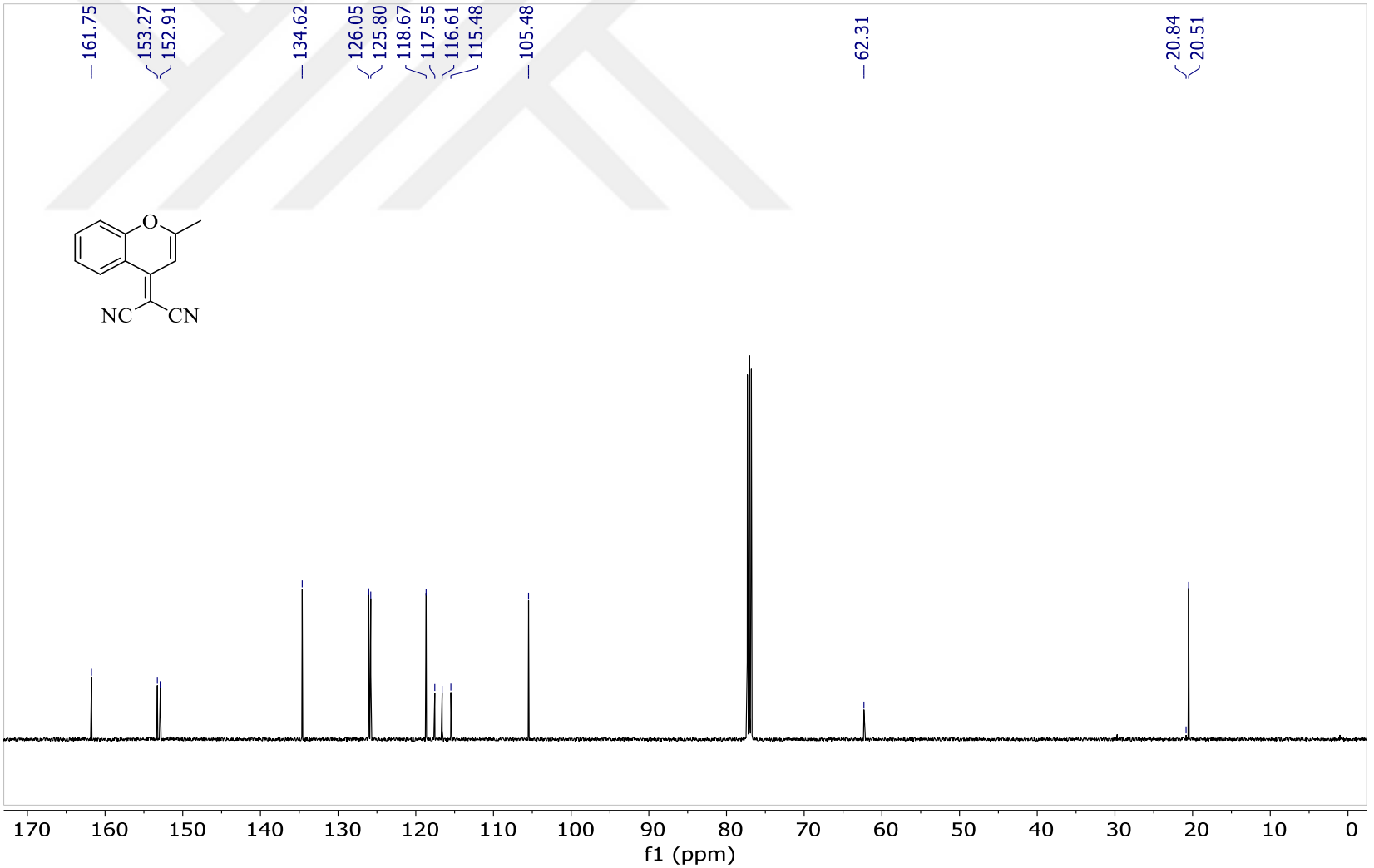

^{13}C NMR of Compound **3** in $CDCl_3$

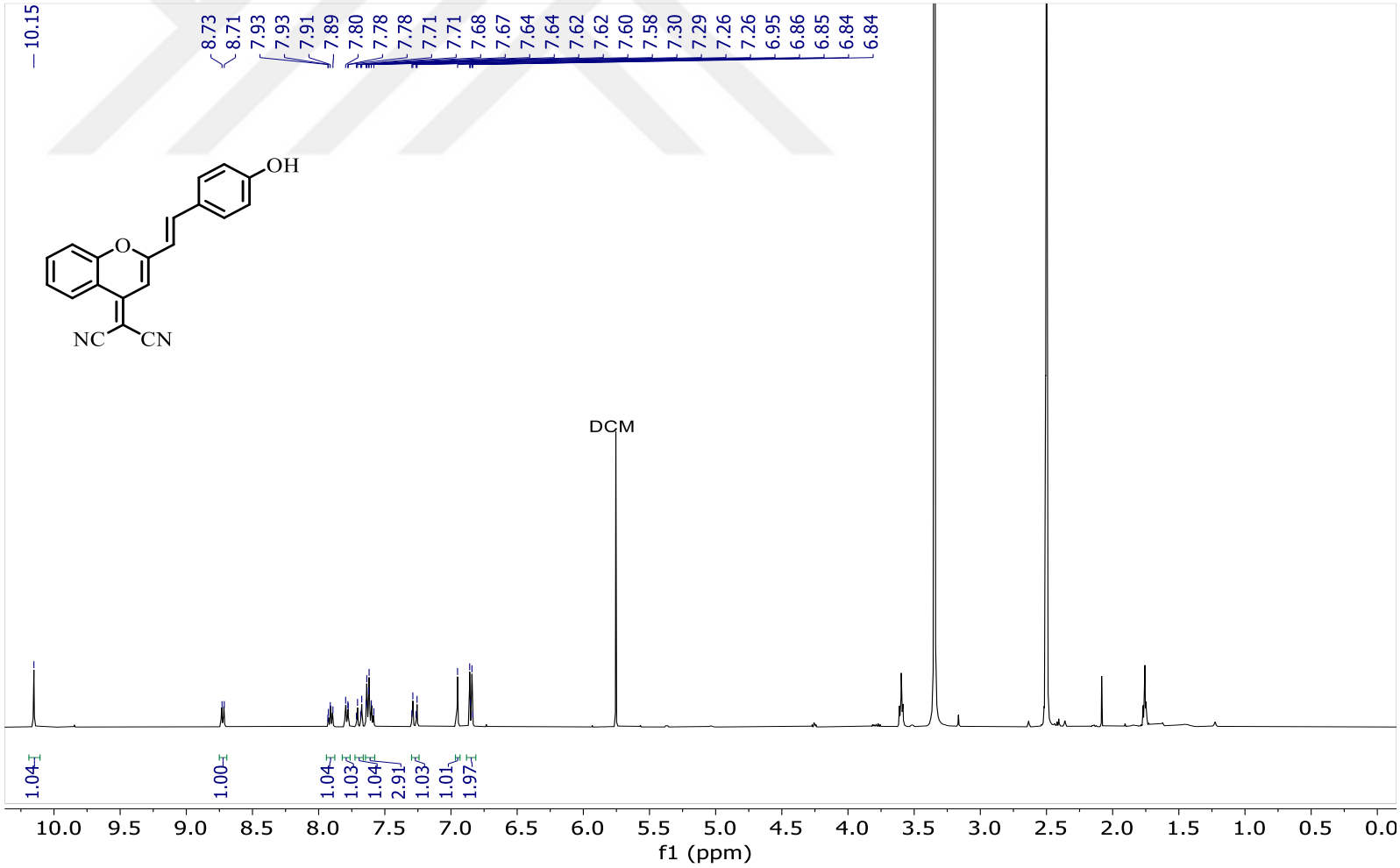

^{1}H NMR of **DCM$_{O}$** in d_6-DMSO

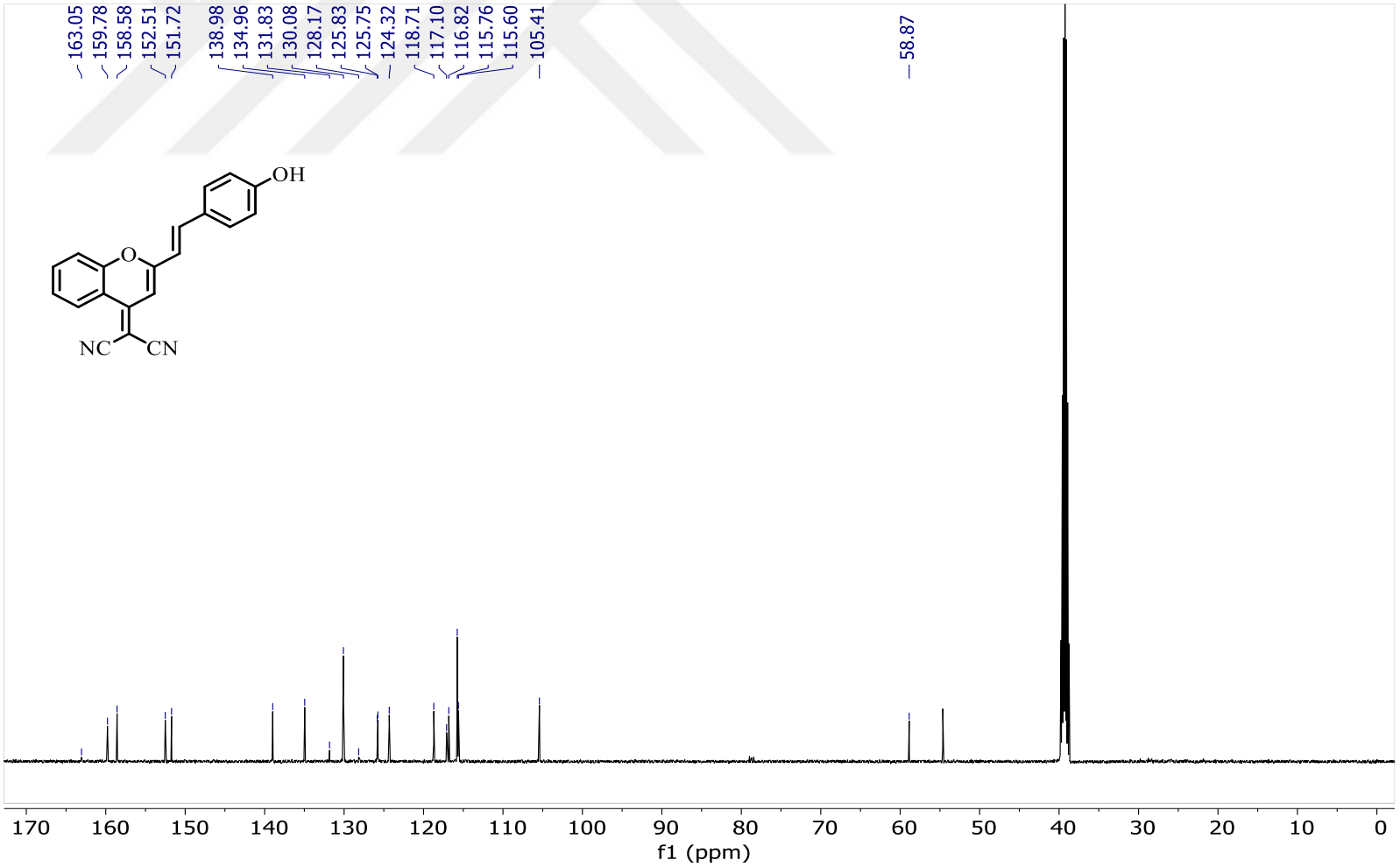

^{13}C NMR of **DCM$_O$** in d_6-DMSO

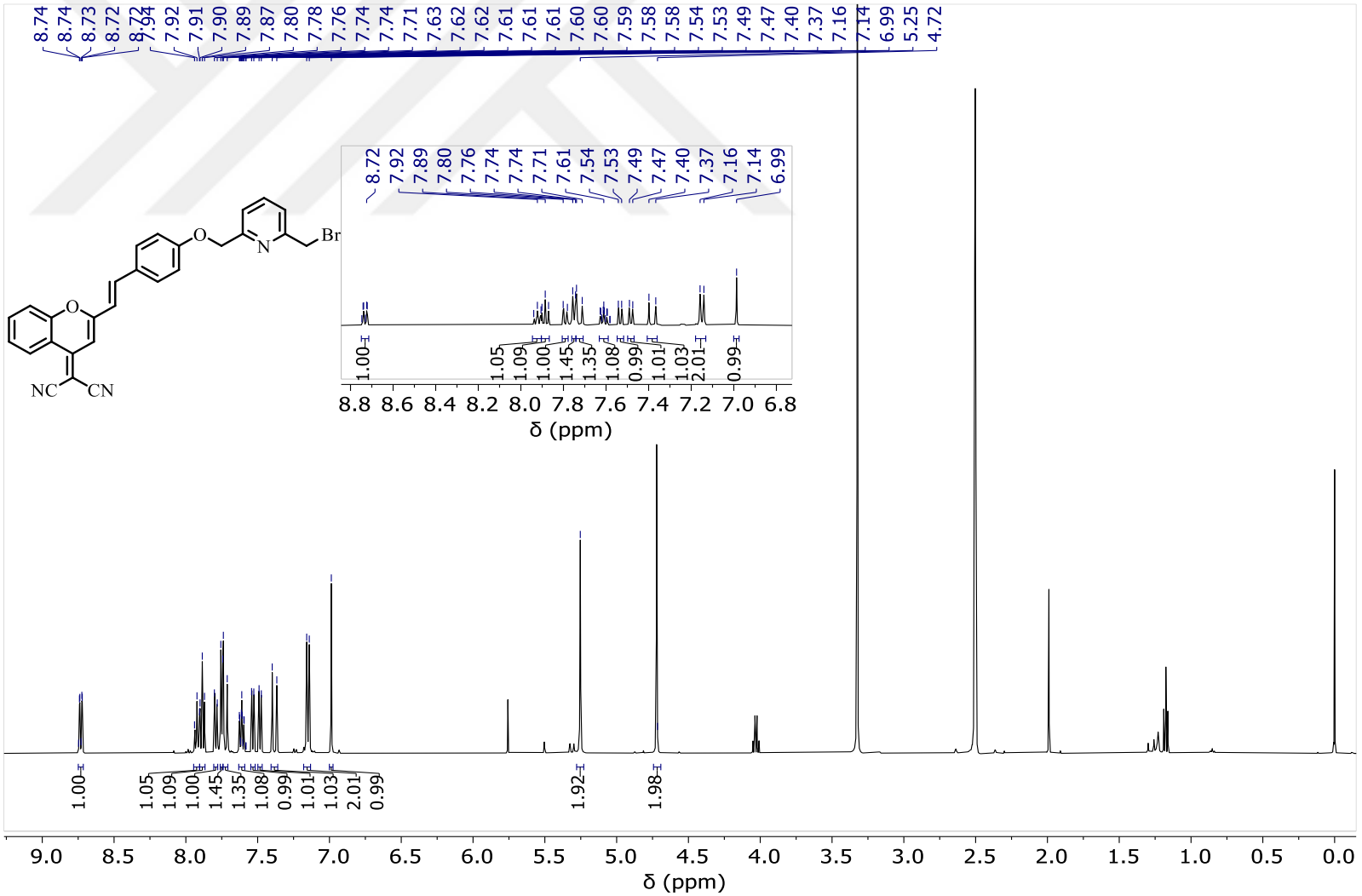

^{1}H NMR of Compound **4** in d_6-DMSO

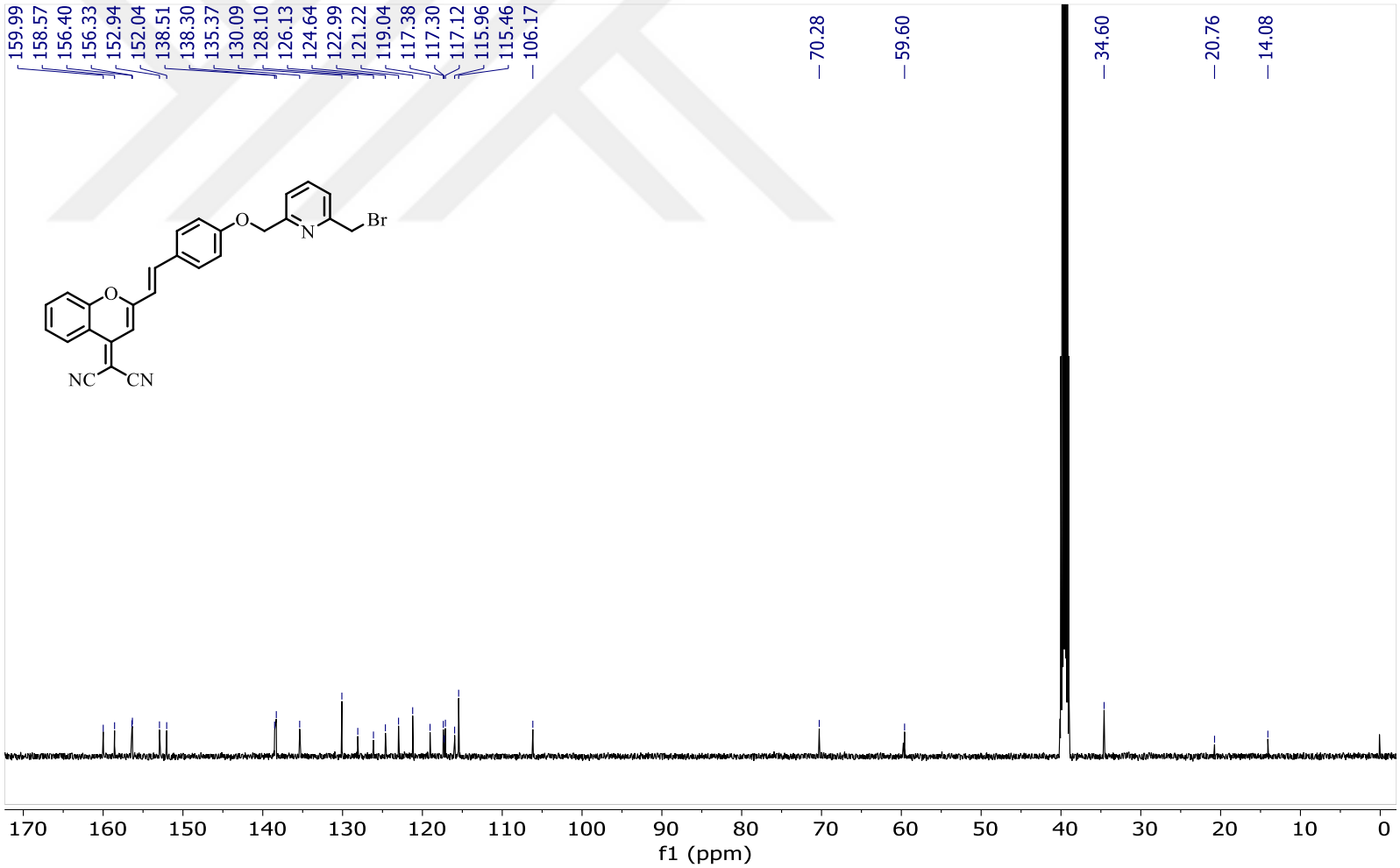

^{13}C NMR of Compound **4** in d_6-DMSO

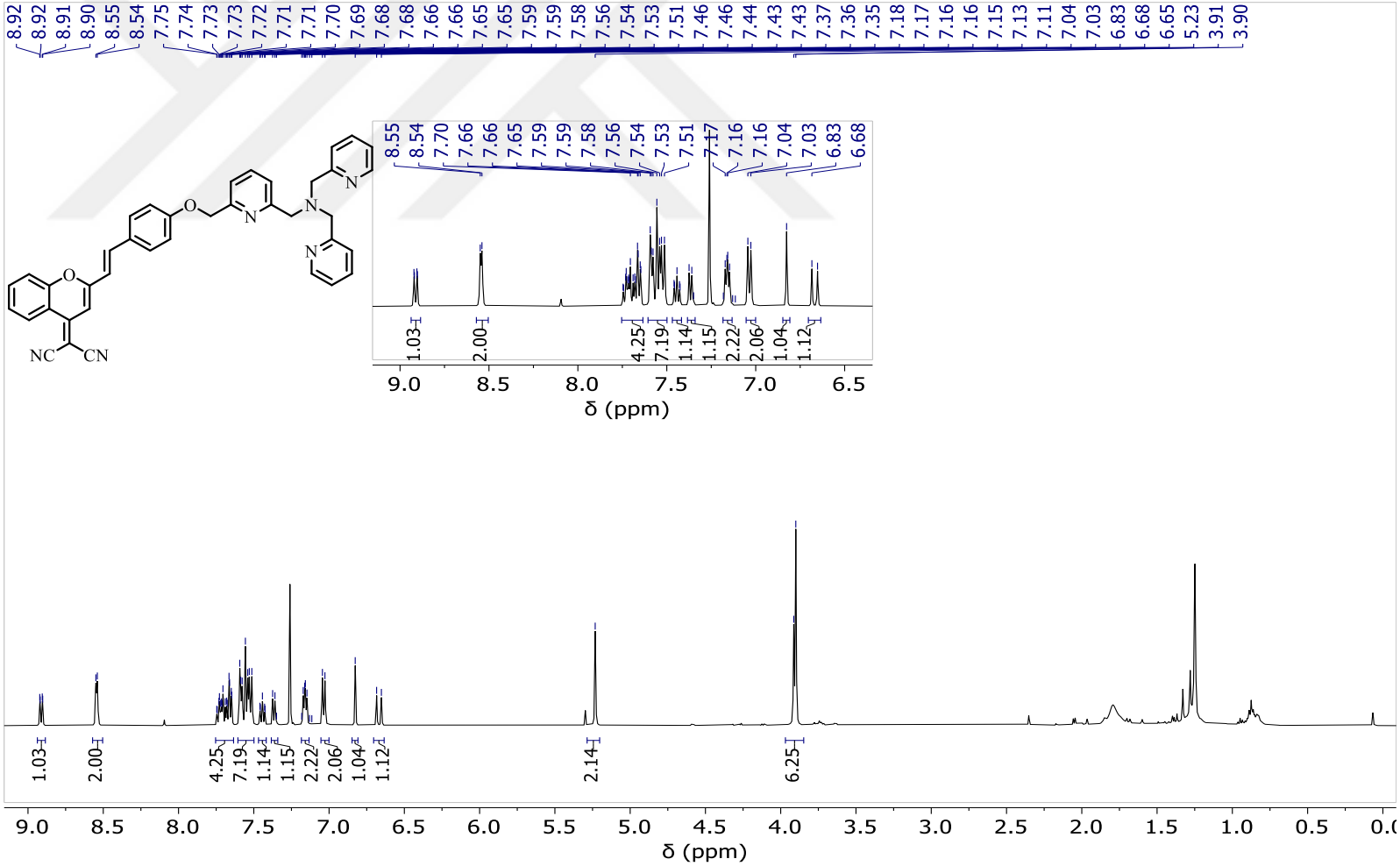

^{1}H NMR of **DCM-Cu** in $CDCl_3$

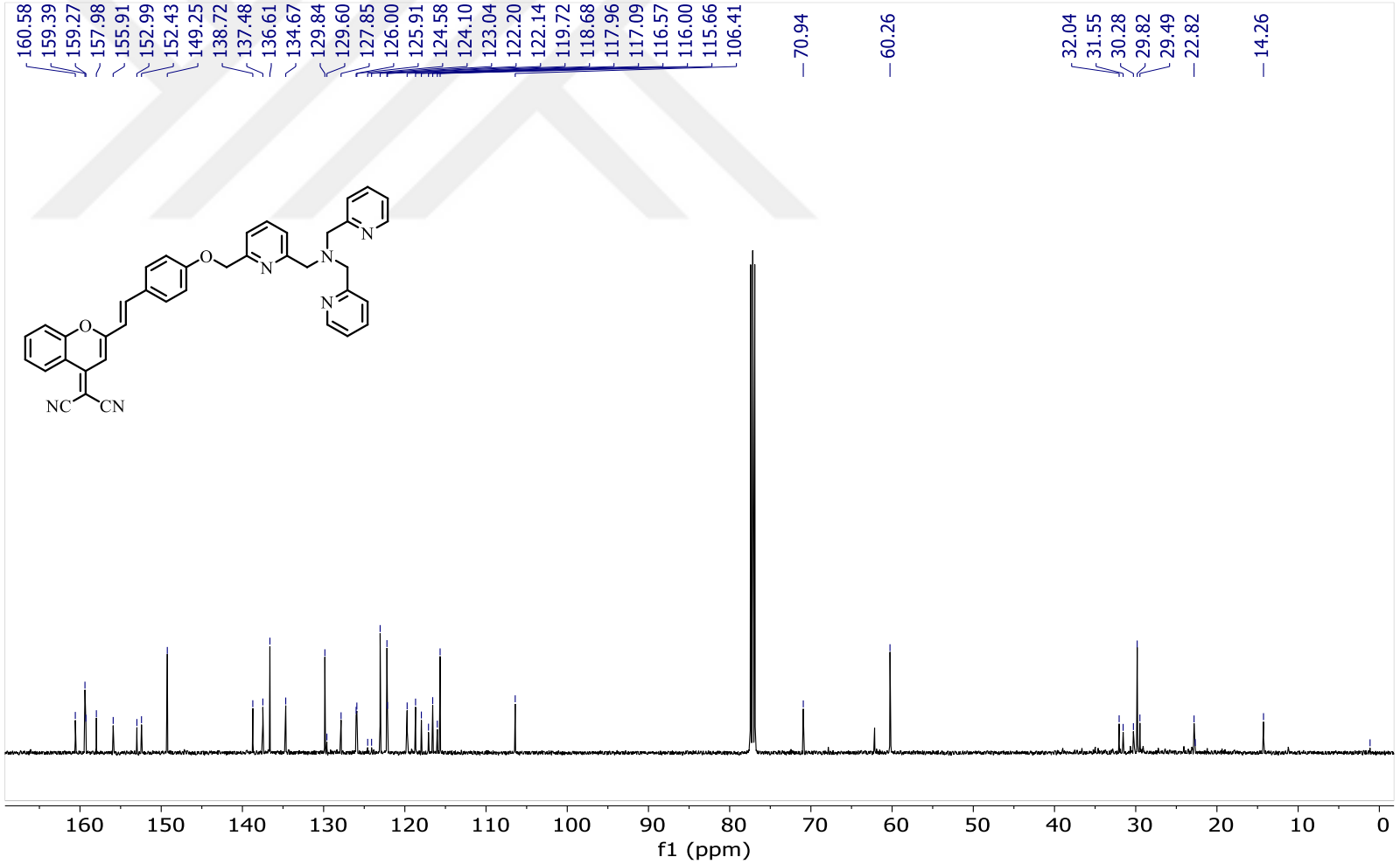

^{13}C NMR of **DCM-Cu** in $CDCl_3$

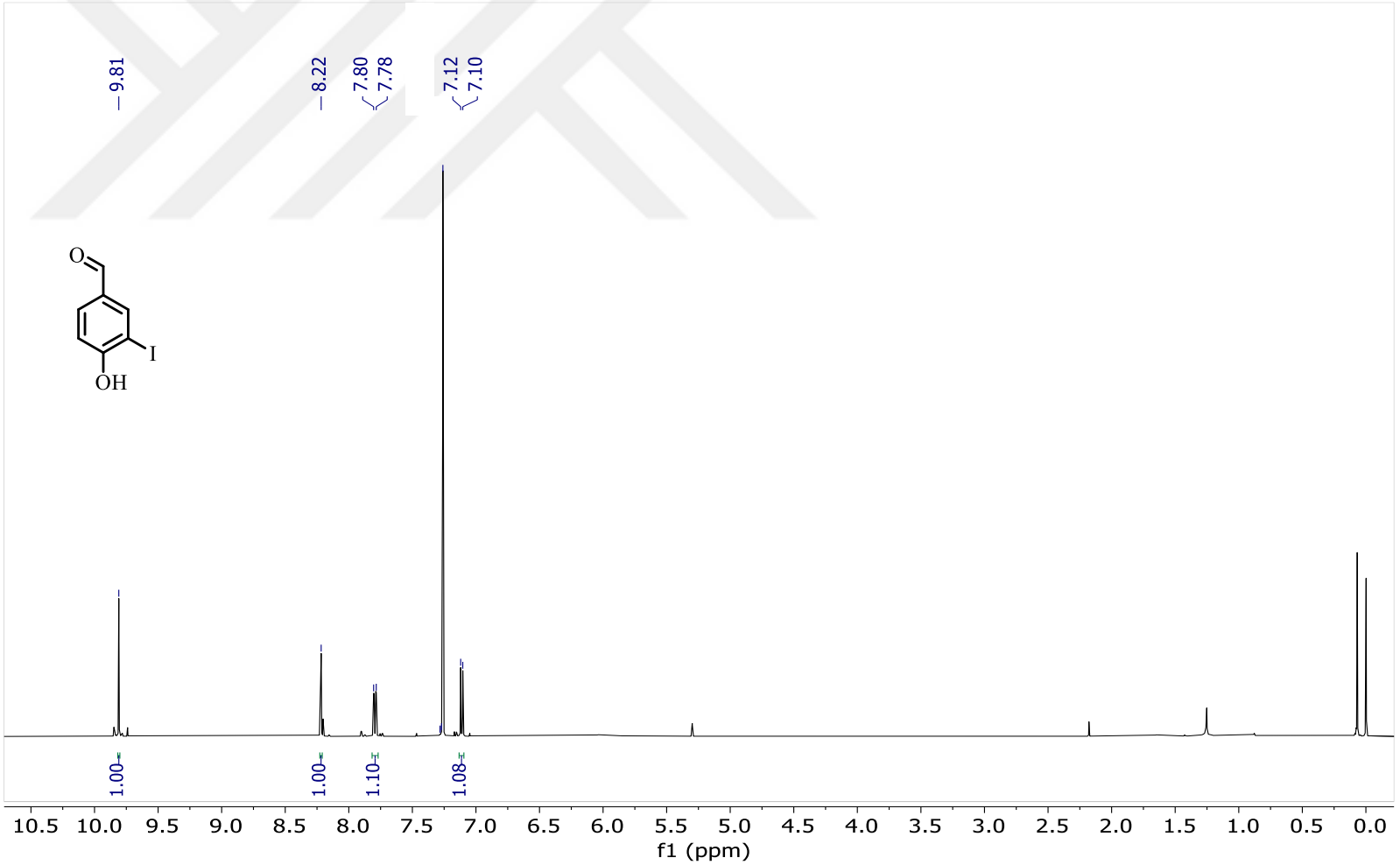

^{1}H NMR of **Compund 5** in $CDCl_3$

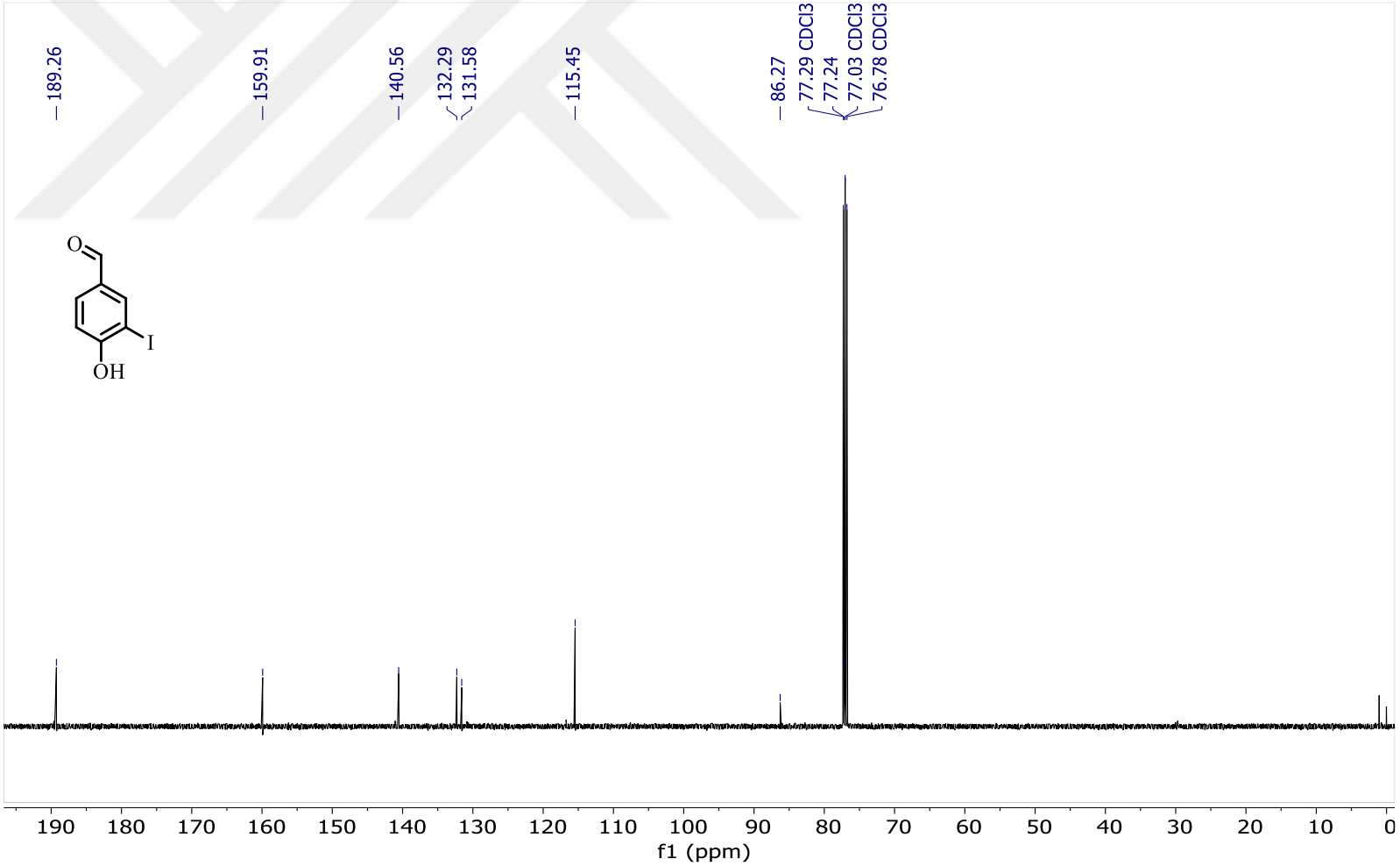

^{13}C NMR of **Compund 5** in $CDCl_3$

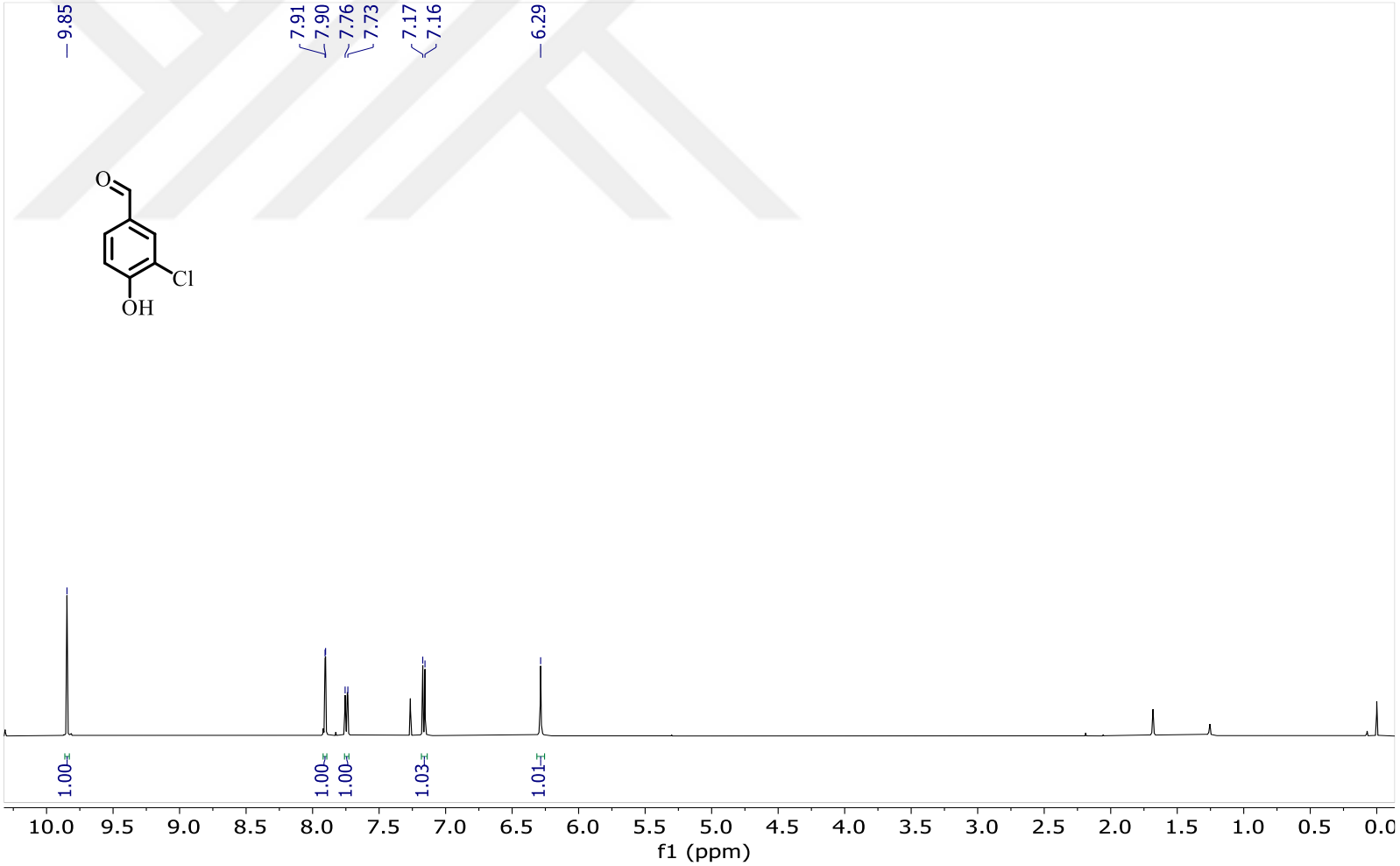

^{1}H NMR of **Compund 6** in $CDCl_3$

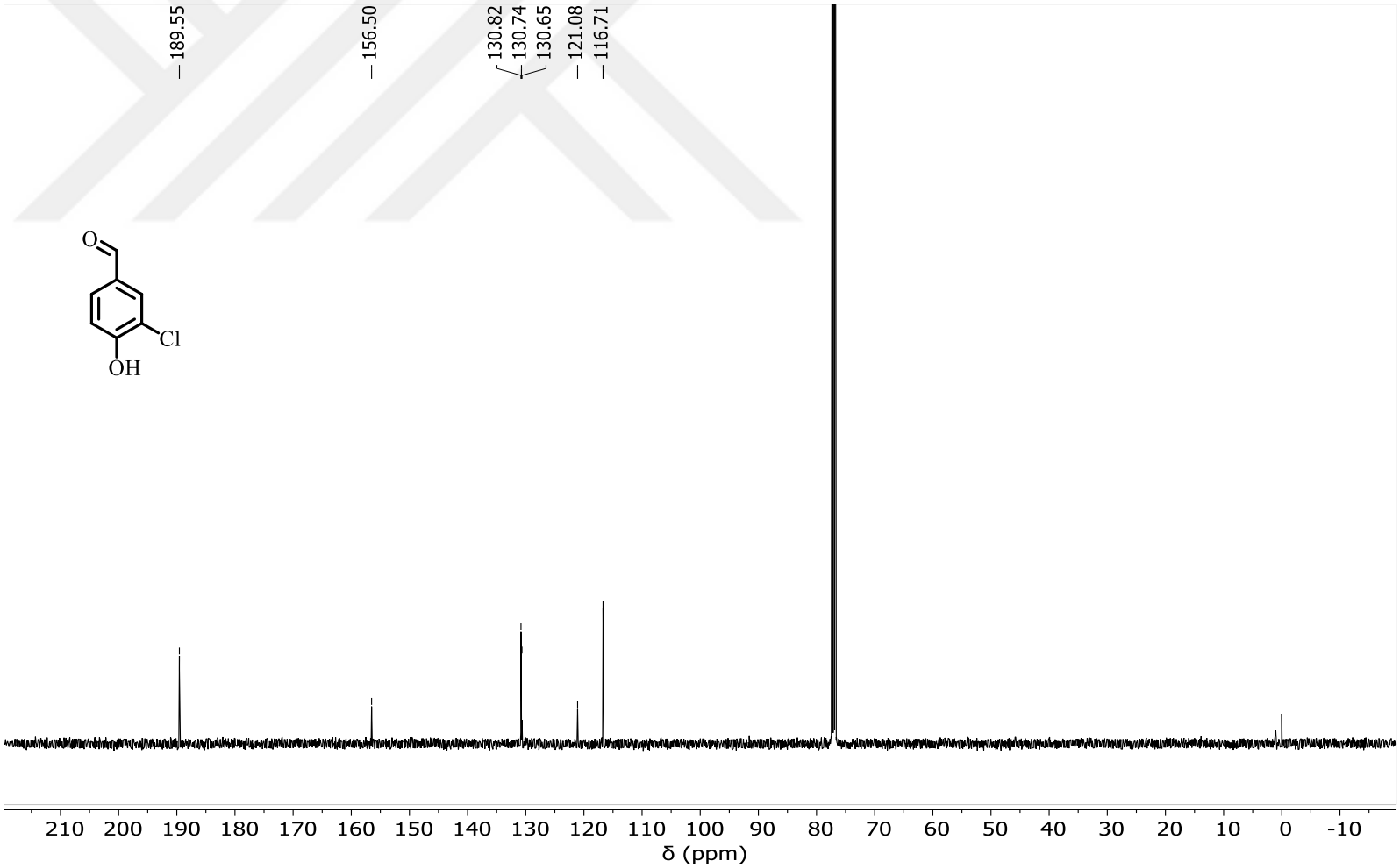

^{13}C NMR of **Compund 6** in $CDCl_3$

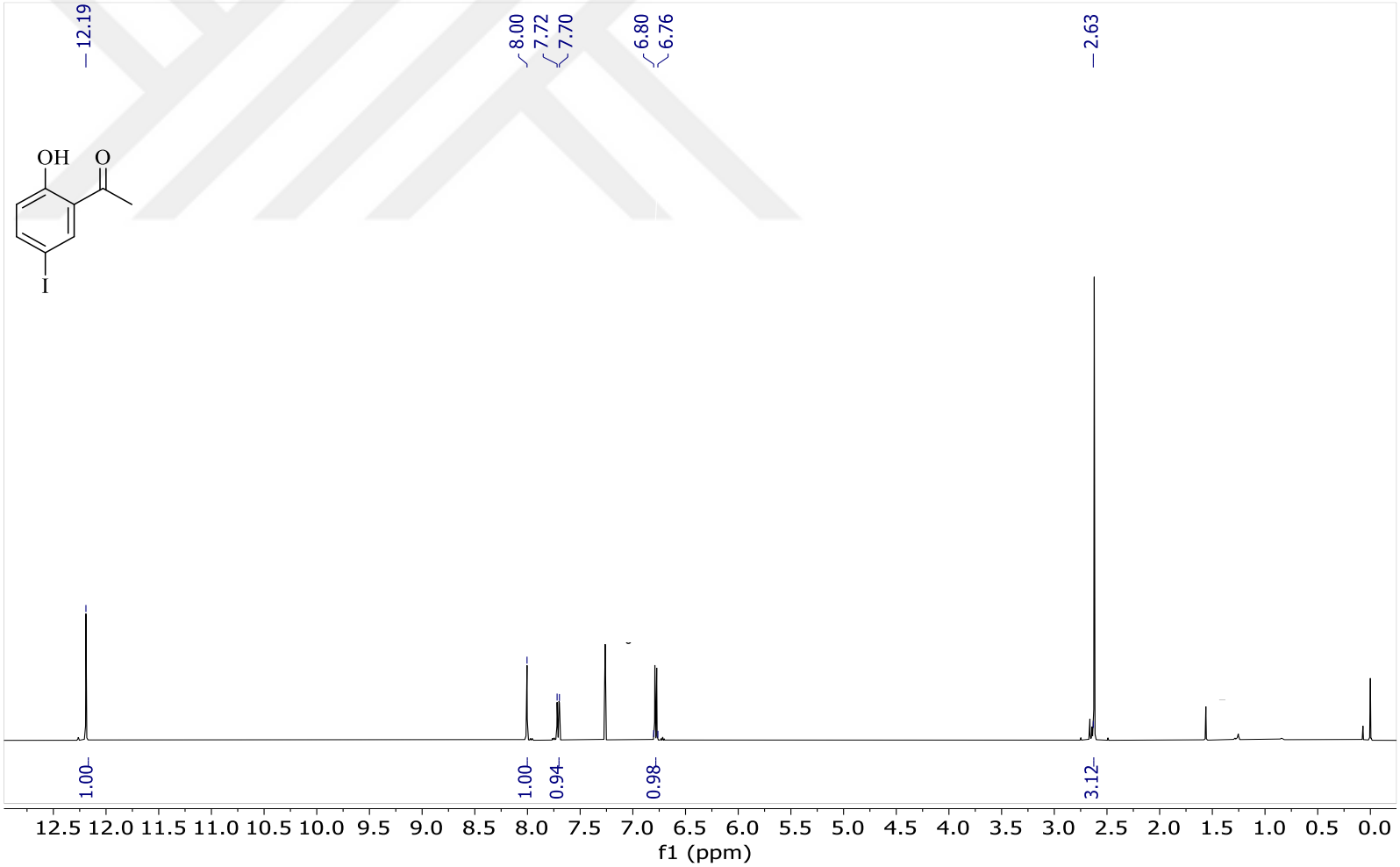

^{1}H NMR of **Compund 7** in $CDCl_3$

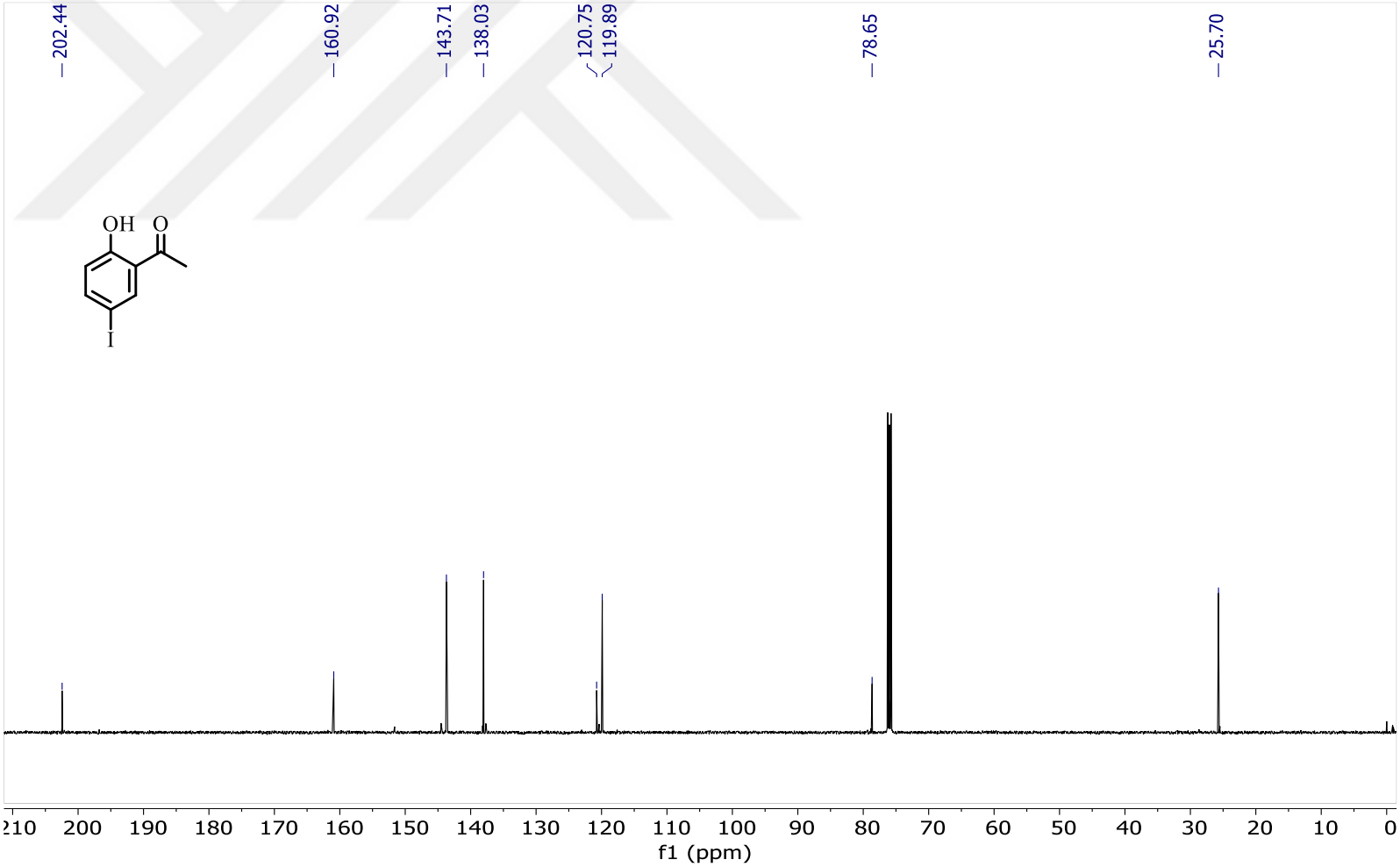

^{13}C NMR of **Compund 7** in $CDCl_3$

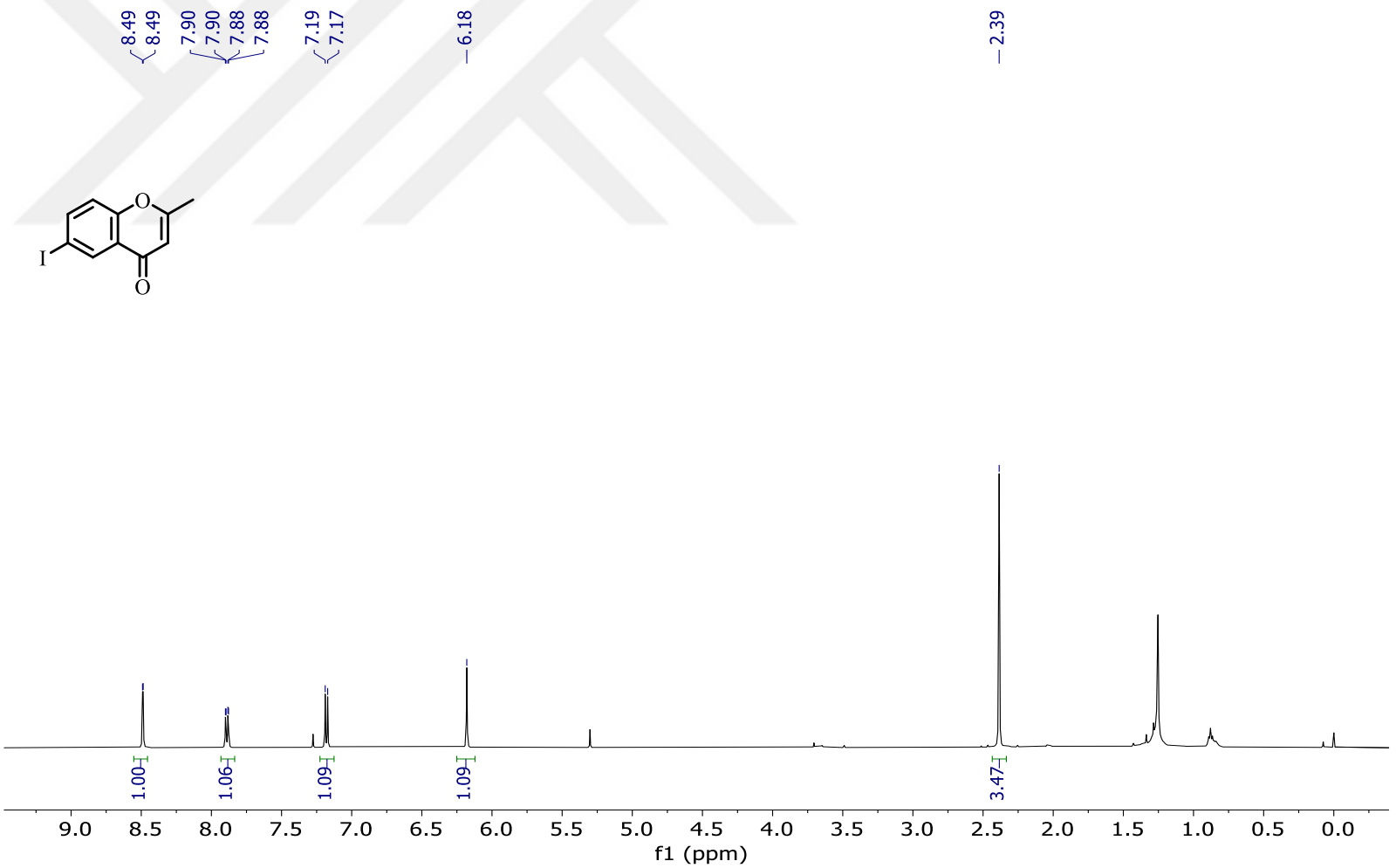

^{1}H NMR of **Compund 8** in $CDCl_3$

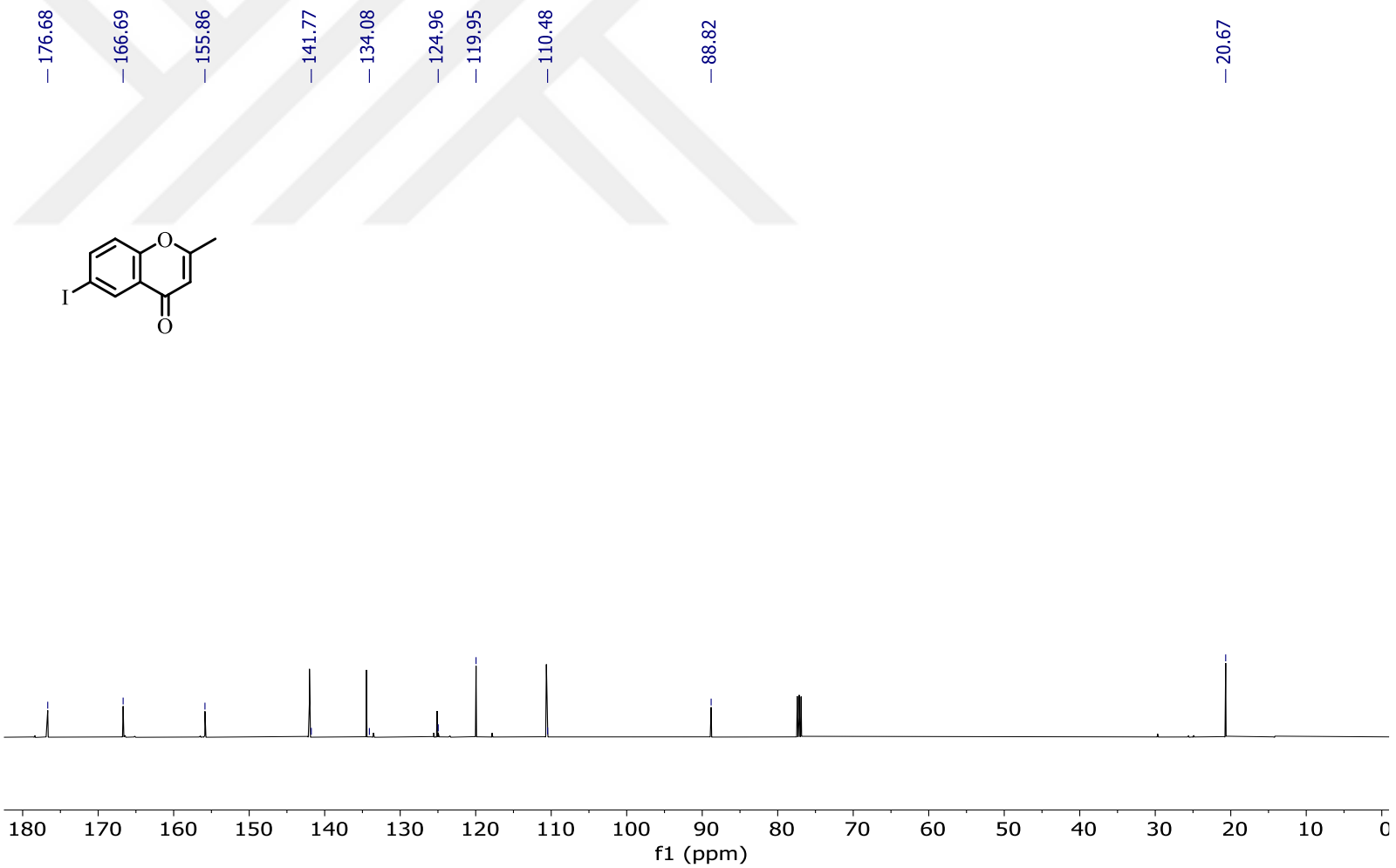

^{13}C NMR of **Compund 8** in $CDCl_3$

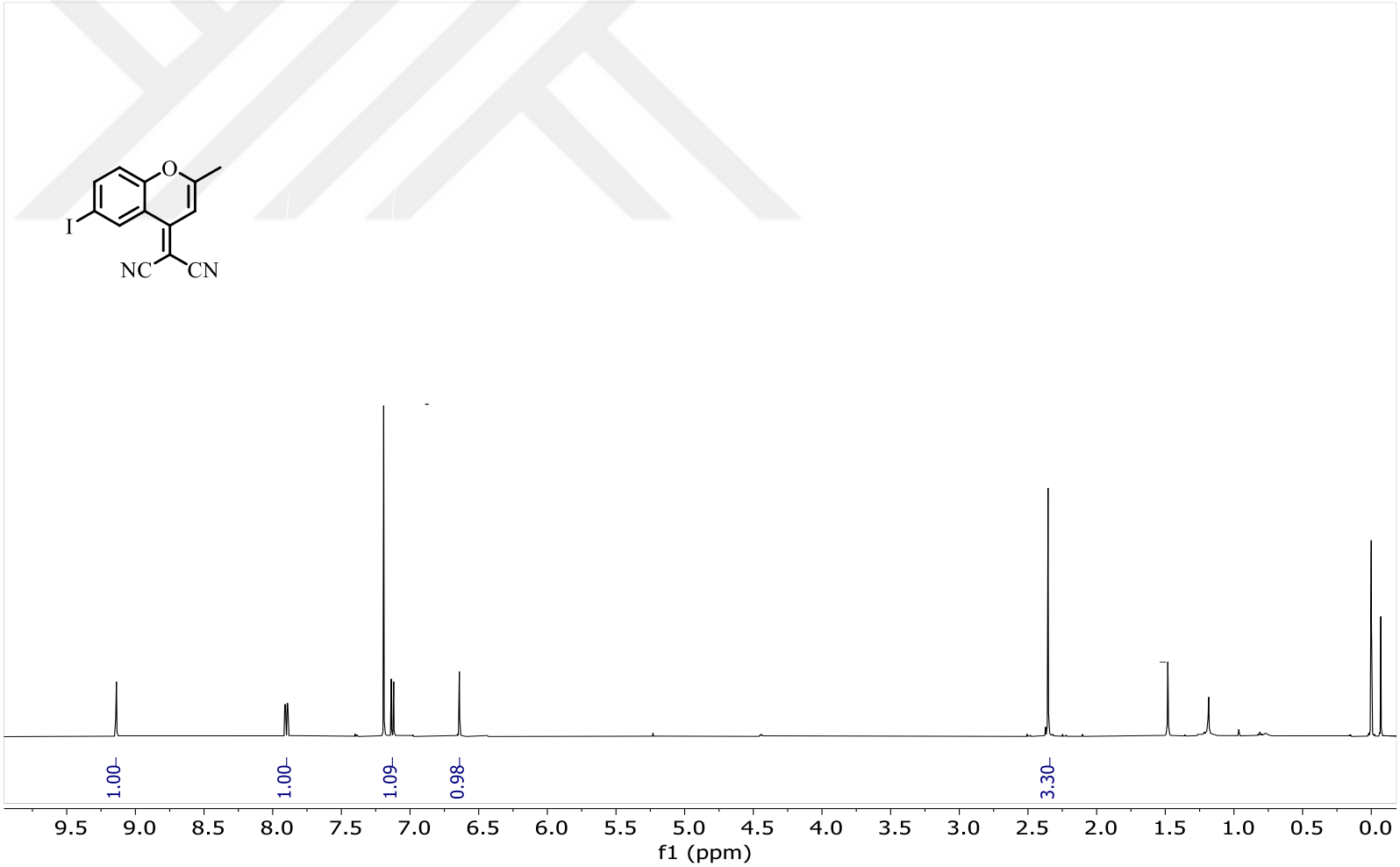

^{1}H NMR of **Compund 9** in $CDCl_3$

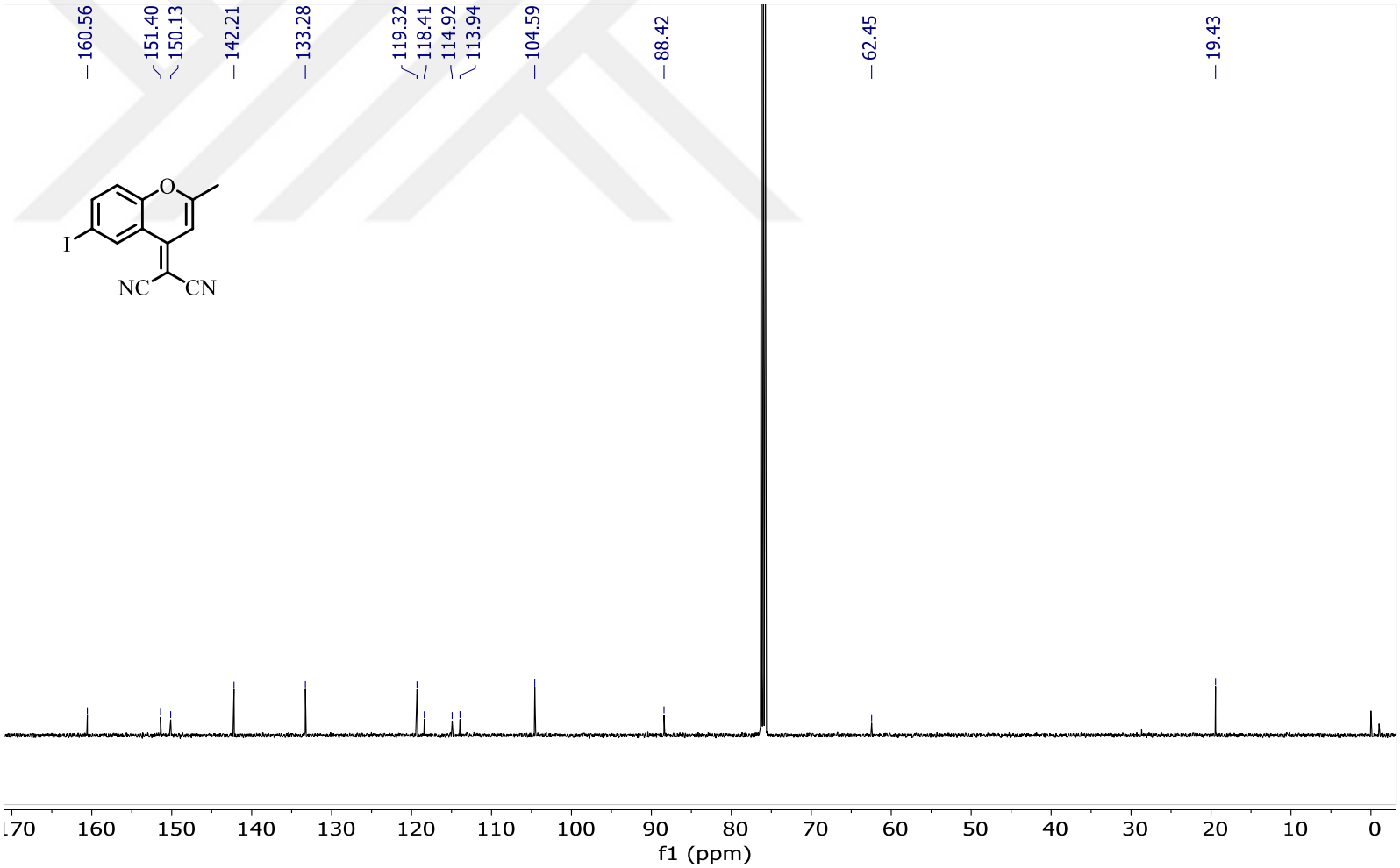

^{13}C NMR of **Compund 9** in $CDCl_3$

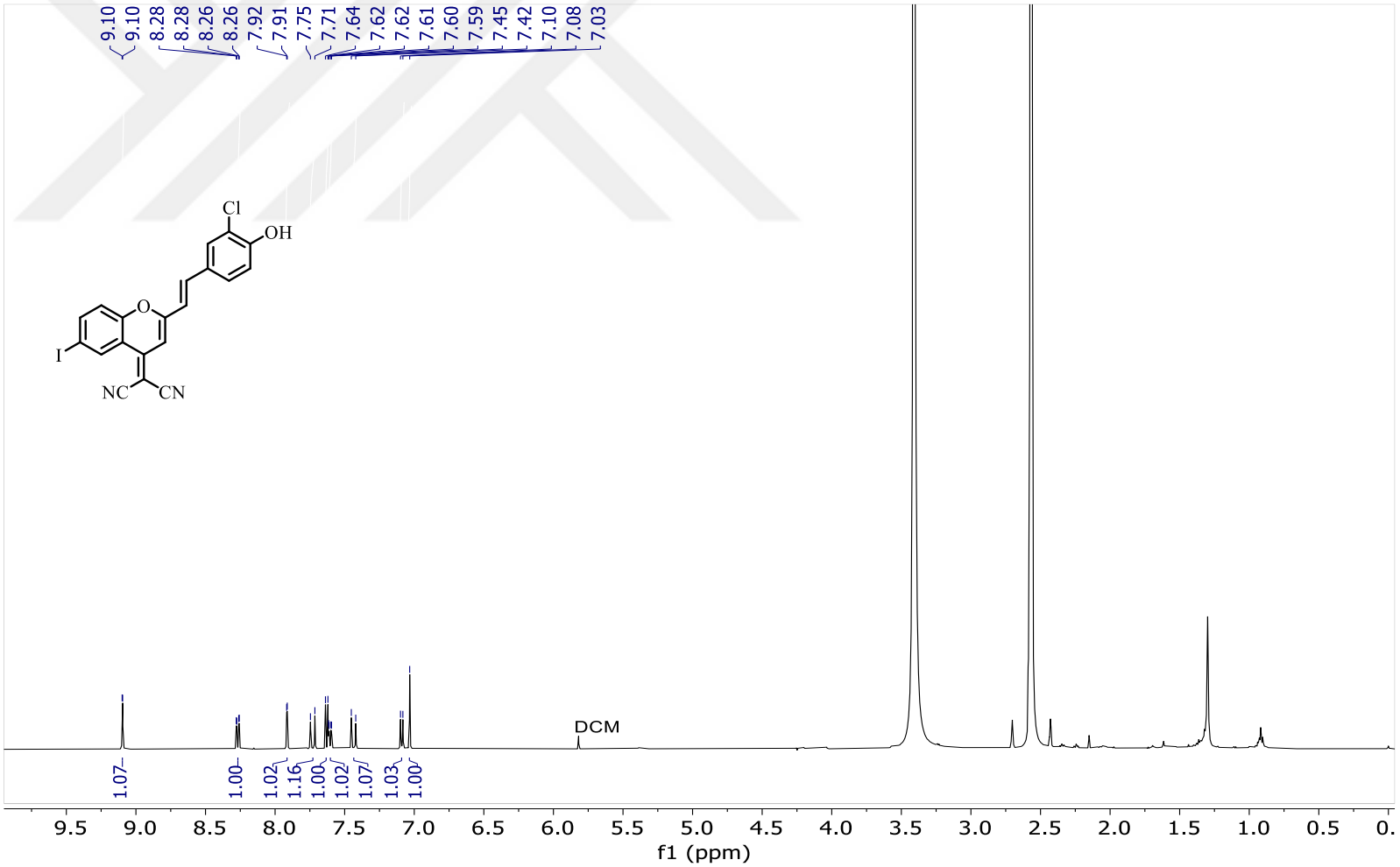

^{1}H NMR of **I-DCM$_{O}$-Cl** in d_6-DMSO

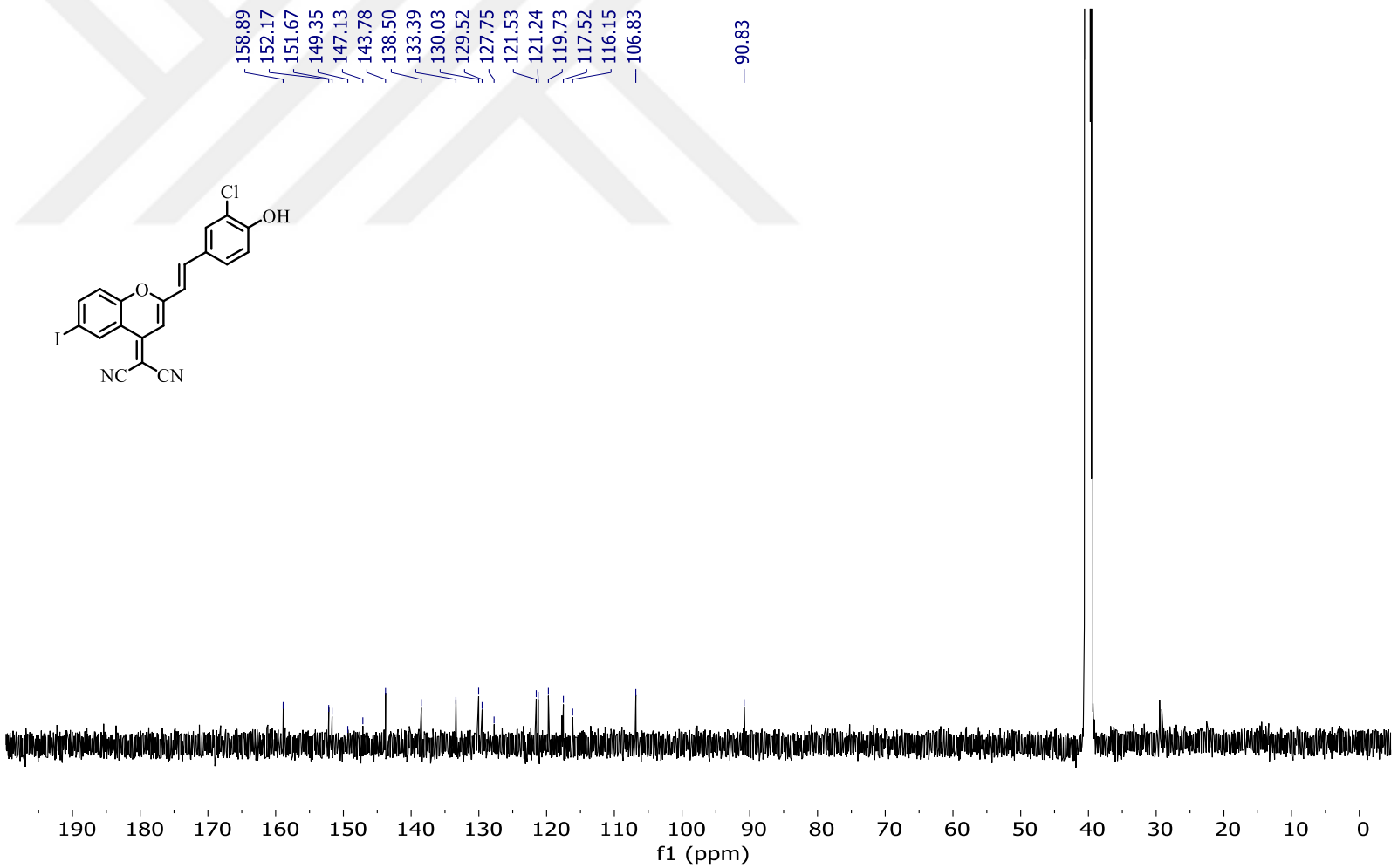

^{13}C NMR of **I-DCM$_O$-Cl** in d_6-DMSO

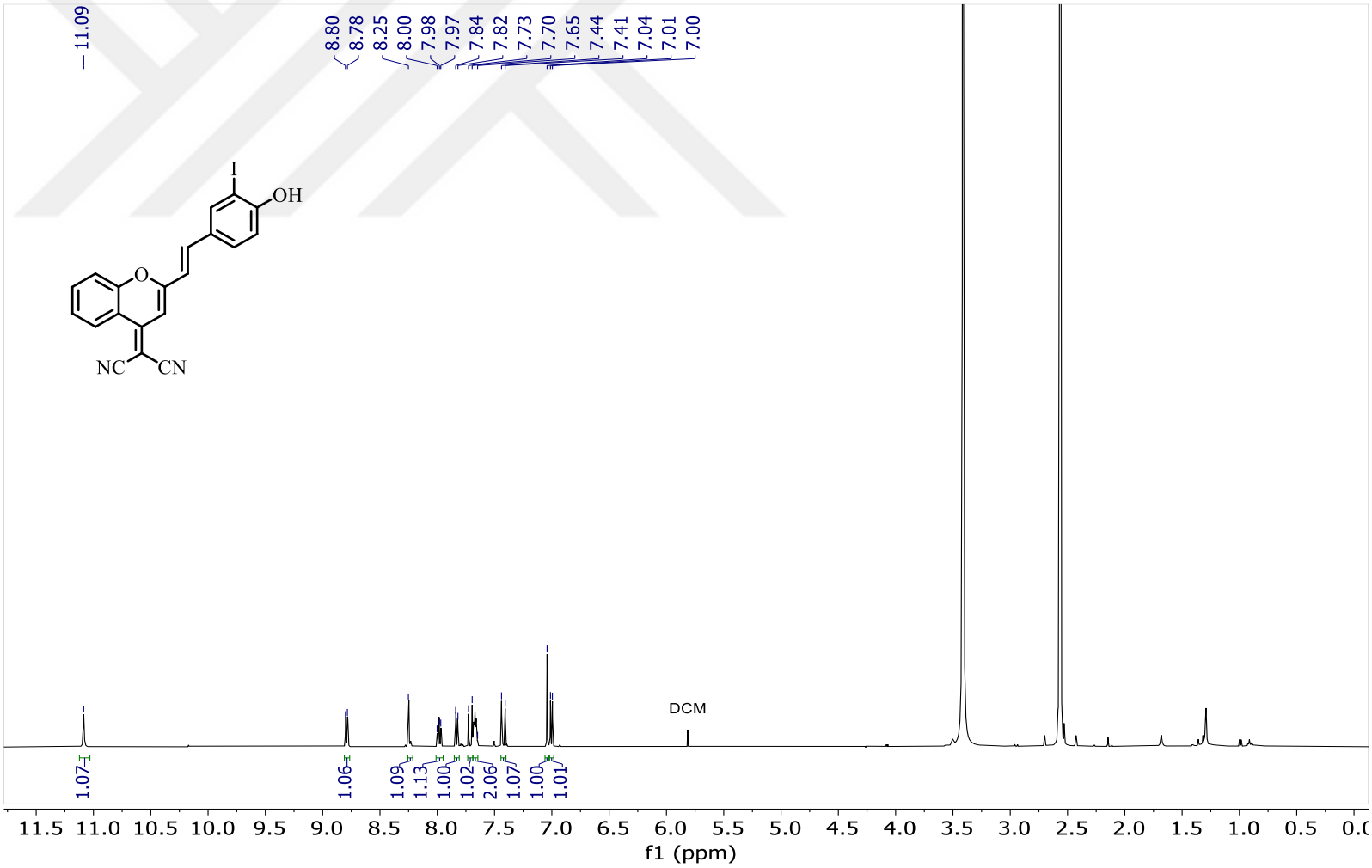

^{1}H NMR of **DCM$_{O}$-I** in d_6-DMSO

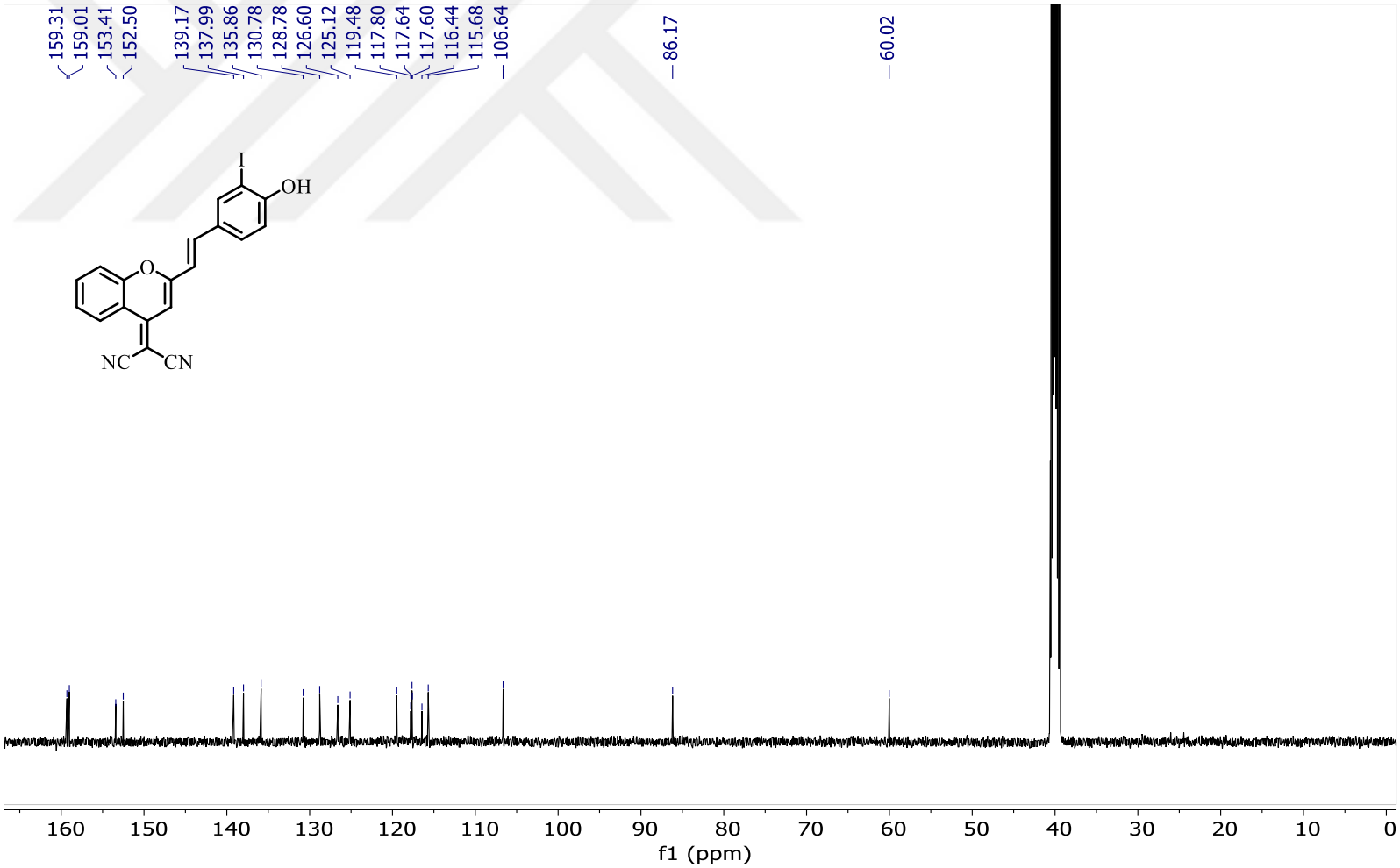

^{13}C NMR of **DCM$_{O}$-I** in d_6-DMSO

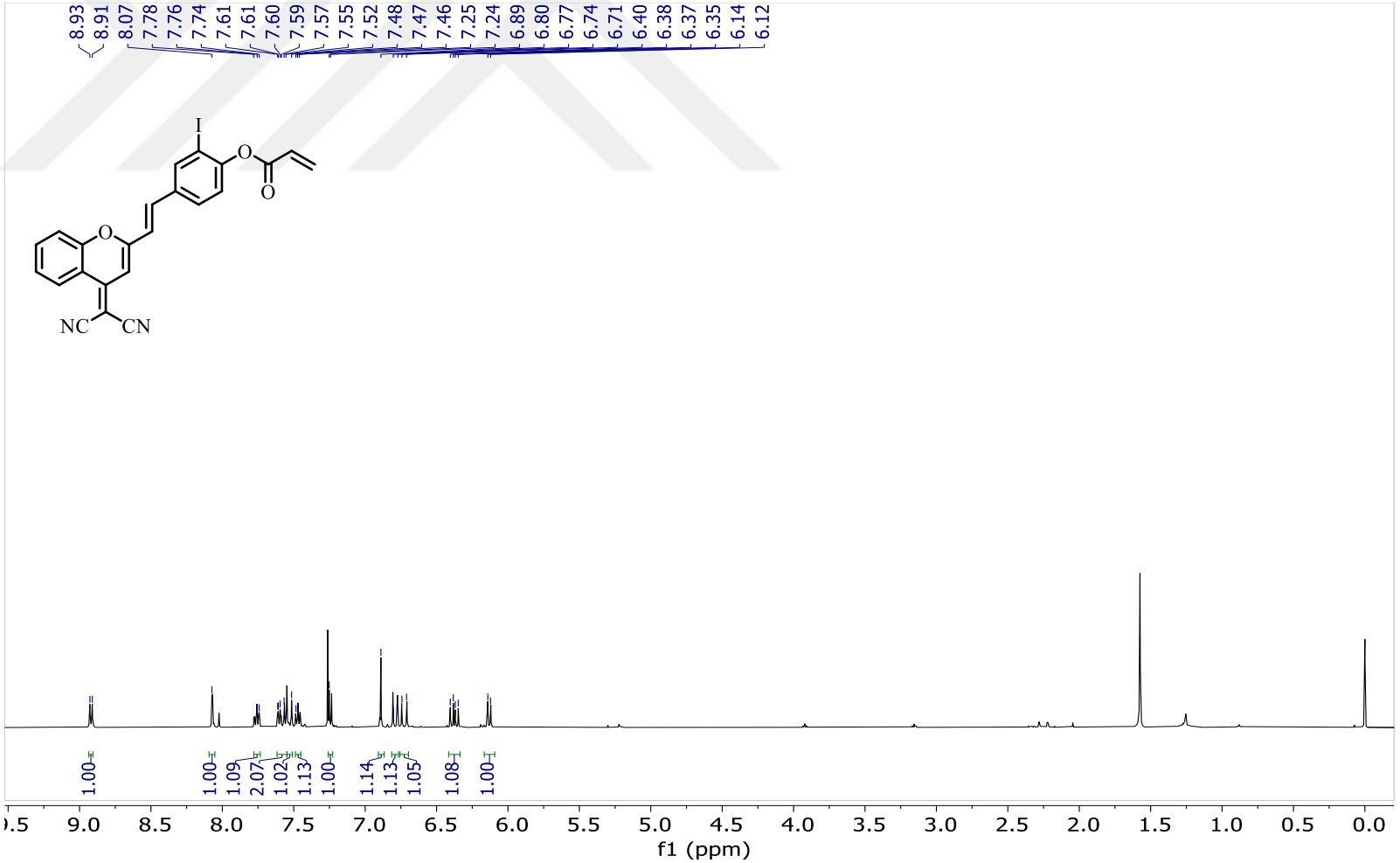

^{1}H NMR of **DCM$_{O}$-I-Cys** in $CDCl_3$

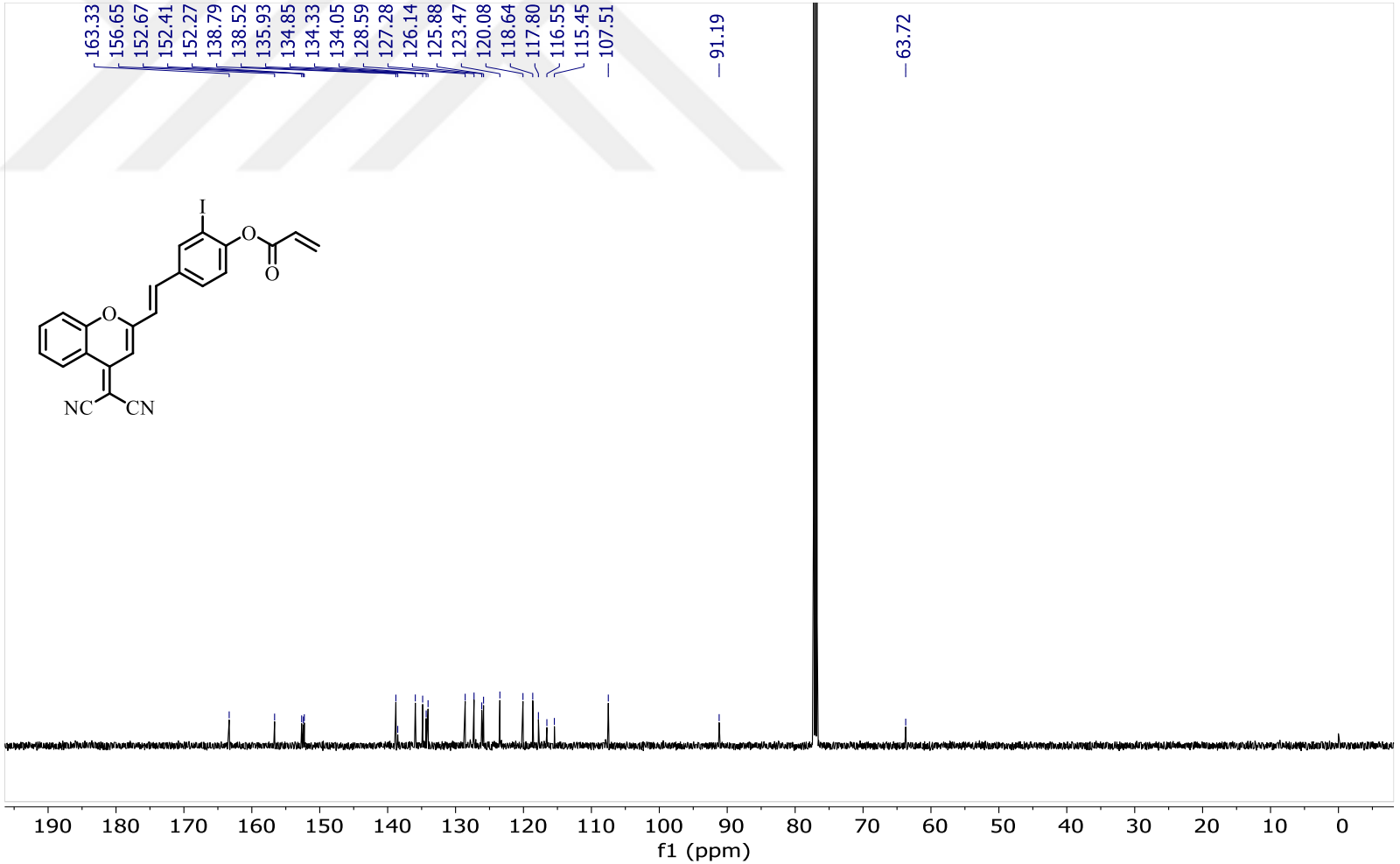

^{13}C NMR of **DCM$_{O}$-I-Cys** in $CDCl_3$

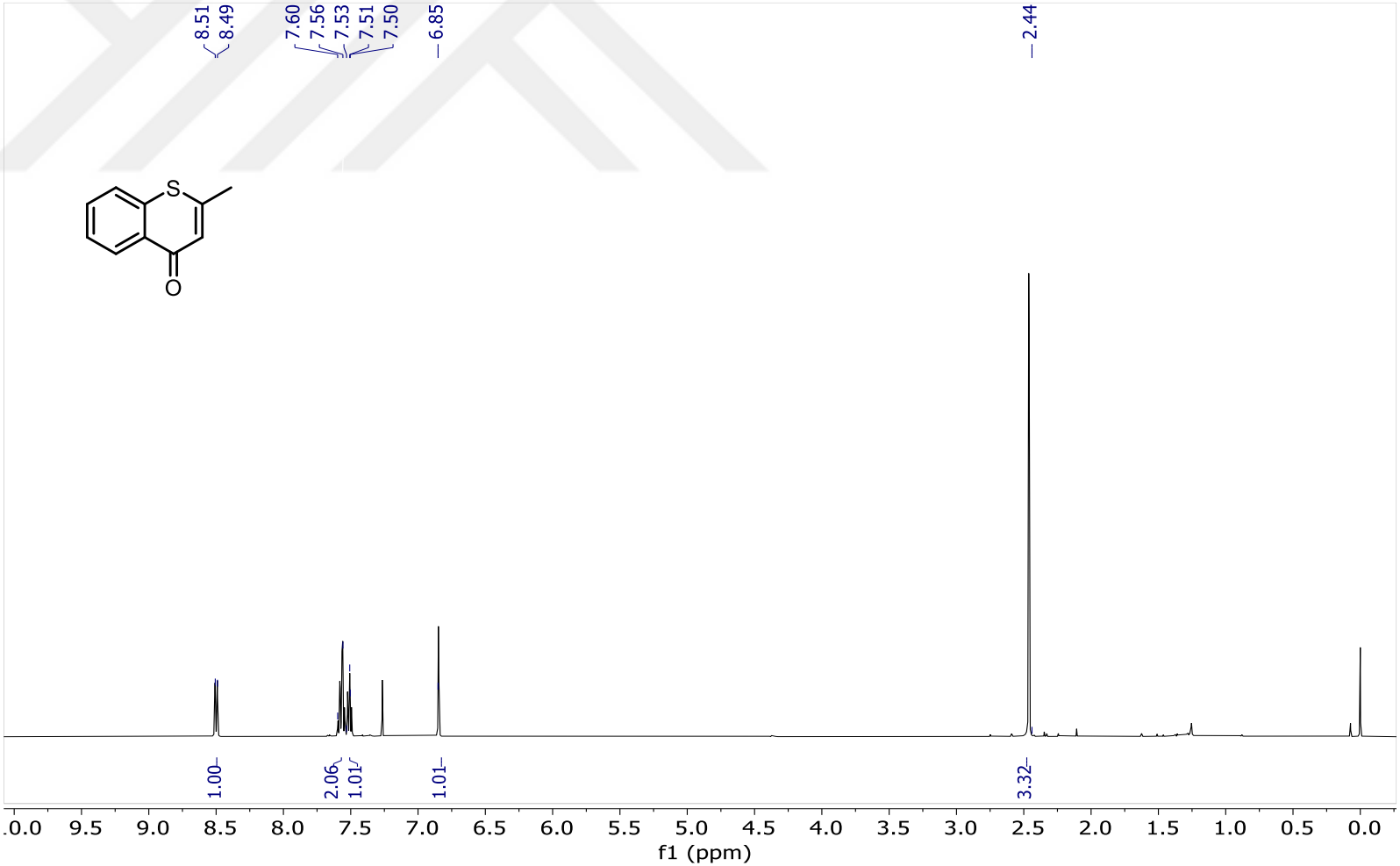

^{1}H NMR of **Compound 10** in $CDCl_3$

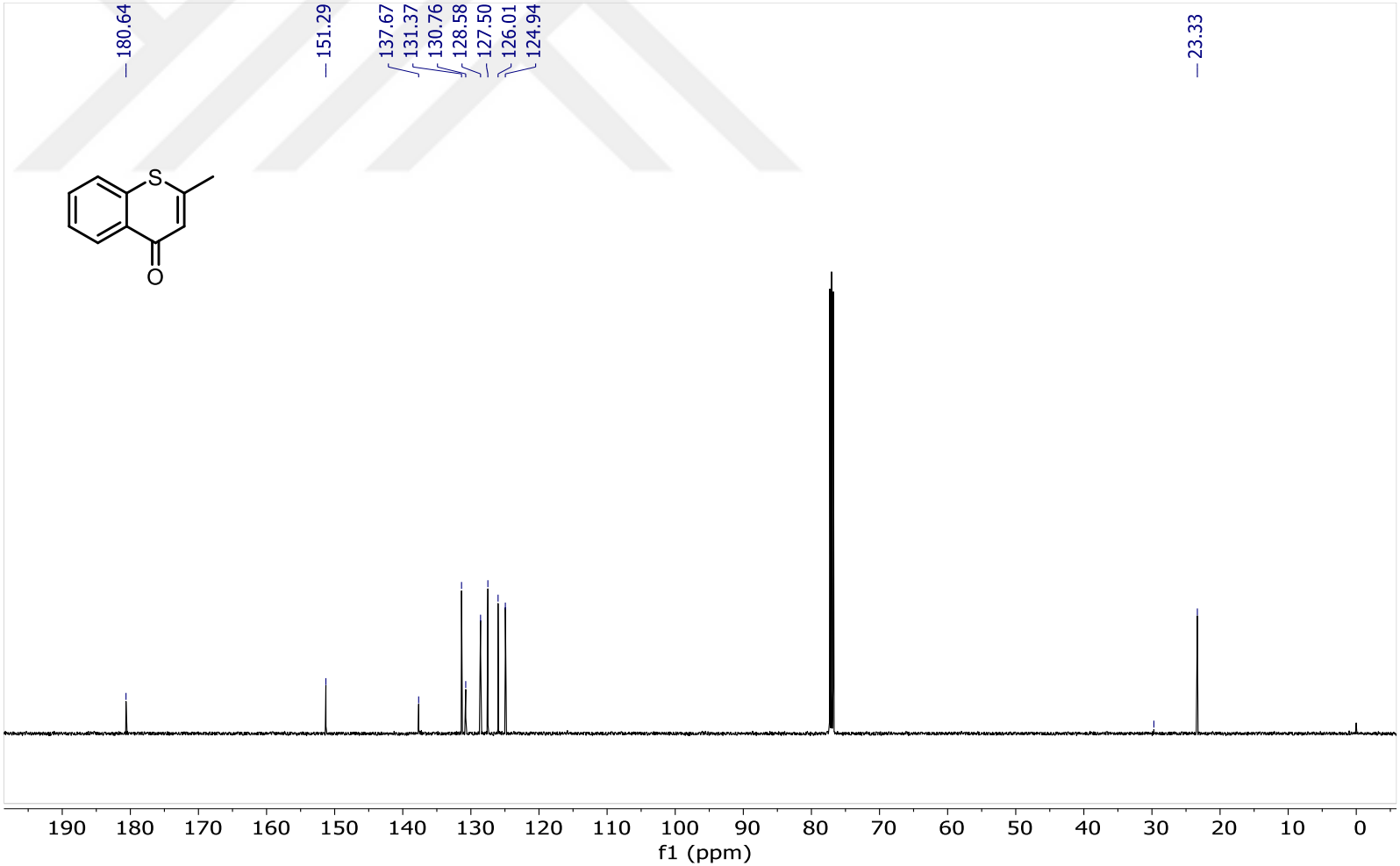

^{13}C NMR of **Compound 10** in $CDCl_3$

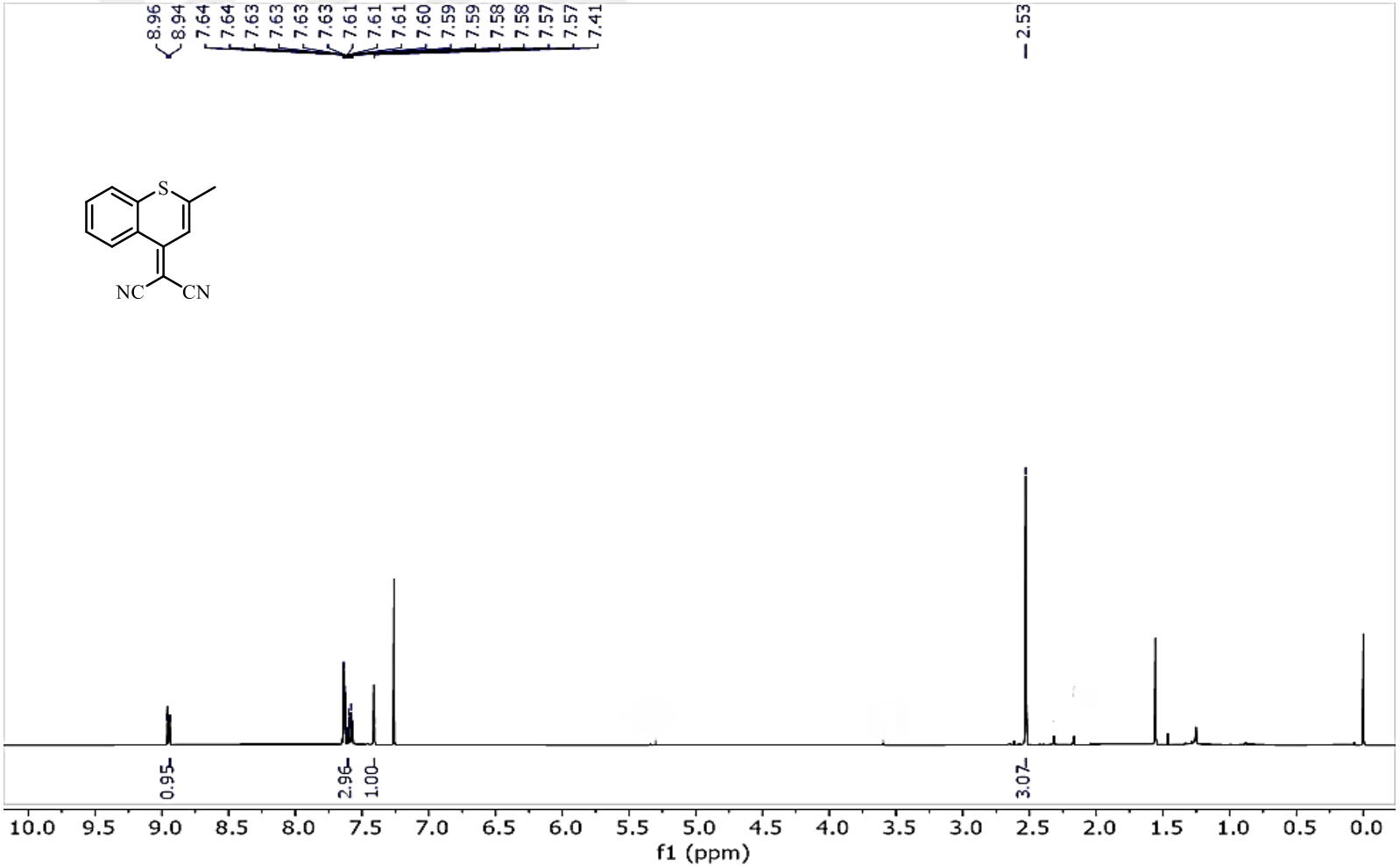

^{1}H NMR of **Compound 11** in $CDCl_3$

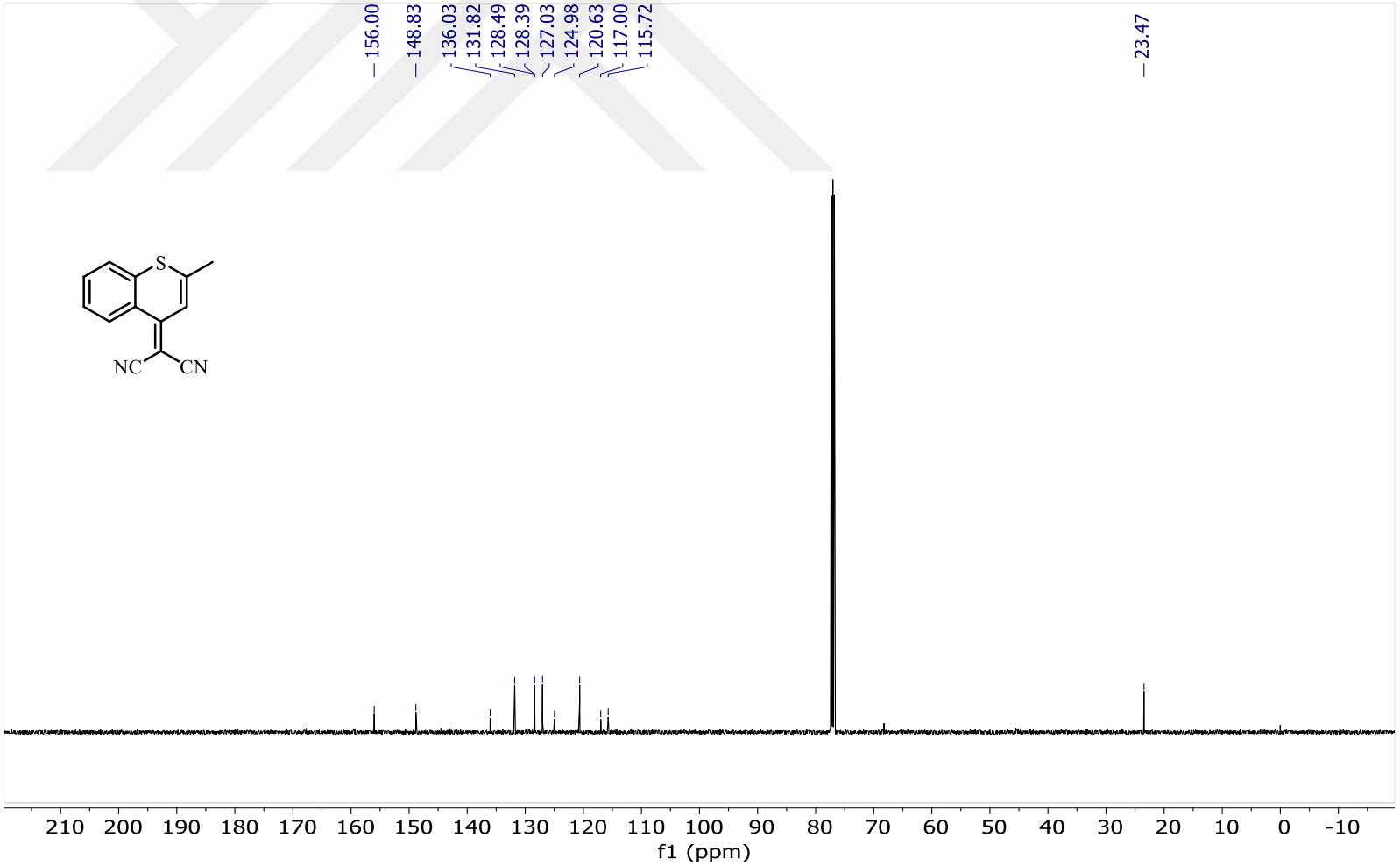

^{13}C NMR of **Compound 11** in $CDCl_3$

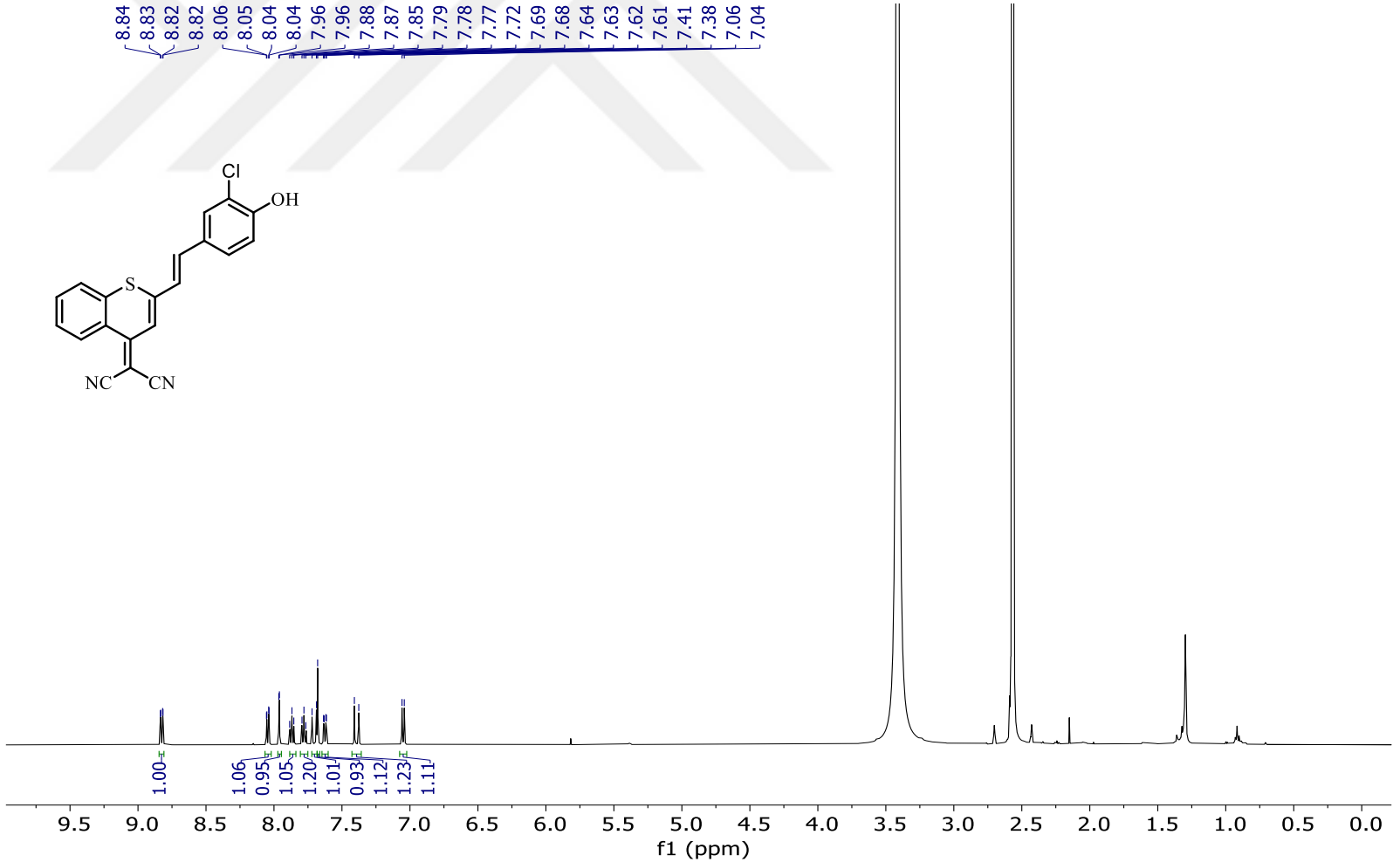

^{1}H NMR of **DCM$_{S}$-Cl** in d_6-DMSO

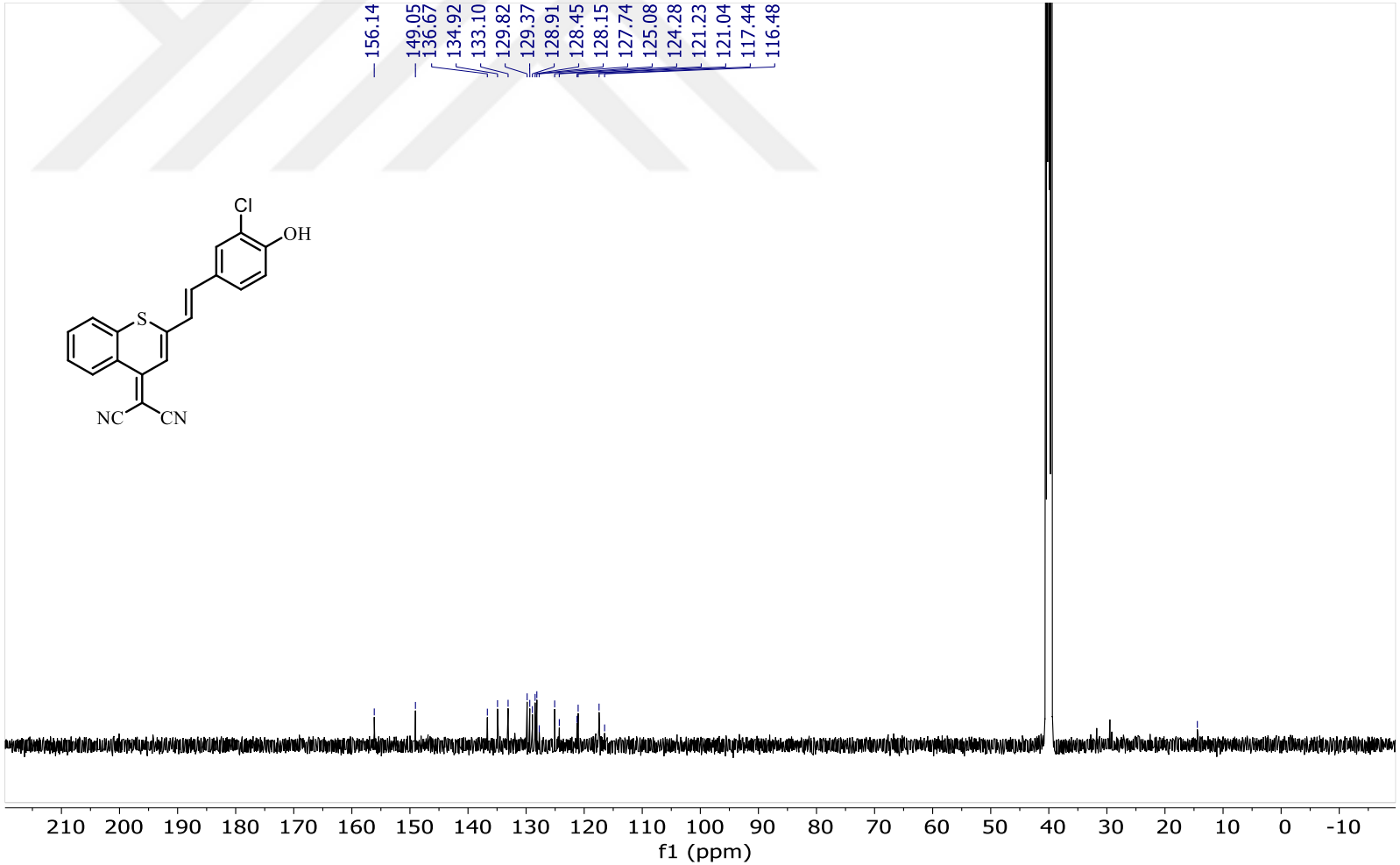

^{13}C NMR of **DCMs-Cl** in d_6-DMSO

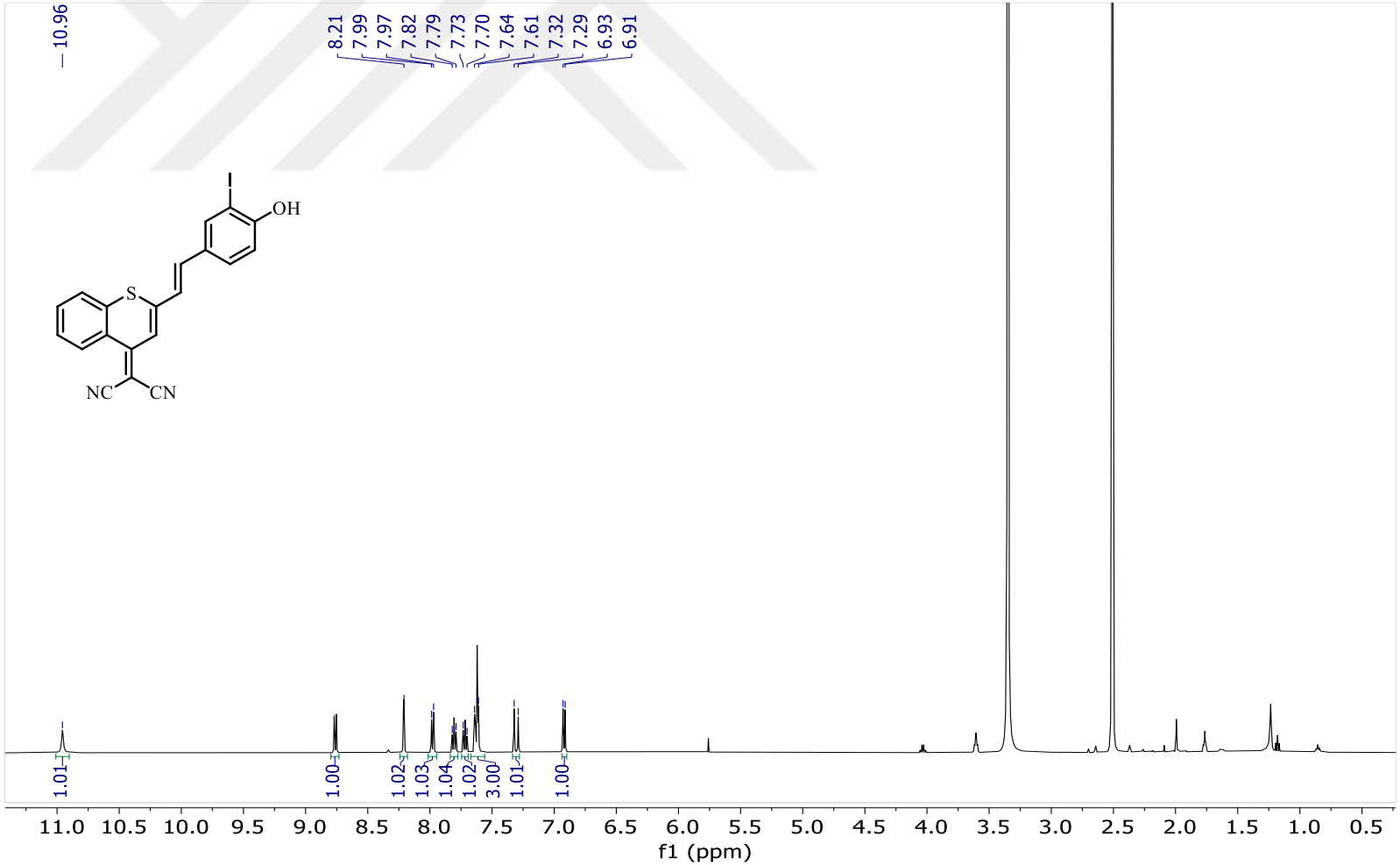

^{1}H NMR of **DCM$_{S}$-I** in d_6-DMSO

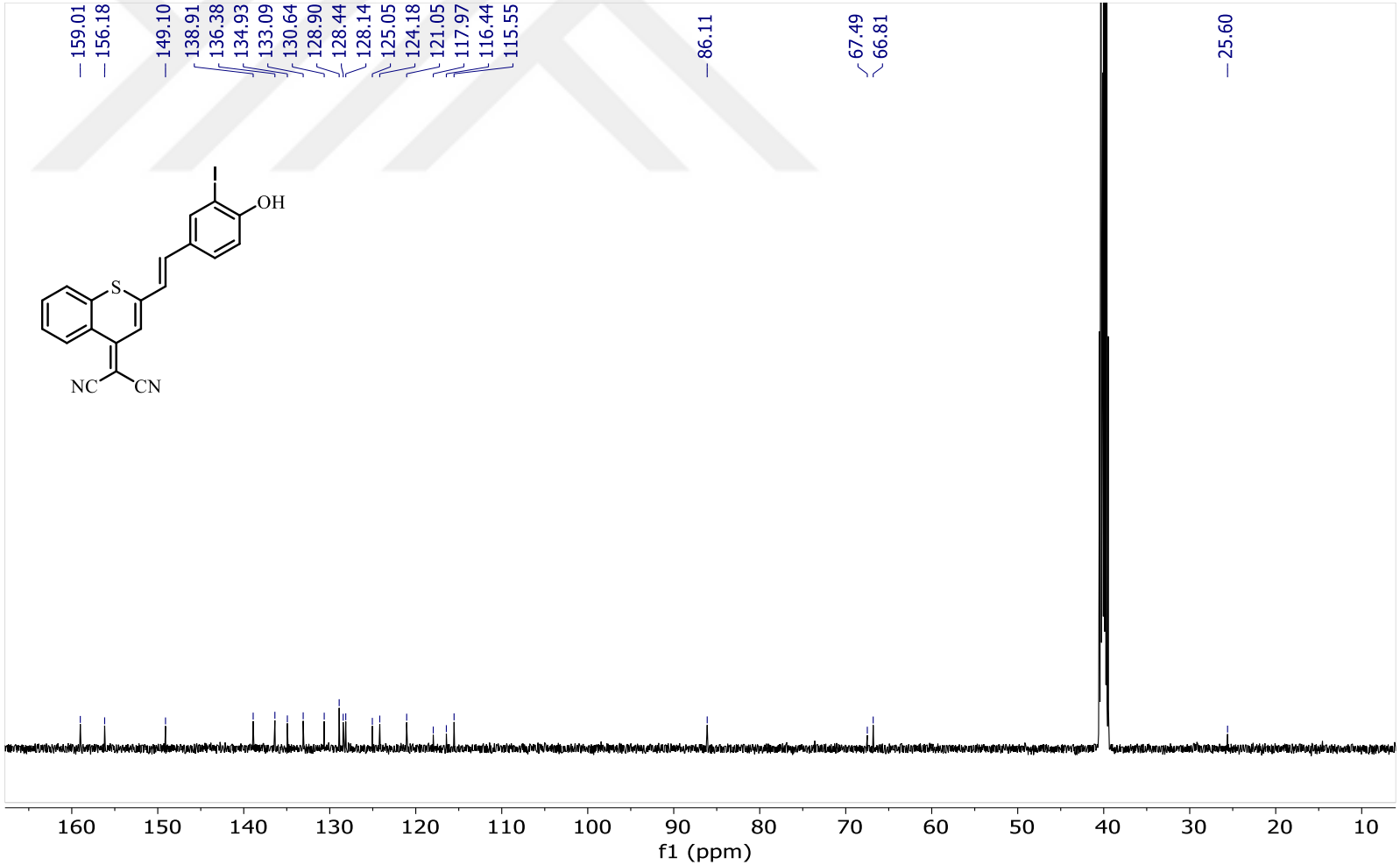

^{13}C NMR of **DCM$_S$-I** in d_6-DMSO

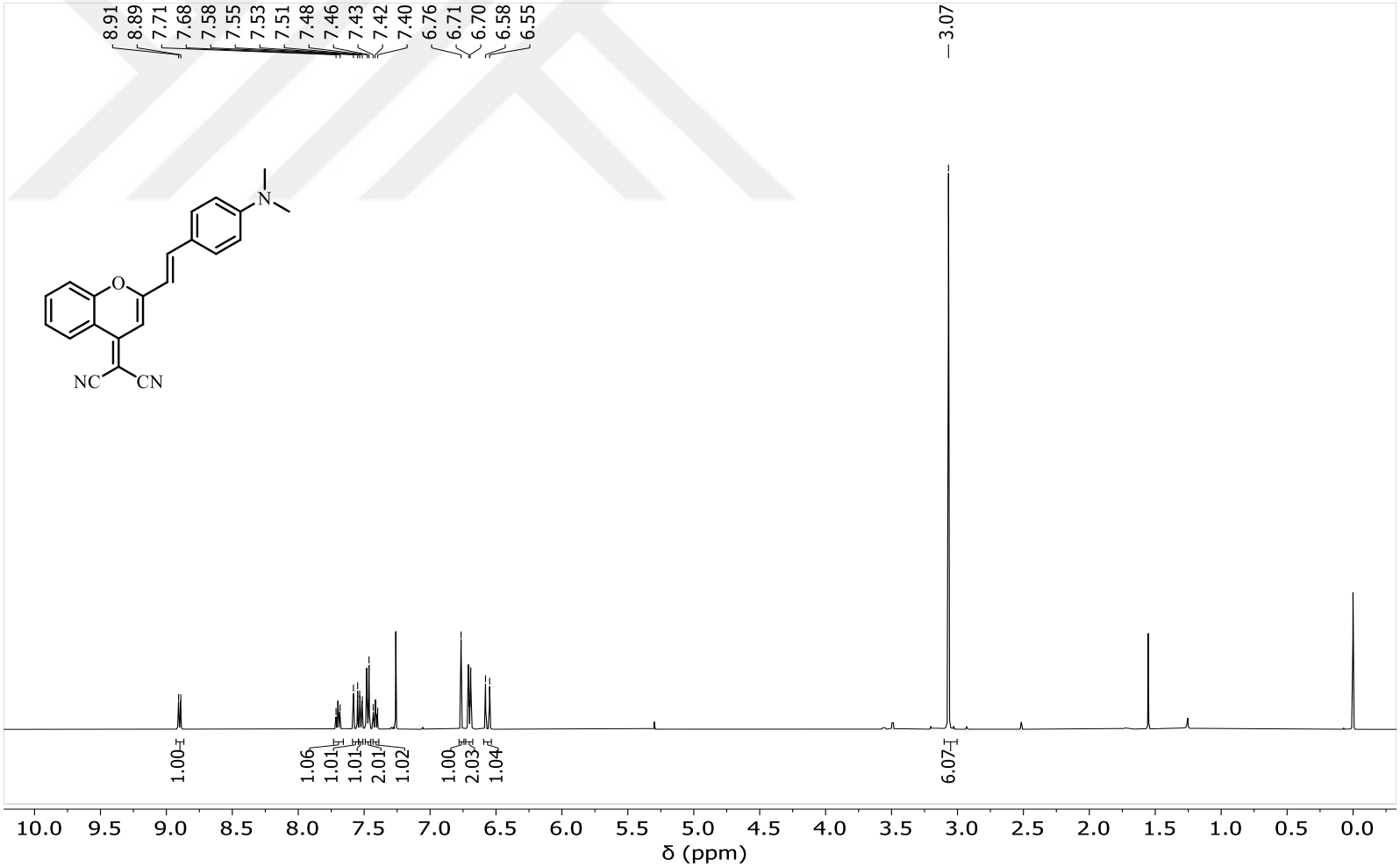

^{1}H NMR of **Compound 12** in $CDCl_3$

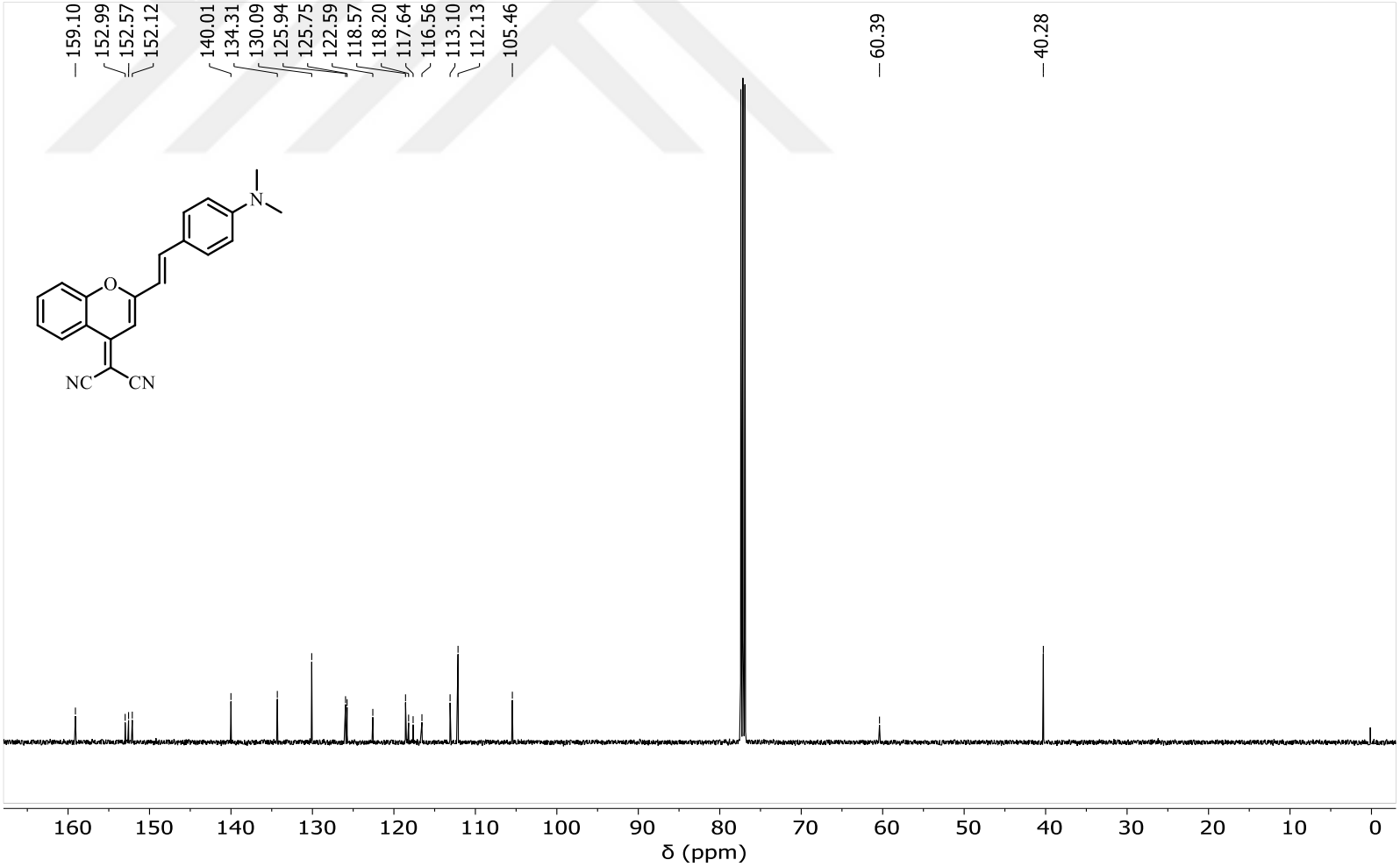

^{13}C NMR of **Compound 12** in $CDCl_3$

Appendix B: Mass Spectra

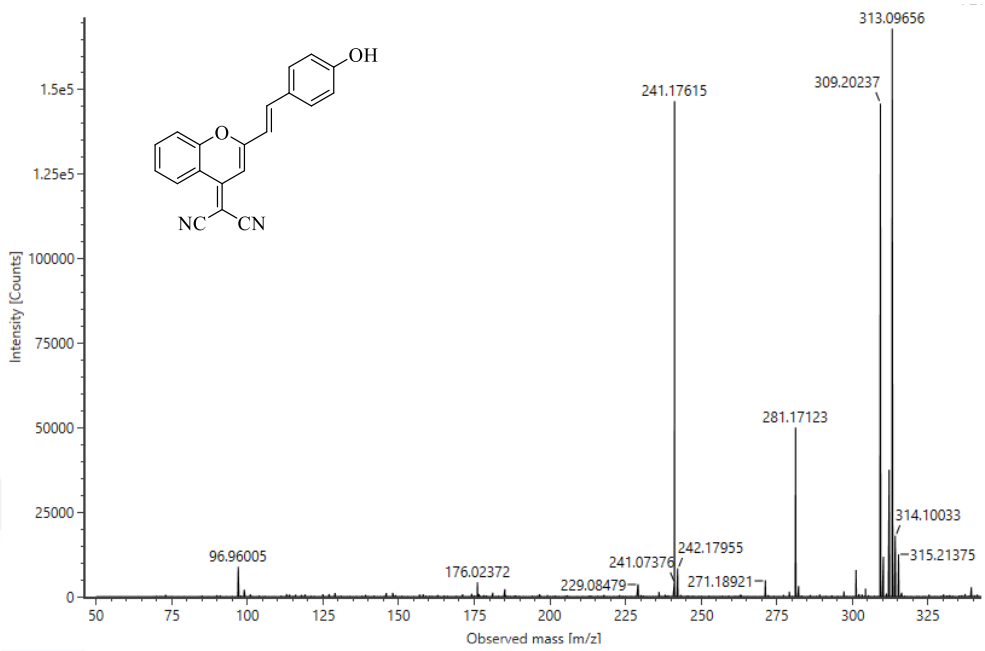

HRMS spectra of **DCMo**

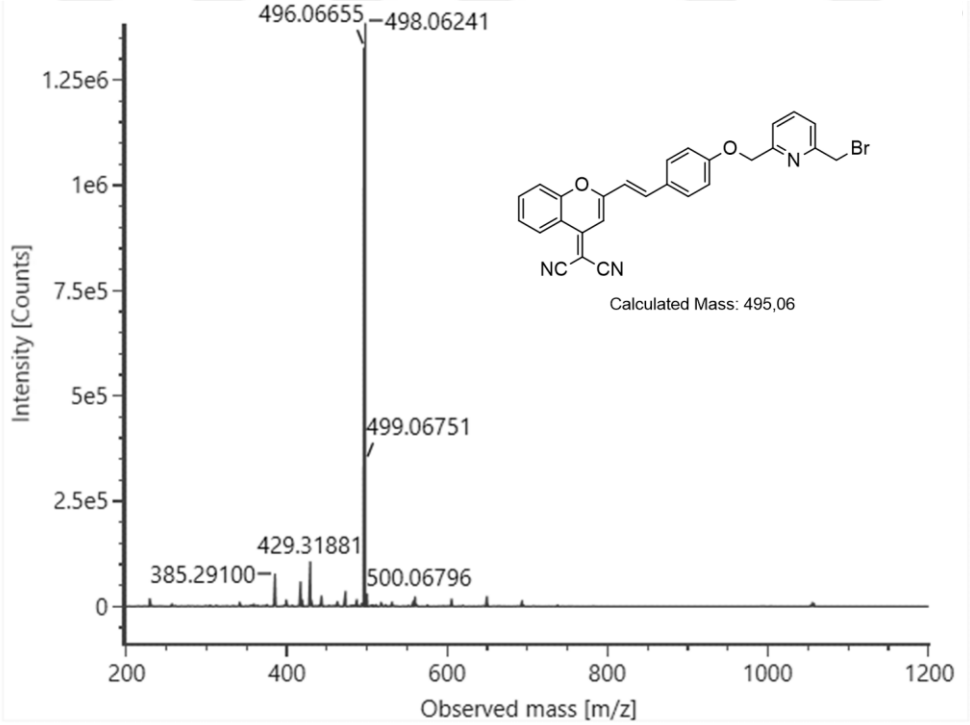

HRMS spectra of **Compound 4**

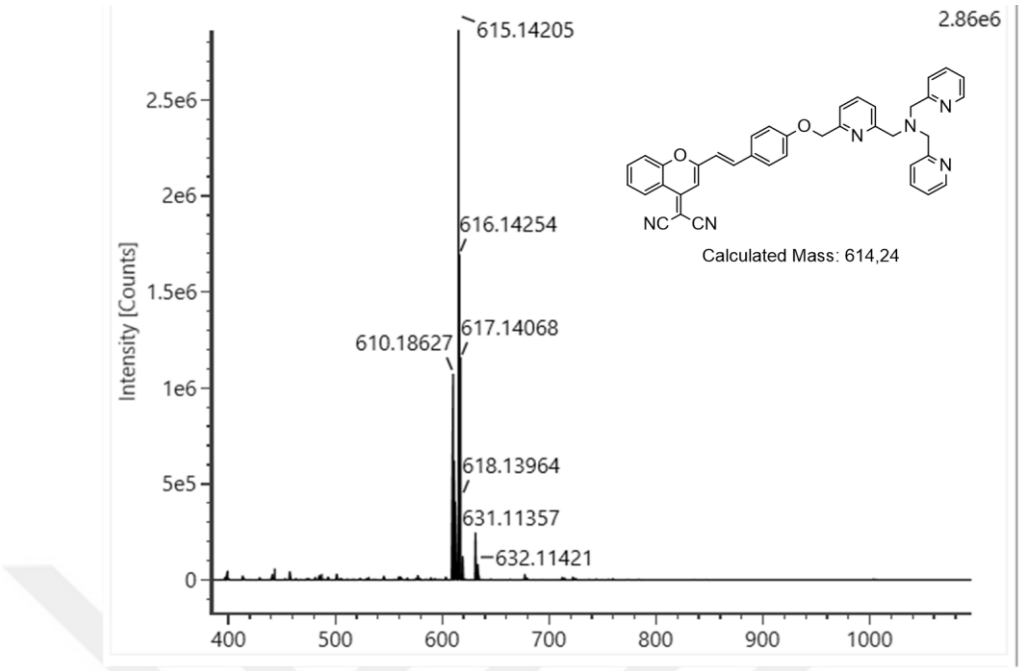

HRMS spectra of **DCM-Cu**

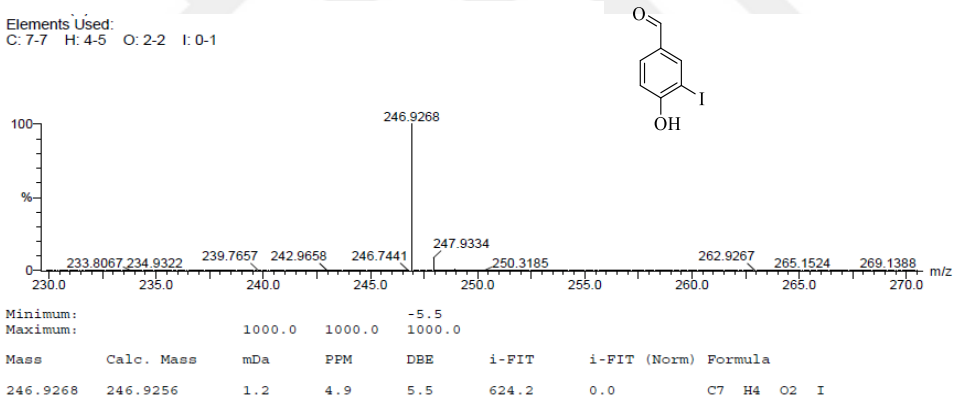

Minimum: -5.5
Maximum: 1000.0 1000.0 1000.0

Mass	Calc. Mass	mDa	PPM	DBE	i-FIT	i-FIT (Norm)	Formula
246.9268	246.9256	1.2	4.9	5.5	624.2	0.0	C7 H4 O2 I

HRMS spectra of **Compound 5**

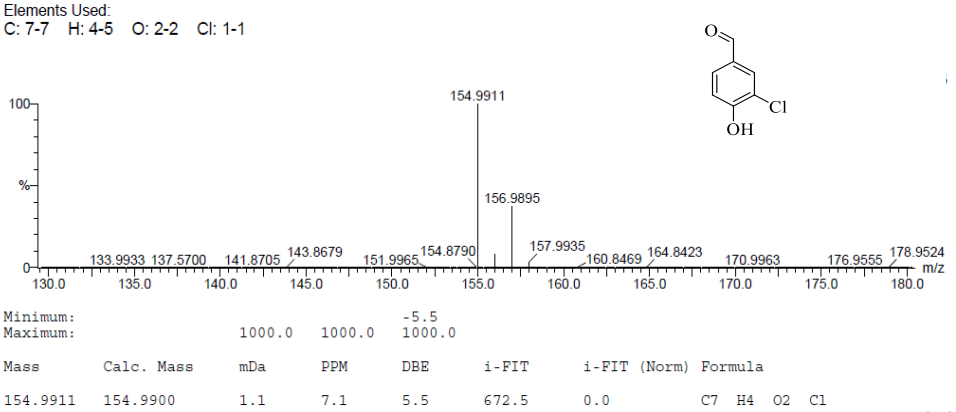

Minimum: -5.5
Maximum: 1000.0 1000.0 1000.0

Mass	Calc. Mass	mDa	PPM	DBE	i-FIT	i-FIT (Norm)	Formula
154.9911	154.9900	1.1	7.1	5.5	672.5	0.0	C7 H4 O2 Cl

HRMS spectra of **Compound 6**

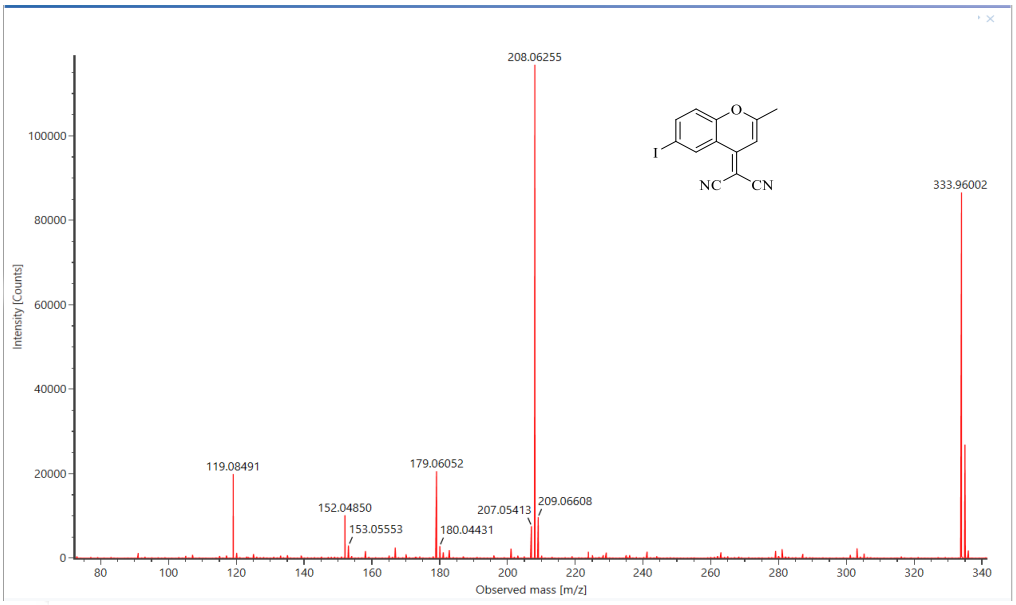

HRMS spectra of **Compound 9**

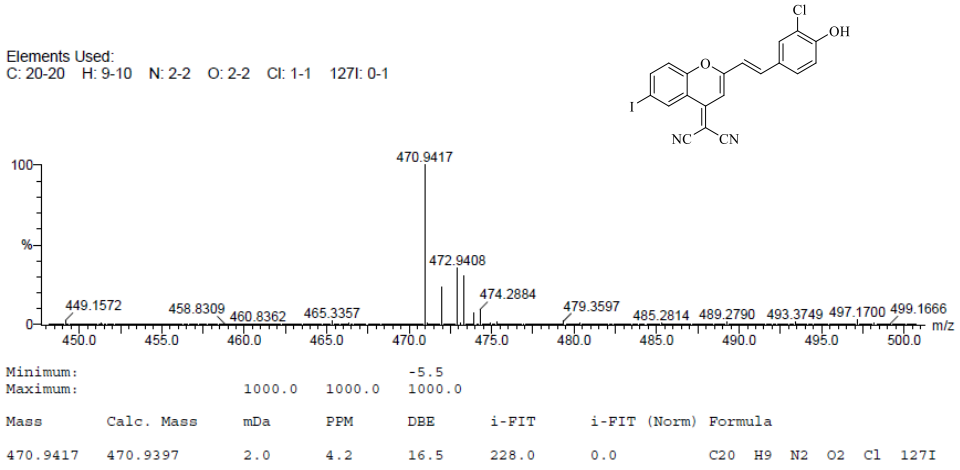

Minimum: -5.5
Maximum: 1000.0 1000.0 1000.0

Mass	Calc. Mass	mDa	PPM	DBE	i-FIT	i-FIT (Norm)	Formula
470.9417	470.9397	2.0	4.2	16.5	228.0	0.0	C20 H9 N2 O2 Cl 127I

HRMS spectra of **I-DCM$_O$-Cl**

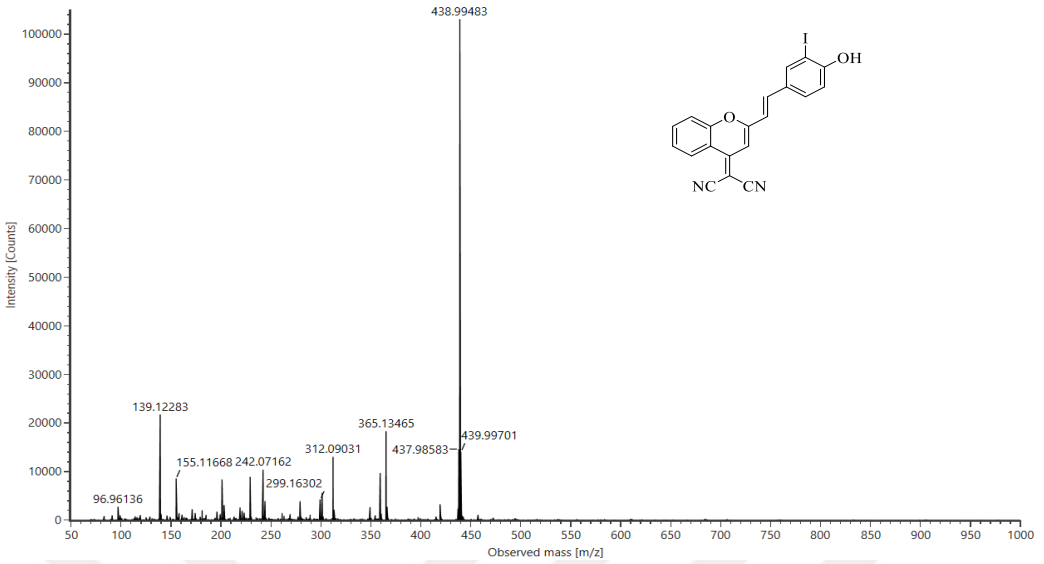

HRMS spectra of **DCM_O-I**

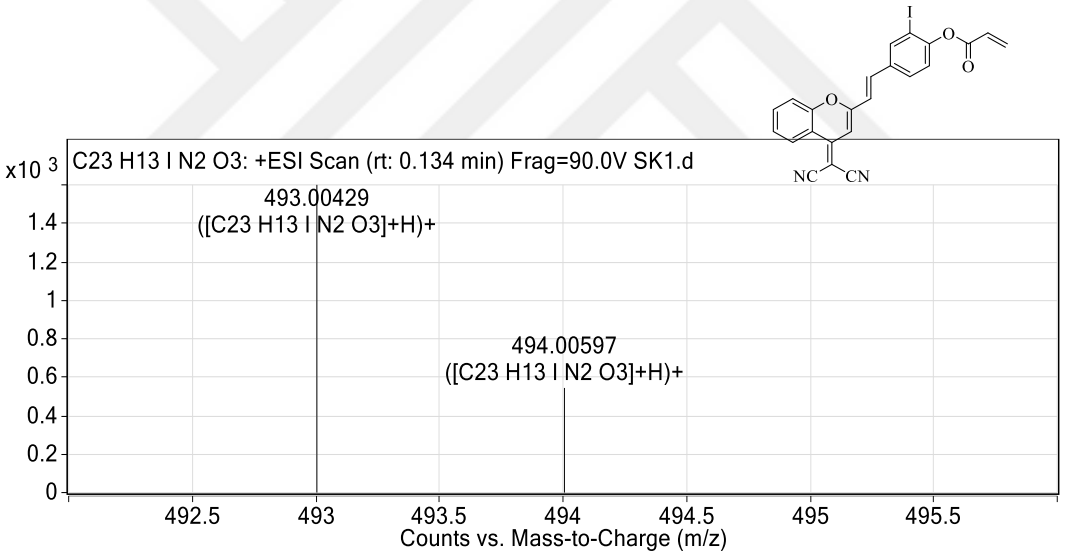

HRMS spectra of **DCM_O-I-Cys**

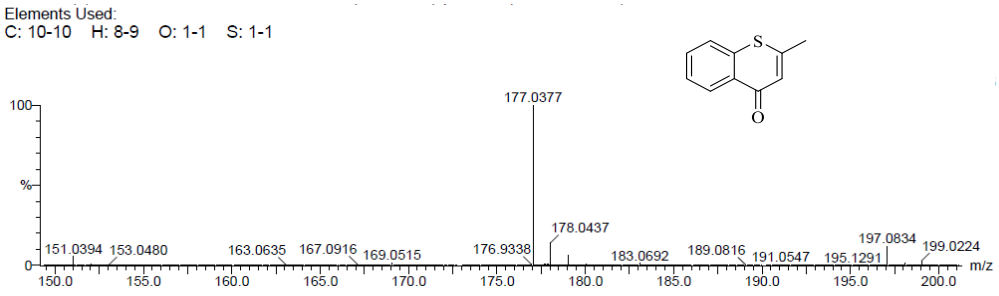

Minimum:				-5.5			
Maximum:		1000.0	1000.0	1000.0			
Mass	Calc. Mass	mDa	PPM	DBE	i-FIT	i-FIT (Norm)	Formula
177.0377	177.0374	0.3	1.7	6.5	933.2	0.0	C10 H9 O S

HRMS spectra of **Compound 10**

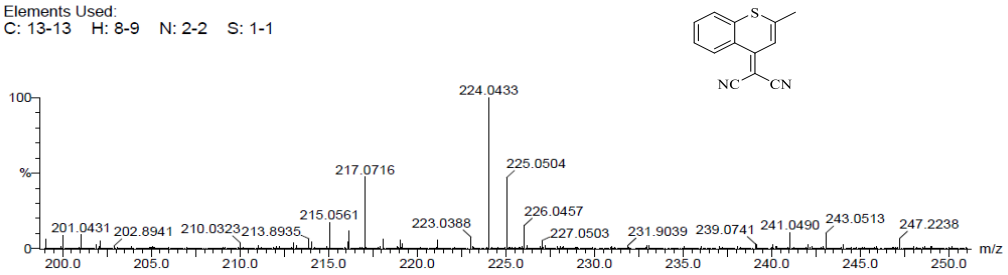

Minimum:				-5.5			
Maximum:		1000.0	1000.0	1000.0			
Mass	Calc. Mass	mDa	PPM	DBE	i-FIT	i-FIT (Norm)	Formula
224.0433	224.0408	2.5	11.2	11.0	410.4	0.0	C13 H8 N2 S

HRMS spectra of **Compound 11**

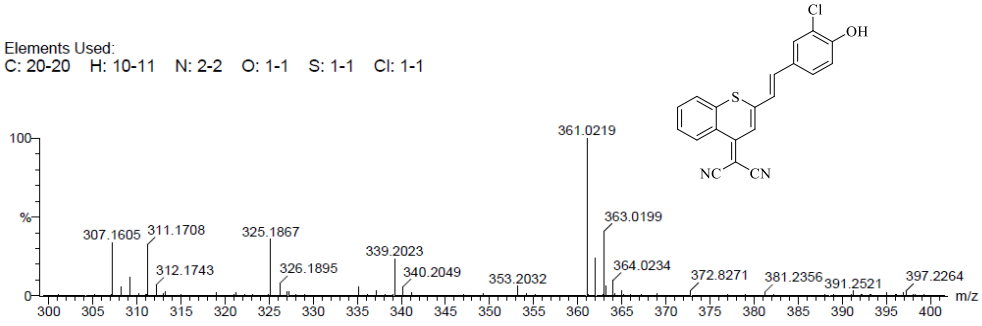

Minimum:				-5.5			
Maximum:		1000.0	1000.0	1000.0			
Mass	Calc. Mass	mDa	PPM	DBE	i-FIT	i-FIT (Norm)	Formula
361.0219	361.0202	1.7	4.7	16.5	244.7	0.0	C20 H10 N2 O S Cl

HRMS spectra of **DCMs-Cl**